Astrophysical simulations of Self-interacting Dark matter

Dissertation

zur Erlangung des Doktorgrades
an der Fakultät für Mathematik, Informatik und Naturwissenschaften
Fachereich Physik
der Universität Hamburg

vorgelegt von

Sabarish Venkataramani Malathi

Hamburg
2026

Gutachter der Dissertation:	Prof. Dr. Marcus Brüggen Dr. Kai Schmidt-Hoberg
Zusammensetzung der Prüfungskommission:	Prof. Dr. Marcus Brüggen Dr. Kai Schmidt-Hoberg Prof. Dr. Jochen Liske Prof. Dr. Stephan Rosswog Prof. Dr. Luisa Lucie-Smith
Vorsitzender der Prüfungskommission:	Prof. Dr. Jochen Liske
Datum der Disputation:	26.03.2026
Vorsitzender des Fach-Promotionsausschusses PHYSIK:	Prof. Dr. Johannes Haller
Leiter des Fachbereichs PHYSIK:	Prof. Dr. Markus Drescher
Dekan der Fakultät MIN:	Prof. Dr.-Ing. Norbert Ritter

Zusammenfassung

Das Standardmodell der Kosmologie und Teilchenphysik erzielte im vergangenen Jahrhundert große Erfolge, trotz fehlendem Verständnis der Natur der Dunklen Materie (DM). Die astrophysikalische Phänomenologie verschiedener DM-Modelle eignet sich besonders gut zur Ableitung von Einschränkungen ebendieser. In dieser Arbeit untersuchen wir selbstwechselwirkende Dunkle Materie (SIDM), welche als Kandidat zur Lösung vieler Herausforderungen der ΛCDM-Kosmologie gesehen wird. Selbstwechselwirkung Dunkler Materie tritt in vielen Modellen natürlicherweise auf. Hierzu führen wir N-Körper- und Fluidsimulationen von SIDM durch, um ihre Phänomenologie zu verstehen und Literaturlücken zu schließen.

Daher analysieren wir SIDM-Effekte auf Skalen von Galaxienhaufen. Die bisherigen Einschränkungen beruhen auf der Annahme eines geschwindigkeitsunabhängigen Wirkungsquerschnitts. Viele SIDM Theorien beinhalten jedoch geschwindigkeitsabhängige Wirkungsquerschnitte. Wir erweitern diese Beschränkungen auf geschwindigkeitsabhängige Selbstwechelwirkungen mit stark anisotropen oder isotropen Winkelabhängigkeiten. Mithilfe von Simulationen zeigen wir, dass Degenerationen zwischen den Wirkungsquerschnitt-Parametern unterschiedlicher SIDM-Modellen, die in isolierten Halos bestehen, bei Verschmelzungen von Galaxienhaufen aufgehoben sind. Außerdem zeigen wir, dass Effekte der Selbstwechelswirkung sich in späteren Verschmelzungsphasen verstärken. Wir vermuten, dass in Zukunft durch hydrodynamische, kosmologische SIDM Simulationen und deren Vergleich mit der großen Menge beobachtender Daten, Modelle präziser eingegrenzt werden können.

Wir verschieben unseren Fokus auf kleinere Skalen und analysieren die Effekte von SIDM um Schwarze Löcher (BH) durch die Simulation von DM-Spikes. Dies ist von besonderem Interesse, da SIDM das ffinal parsec problem”der Verschmelzung supermassereicher Schwarzer Löcher (SMBH) lösen könnte. Wir bestätigen daher erstmals die Existenz von SIDM-Lösungen im Gleichgewicht um Schwarze Löcher mithilfe von N-Körper-Simulationen. Wir simulieren SIDM in einem Regime, in dem die Relaxationszeitskala größer oder gleich der Umlaufzeitskala ist. Zusätzlich können wir einen Ausdruck für die Akkretionsrate der SIDM ableiten. Desweiteren simulieren wir SIDM-Spikes im SMFP-Regime, einem Regime in dem die Relaxtionszeit viel kleiner ist als die Umlaufzeit, mit hydrodynamischen Simulationen. Wir finden heraus, dass in diesem Regime die Gleichgewichtsprofile der SIDM-Spikes nahe an den Bondi-Lösungen sind. Schließlich skizzieren wir die SIDM-Akkretionsrate gegen eine variierende Kollisionsrate vom kollisionslosen zum hydrodynamischen Limit. Ein Verständnis der Variation der Akkretionsrate kann uns potentiell helfen, hochrotverschobene SMBH-Beobachtungen zu interpretieren.

Abstract

The standard model of cosmology and particle physics has seen enormous success over the last century despite the fact that there is a lack of understanding of what dark matter (DM) is. The astrophysical phenomenology of various dark matter models have proven to be particularly useful in constraining them. In this thesis, we study self-interacting dark matter (SIDM). SIDM is considered a candidate for many challenges that ΛCDM cosmology faces. DM self-interactions naturally arise in a variety of DM models. To this end we perform N-body and fluid simulations of SIDM to understand their phenomenology and fill missing gaps in the literature.

Galaxy clusters have proven to be the best testbeds for SIDM, we study the effects of SIDM at these scales. In literature, constraints on the cross-section have been derived assuming velocity independent cross-section with the help galaxy cluster observations. However, velocity dependent cross-sections are present in most theories of SIDM. We extend these constraints to velocity dependent self-interactions that also feature either strongly anisotropic or isotropic angular dependencies. Using simulations, we show that the degeneracy between the cross-section parameters of different SIDM models that exist in the evolution of isolated haloes is broken in galaxy cluster mergers and that the effects of self-interactions are found to be more prominent during later stages of merger even with the inclusion of velocity dependence. We speculate that by performing hydrodynamical simulations with SIDM on cosmological scales, and comparing them with the wealth of data that we will have in the near future these models can be constrained better.

We then shift focus to smaller scales where we study the effects of SIDM around black holes (BH) by simulating DM spikes. This is of great interest since, SIDM has been considered to be capable of solving the ”final parsec problem” of SMBH mergers. Therefore, we verify for the first time that steady-state solutions for SIDM can exist around BHs using N-body simulations in the regimes where SIDM relaxation timescale is larger than or equal to the orbital timescale and derive an expression for the accretion rate of SIDM in these regimes. Then, we simulate SIDM spikes in the SMFP regime, i.e. a regime where SIDM relaxation timescale is much shorter than the orbital timescale, using hydrodynamical simulations. We find that in this regime, the profiles of SIDM spikes are close to the Bondi solutions with mildly suppressed accretion rates. Finally, we sketch the accretion rate of SIDM against varying collisionality all the way from collisionless limit to the hydrodynamical limit. Understanding the variation in accretion rate across collisionality can potentially aid us in making sense of the observations of SMBHs at high redshifts.

List of publications

This thesis is based on the following publications:

First author publications:

- **Sabarish, V. M.**, Brüggen, M., Schmidt-Hoberg, K., Fischer, M. S. & Kahlhoefer, F. Simulations of galaxy cluster mergers with velocity-dependent, rare, and frequent self-interactions. MNRAS 529, 2032–2046 (2024).
- **Sabarish, V. M.**, Brüggen, M., Hoberg, K.-S. & Fischer, M. S. Accretion of self-interacting dark matter onto supermassive black holes. Astronomy and Astrophysics 703, A142 (2025).

Contents

List of Abbreviations

AGN	Active Galactic Nuclei
BAO	Baryon Acoustic Oscillations
BBN	Big Bang Nucleosynthesis
BC	Boundary Conditions
BCG	Brightest Cluster Galaxy
BH	Black Hole
BSM	Beyond Standard Model
CL	Confidence Level
CMB	Cosmic Microwave Background
DM	Dark Matter
DR	Dark Radiation
DSMC	Direct Simulation Monte Carlo
FPP	First pericentre passage
fSIDM	Frequently Self-Interacting Dark Matter
GRMHD	General Relativistic Magnetohydrodynamics
GW	Gravitational Waves
IC	Initial Conditions
ISM	Interstellar Medium
ICM	Intracluster Medium
LMFP	Large Mean Free Path
MFP	Mean Free Path
MLR	Mass–Light Ratio
MMR	Merger mass ratio
MOND	Modified Newtonian Dynamics
rSIDM	Rarely Self-Interacting Dark Matter
RS	Relativistic Species
SIDM	Self-Interacting Dark Matter
SIWDM	Self-Interacting Warm Dark Matter
SIMP	Strongly Interacting Massive Particle
SM	Standard Model
SMBH	Supermassive Black Hole
SMFP	Small Mean Free Path
SPH	Smoothed Particle Hydrodynamics
WIMP	Weakly Interacting Massive Particle
WPDM	Warm Particle Dark Matter

1 Introduction

In the beginning of the last century, we slowly started collecting evidence for missing mass in astrophysical systems dubbed *dark matter*. This idea did not immediately gain attention, and many astronomers and astrophysicists considered dark matter to be *baryonic matter* that is dark. Dark matter, as non-baryonic matter, eventually found its place through the observations of galaxy rotation curves, Big Bang Nucleosynthesis (BBN) constraints on the baryonic density parameter, and COBE measurements of the Cosmic Microwave Background (CMB). The observation of the Bullet cluster was the final nail in the coffin. To date, it remains the most difficult observation to explain for a majority of modified theories of gravity that challenge the existence of dark matter. Thus, by the turn of the century ΛCDM cosmology was accepted as the concordance model despite the lack of understanding what dark matter is, and it still remains to be an important and fundamental challenge in modern physics and cosmology. The entirety of this thesis will be under the premise of dark matter being a non-baryonic particle. In particular, collisionless dark matter along with self-interacting dark matter will be the main focus of this thesis.

1.1 Evidence and challenges of ΛCDM Cosmology

Astrophysical observations in the linear scales, i.e. from the scale of the horizon ($\sim$ 10 Gpc) all the way down to a scale of $\sim$ 1 Mpc are consistent with the predictions of ΛCDM cosmology. In this section we will first highlight why certain observations are considered to be evidences for the concordance model before discussing the challenges it faces. Early evidence for dark energy were primarily the increasing recession velocities of galaxies with distance due to Hubble (1929). Early evidence for dark matter are primarily of two nature : (i) the need for a non-zero local dark matter density to explain the motion of stars in the local solar neighbourhood (Jeans 1922, Kapteyn 1922, Oort 1932) (ii) the need for more mass to explain the velocity dispersion of galaxies in galaxy clusters (Zwicky 1933, Zwicky 1937). The authors of these papers referred to baryonic matter that was *dark* as dark matter. Around this time, on the theoretical front, there was the emergence of FLRW cosmology describing a homogenous and isotropic universe (Friedmann 1922, Lemaître 1931, H. P. Robertson 1935, Walker 1935).

The first direct evidence for the existence of non-baryonic matter partly comes from the predictions of elemental abundances due to primordial nucleosynthesis. BBN calculations allow us to estimate the abundances of light elements by solving a network of differential equations. BBN calculations are done in a background FLRW metric, and the main free parameters to solve this network of equations is baryon-to-photon number density ratio $\eta = n_b/n_\gamma$ and the effective number of neutrino species $N_{\rm eff}$. Although BBN was proposed much earlier (Gamow 1946, Alpher et al. 1948), making predictions on elemental abundances still remained impossible due to the lack of observational knowledge on the parameters $\eta, N_{\rm eff}$. This changed with the following developments in both theory and observations : (i) observation of the temperature of the CMB by Penzias et al. (1965) provided a handle on n_γ (ii) observation of deuterium in the interstellar medium provided a handle on the elemental abundance of deuterium due to BBN, as stellar nucleosynthesis cannot produce them (iii) emergence of the standard model of particle physics and that $N_{\rm eff} \approx 3$ owing to the 3 neutrino flavours. Given these three pieces of information, Reeves et al. (1973) estimated that $\Omega_{b,0} \lesssim 0.1\ \Omega_{\rm crit,0}$. Here, $\Omega_{b,0},\ \Omega_{\rm crit,0}$ are the baryon density parameter, and the critical density parameter at redshift 0. Observations of elemental abundances have become more precise over the years. In recent years, thanks to high resolution spectroscopy, deuterium abundance has been estimated by looking at low-metallicity quasar absorption features to a high precision. This in turn has led to the estimation $\Omega_{b,0} \approx 0.048$ (Cooke et al. 2018, assuming $h = 0.67$). Now, the complementary observation that will serve as a direct evidence for non-baryonic matter is the estimation of $\Omega_{m,0}$ from galaxy clusters. It was shown by N. A. Bahcall et al. (1995), Carlberg et al. (1996) that using observed luminosity of cluster galaxies, and the field luminosity density, one can estimate the total matter density parameter to be $\Omega_{m,0} \sim (0.2-0.3)\ \Omega_{\rm crit,0}$. Clearly, BBN constraints and cluster estimates on the matter content of the universe show that more than 80% of matter is non-baryonic in nature.

The most popular evidence that is usually quoted in media is due to Rubin et al. (1970), Rubin et al. (1980). They show that the observed rotation curves $V_c(r)$ of galaxies cannot be explained only with observed luminous matter. To further the evidence for missing mass, Roberts et al. (1975) measured the rotation curve far outside the optical disk only to find that it is approximately constant at such distances. An alternative hypothesis, Modified Newtonian Dynamics (MOND), was proposed to explain the missing mass seen in the rotation curves of galaxies by Milgrom (1983). Although MOND was initially successful in explaining the flattening of rotation curves (Lelli et al. 2017), it proves inadequate in explaining the most robust evidence for CDM, which are discussed below.

Another independent cosmological probe that provided evidence for ΛCDM is the temperature auto-correlation power spectrum of the CMB first observed by COBE (Smoot et al. 1992) at larger angular scales. The success of COBE led to follow-up missions such as WMAP, Planck, ACT, SPT, and the upcoming LiteBIRD satellite experiment, among others. The effect of CDM can be seen in baryon acoustic oscillations (BAO). Before recombination during matter domination, baryons are tightly coupled to photons due to frequent Compton scattering. Further, the baryon-photon plasma flowed towards regions of lower gravitational potential, that is where the matter over density parameter δ_m was large. As the plasma density increased in these potential

Figure 1.1: Composite image of the Bullet cluster combining JWST's NIRCam, and X-rays from Chandra X-Ray observatory. The hot gas observed in X-rays is shown in pink. The mass distribution of the collisionless component (galaxies, DM, intra-cluster stars) is shown in blue. The two circles mark the galaxy clusters. A detailed discussion of what JWST adds to our knowledge of the Bullet cluster can be found in Cha et al. (2025). Image: NASA, ESA, CSA, STScI, CXC; Science: James Jee (Yonsei University, UC Davis), Sangjun Cha (Yonsei University), Kyle Finner (Caltech/IPAC)

wells, the photon pressure gradually increased until the pressure pushes the plasma outwards setting up a radially oscillating system. The odd peaks in the CMB spectrum correspond to the state when the baryon-photon plasma is maximally compressed, while the even peaks correspond to the maximally rarefied state. Even in the absence of CDM, the baryon-photon plasma can oscillate; however, the successive peaks are suppressed due to the increased inertia of the fluid from a higher baryon density. In the presence of non-baryonic matter, n-th odd peak is more pronounced than the even $(n-1)$-th peak. Therefore, this is clear signal of non-baryonic matter.

Relativistic extensions of MOND were introduced to study cosmology. Most of the relativistic extensions of MOND that dismiss dark matter, struggle to explain the observed asymmetry in the second and third peak of the CMB (e.g. see Figure 3 in Skordis 2009). In this regard, the only known successful relativistic extension of MOND that is compatible with this feature in the CMB is a particular model belonging to the class of TeVeS (Tensor-Vector-Scalar) theories proposed in Skordis et al. (2021). However, it is worth noting that the apparent compatibility with the CMB of these models only comes at the cost of introducing additional scalar and vector fields. Therefore, it is evident that within the Einsteinian theory of gravity, a baryon-only universe is incompatible with the CMB.

By the beginning of the 21st century, it was possible to measure masses of galaxy clusters using lensing with good precision. One of the strongest arguments for dark matter, is due to this advancement. Douglas Clowe, et al. published a paper where part of its title read *Direct Evidence for the Existence of Dark Matter* (Clowe et al. 2004). The Bullet cluster as shown in **Fig. 1.1** is a system of merging galaxy clusters, where the clusters have just passed their first crossing. In their paper they show that, the mass peak identified due to lensing is significantly displaced from the gas peaks identified for the intra-cluster medium (ICM) using X-ray imaging. Most of the modified theories of gravity that challenge the dark matter paradigm suffer from not being able to explain this observation without invoking non-baryonic components. In particular as argued in Angus et al. (2007), the missing mass is compatible with MOND only if the three species of neutrinos have masses $m_\nu \approx 1$ to $2\,\mathrm{eV}$. Such a neutrino mass is already at the limits of allowed neutrino mass constraints due to cosmological probes (Planck Collaboration et al. 2020a) and KATRIN experiment (Katrin Collaboration et al. 2025). Angus et al. (2010) accounts for this fact and proposes that massive sterile neutrinos with mass $m_\nu \sim 11\,\mathrm{eV}$ can explain bullet cluster. However, such a mass is clearly excluded due to cosmological constraints (Hamann et al. 2010). In any case what is clear is that the observations of the Bullet cluster cannot be explained with baryons alone.

1.1.1 Challenges of ΛCDM Cosmology

Foundational challenges

ΛCDM cosmology despite all of its success faces some challenges. The most famous of these tensions is the Hubble tension, wherein the measured value of the Hubble constant from the CMB is at $\sim 5\sigma$ tension with the locally measured values. A plethora of models have been proposed to fix this, see Schöneberg et al. (2022) for a ranking of these models and how they compete with each other given all the available datasets. Very recently, Freedman et al. (2025) have shown with JWST observations that the tension is reduced and is compatible with CMB measurements (Planck Collaboration et al. 2020b), but the SH0ES team report that tension stays using JWST data (Riess et al. 2024). Another tension is the so-called S8 tension, where the inferred values of $S8 = \sigma_8\sqrt{\Omega_{m,0}/0.3}$ from CMB is at tension with the ones inferred from weak-lensing and galaxy clustering (see Abdalla et al. (2022) for a review). Very recently, Wright et al. (2025) find that the inferred S8 is consistent with Planck results. Therefore, as of today, it is not entirely clear if these tensions will disappear or not with more data and observations.

Small-scale challenges

Given the successes of ΛCDM on the linear scales. Let us turn our attention to the non-linear scales. An order of magnitude estimate for the wave number (k_{NL}) where non-linear effects start contributing follows from demanding $\Delta_L^2(k) \sim 1$, here $\Delta_L^2(k)$ is the variance of the linear density perturbations of the matter field. At $z = 0$, this results in $k_{\mathrm{NL}} \approx 0.25h\mathrm{Mpc}^{-1}$, this approximately gives a length scale of $r \sim 10\,\mathrm{Mpc}$. To understand the properties of the structures, below this scale one needs N-body simulations. The methodology of these simulations will be briefly described in **section 1.4.1**. Navarro et al. (1996) ran one of these simulations in a cosmological setting, and they found a universal profile that approximately fits the measured density profiles of dark matter halos in the simulations.

$$\rho(r) = \frac{\delta_c \rho_{\mathrm{crit}}}{r/r_s(1 + r/r_s)^2} = \frac{4\rho_{-2}}{(r/r_{-2})(1 + r/r_{-2})^2} = \frac{\rho_0}{r/r_s(1 + r/r_s)^2}. \tag{1.1}$$

Here, r_s and r_{-2} are the characteristic radii called the scale radius. In literature, ρ_0 is often written as ρ_s, and in some other papers ρ_{-2} is often written as ρ_s. To avoid ambiguity ρ_0 and $\rho_{-2} := \rho(r_{-2})$ will be referred to as density normalization and scale density respectively. The universality of these profiles have been demonstrated in various simulations even including baryonic physics. One can naturally ask if NFW like profiles be derived from first principles. Given that on these scales perturbations evolve non-linearly and that halos can merge and accrete make this a very hard problem. Lu et al. (2006) is the one of the few papers that provides arguments for what the density profile must look like in the limiting cases. That is, they show that for small r, $\rho \sim r^{-1}$ and for large r, $\rho \sim r^{-3}$. Small-scale challenges are the discrepancies found between ΛCDM simulations and observations on scales $l \lesssim$ Mpc. For a thorough review of this topic see Bullock et al. (2017), Tulin et al. (2018). It is to be noted that astrophysical challenges to ΛCDM in addition to the ones discussed here that are well explained by MOND have been put forth (e.g. Kroupa et al. 2012). However, it remains that the success of ΛCDM lies in its simplicity, while still explaining observations across a wide range of length and time scales.

Diversity problem: The inner regions of the NFW profile scales like $\rho_{\mathrm{NFW}} \sim r^{-1}$, but observations find a range of values for the exponent (Flores et al. 1994, Moore 1994, de Blok 2010, Oman et al. 2015). The DM density profiles are usually inferred using the rotation curves of galaxies. The left panel of **Fig. 1.2** shows circular velocity at $r = 2\,\mathrm{kpc}$ vs. the maximum velocity in the rotation curve, $V_{\max}$. $V_{\max}$ serves as a proxy for the total virial mass of the halo. The black solid line is the prediction from CDM simulations, while the banded red line is from EAGLE hydro-simulations. The red dots correspond to observed galaxies. It is clear from the plot that the observed galaxies have a wide spread in $V_{\mathrm{circ}}(2\,\mathrm{kpc})$ for a given $V_{\max}$. One can also find another version of the same issue called "core vs cusp". In this case, core stands for an exponent that is approximately 0, and a cusp refers to an NFW like exponent of -1. Within ΛCDM, there have been attempts to explain it with baryonic feedback processes. That is, at cluster scales it is mostly due to AGN feedback while at the galactic scales it is due to star formation and supernova feedback (Di Cintio et al. 2014, Shirasaki et al. 2018). These feedback processes have enough energy to redistribute the DM mass altering the structure. However, it is unclear if baryonic processes alone can reproduce the observed diversity. In particular, recent literature like Santos-Santos et al. (2020), Jackson et al. (2025) explicitly state that the problem remains open.

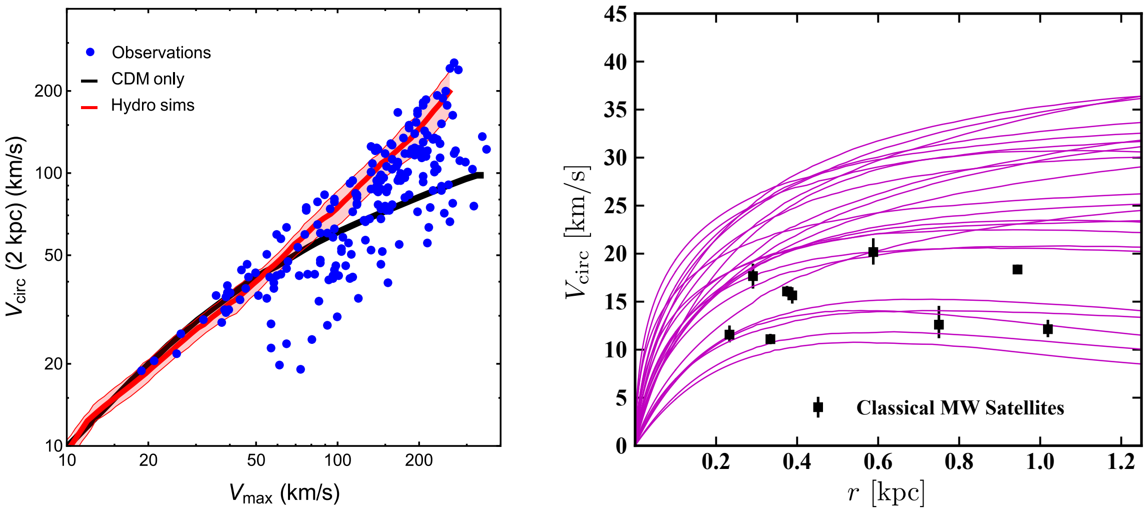

Figure 1.2: *Left :* Plot illustrating the diversity problem. *Right :* Plot illustrating the TBTF and missing-satellites problem. Plots taken from Tulin et al. (2018).

Missing satellites : In some earlier studies the predicted halo mass function at the low mass end characterizing satellite galaxies were found to be inconsistent with observations (Klypin et al. 1999, Moore et al. 1999). Until recently only $\lesssim 70$ satellite galaxies of Milky-Way were observed, but in simulations we see as high as 1000 dark subhalos for a Milky-Way like host halo. The current consensus is that the problem has largely gone away due to efforts from both observers and theorists. That is, the following hint at the problem being solved *(i)* observations of more faint dwarves due to wide field surveys (for e.g. D. Kim et al. 2015, S. Y. Kim et al. 2018, Torrealba et al. 2018) *(ii)* improved abundance matching methods to link galaxies to their host haloes (Read et al. 2019) *(iii)* zoom-in cosmological simulations with the inclusion of baryonic physics, and increased resolution resolving length scales $\lesssim 100$ pc (Roca-Fàbrega et al. 2021).

Too-big-to-fail (TBTF): TBTF problem has been reformulated in slightly different ways in the literature over the last decade. Some formulations have been argued to be resolved, while for some others it remains open. It has been argued that Milky-Way has a gap in the $V_{\rm max}$ distribution of its satellite galaxies (Boylan-Kolchin et al. 2012, Cautun et al. 2014). Specifically, there are no satellite galaxies known in the window $25\,{\rm km\,s^{-1}} < V_{\rm max} < 60\,{\rm km\,s^{-1}}$. Ostriker et al. (2019) argue that this formulation of the problem is largely resolved, as simulations like EAGLE (Schaye et al. 2015) and Illustris (Genel et al. 2014) also feature these gaps. Another formulation is that the most massive subhalos of Milky-Way like host should be very dense in the centre, yet the observed ones appear to be more cored (Boylan-Kolchin et al. 2011, Purcell et al. 2012). Therefore, this formulation is related to the diversity problem discussed above. Yet another formulation and the most commonly discussed one is that, in simulations we find a lot of very massive subhalos, $M_{\rm vir} \approx 10^{10}\,{\rm M}_\odot$ that are not found in observations (Boylan-Kolchin et al. 2011, Jiang et al. 2015). In other words, these massive halos are too big to not have accreted baryons and formed galaxies.

The right panel of **Fig. 1.2** shows the rotation curves of subhalos in cosmological simulations of a Milky-Way like host halo. The black dots are the most massive observed satellite galaxies of Milky-Way. The curves with a large $V_{\rm circ}$ are unpopulated by galaxies, highlighting that the most massive ones have failed to form galaxies. Many authors claim that upon accounting for environmental effects like tidal stripping, ram pressure evaporation these observations can become consistent with ΛCDM (e.g. Zolotov et al. 2012, Dutton et al. 2016).

Supermassive Black holes at high redshift

Numerous quasars hosting a SMBH of mass $\sim 10^9\,{\rm M}_\odot$ have been observed at redshifts $z > 6$. This has been difficult to explain with ΛCDM and our current models of SMBH seed formation channels (Inayoshi et al. 2020, Fan et al. 2023). Some popular models include formation of seeds $M_{\rm seed} \sim 10^3 - 10^4{\rm M}_\odot$ from the collapse of Population-III stars at high redshifts, $z \lesssim 30$, or the direct collapse of baryonic gas. In both these models a near Eddington accretion rate across several orders of magnitude of growth in mass is required to be able to explain the observations. Such sustained near Eddington accretion rate is very difficult. Therefore, the consensus is that we need mechanisms that can lead to super-Eddington accretion rates and/or formation scenarios where very massive seeds form. In addition to these, a large collection faint AGNs dubbed Little Red Dots (LRDs) have been detected by JWST (Kocevski et al. 2023, Matthee et al. 2024). For a discussion on the physical nature of these objects see Inayoshi et al. (2025). The observed number density of these objects pose a challenge to ΛCDM cosmology.

1.1.2 Alternate models of Dark matter as solutions

The dark model discussed so far is the classic Weakly Interacting Massive Particle (WIMP) like DM. In this section alternate models of DM and how they stand against the crisis in ΛCDM will be discussed. As far as astrophysical phenomenological studies are considered, DM can be broadly classified into particle DM and wave DM. WIMP like DM is a particle DM candidate typically in the mass range 1 GeV to 100 TeV.

Warm particle dark matter (WPDM)

Warm particle dark matter is a subclass of particle DM models where the particles have a non-negligible free streaming length. Mainstream WDM has a mass $\sim$ keV. For the rest of the discussion on WDM, the focus will be placed on thermal WDM. The main characteristic of WDM is that depending on the mass and the temperature at which it decouples from standard-model particles, one can define a free streaming wave number $k_{\rm FS}$ below which the linear matter power spectrum is suppressed. This suppression of power spectrum at small scales has been attributed to solve the small-scale crisis. Assuming all of dark matter is warm, the physical smoothing scale can be written as (Bode et al. 2001, Schneider et al. 2013),

$$R_{\rm FS} \approx 0.2(\Omega_{\rm WDM}h^2)^{1/3}\left(\frac{1.5}{g_D}\right)^{1/3}\left(\frac{\rm keV}{m_{\rm WDM}}\right). \tag{1.2}$$

Therefore, WDM can be an interesting candidate to solve some parts of the small scale challenges, in particular TBTF problem. Macciò et al. (2012) argue that to create typical core sizes observed in galaxies ($M \sim 10^{10}\,{\rm M}_\odot$), a WDM mass of $m_{\rm WDM} \lesssim 0.1\,{\rm keV}$ is needed. Such a requirement is at strong tensions with complementary constraints from Lyman-α forest (Viel et al. 2005), Milky-Way satellite galaxy counts (Tan et al. 2025), strong gravitational lensing images (Gilman et al. 2023). The constraint on the mass can only be relaxed if WDM was a fraction of the total dark matter budget (Viel et al. 2005, Tan et al. 2025). Despite WDM being capable of alleviating some tensions, it is clear that not all of DM can be WDM if it were to potentially resolve all the small-scale crisis.

Wave dark matter

Wave dark matter is a subclass of DM models which has wave-like characteristics in astrophysical systems. These are particles of bosonic nature and due to this they can have high occupation numbers allowing them to have coherent wave-like behaviour (Hui 2021). The evolution of collisionless particle like DM is described by the collisionless Boltzmann equation. On the other hand, collisionless wave like DM is described by the Schrödinger-Poisson equation. This serves as the key difference when simulating them (Schive et al. 2014a). The phenomenology of wave dark matter is rich, and it can solve TBTF, missing satellites, by suppressing the power in the small scales of the linear power spectrum due to wave like behaviour (Hu et al. 2000). The wave-like behaviour of these candidates leads to the formation of cores in the centre of the density profile, dubbed soliton cores (Schive et al. 2014b). The size of the soliton core is inversely related to the mass of the DM particle (Li et al. 2021). Therefore, a lower limit on the mass can be placed. S.-R. Chen et al. (2017) find that a mass in order of 10^{-22} eV to be consistent with observations and any lower would lead to larger cores than observed. In addition, independent probes have also placed similar constraints by measuring Milky-Way satellite abundances, satellite mass, density profile of SPARC galaxy dataset and Lyman-α forest constraints (see. Table 1 in Hui 2021). Similar to particle DM, wave DM can also be cold or warm, therefore warm wave dark matter can have free streaming effects (Amin et al. 2024, Liu et al. 2025).

Self-interacting dark matter (SIDM)

All the models discussed so far neglected the possibility of DM having self-interactions. D. N. Spergel et al. (2000) proposed that DM that can scatter off each other non-gravitationally can alleviate the small-scale challenges. Even in the scenario when DM is completely decoupled from Standard Model (SM), astrophysical phenomenology can still serve as an experimental ground for testing and constraining these models. In addition to it solving small-scale challenges it has also been considered as a prospective solution to reconcile ΛCDM with high redshift SMBH observations (Balberg et al. 2002b, Pollack et al. 2015, Choquette et al. 2019, W.-X. Feng et al. 2025, Sabarish et al. 2025). Moreover, SIDM also has been shown to be capable of explaining the observations of LRDs (Jiang et al. 2025). In the following sections, SIDM will be explored in greater detail.

1.2 Particle physics aspects of SIDM

A lot of DM models can exhibit self-interactions. The nature of the interaction can lead to considerably different phenomenology. For a majority of these models, astrophysical observations constrain their parameter space. Before reviewing some of these models, some integrated cross-sections that are of importance to both SIDM modelling and kinetic theory in general is discussed.

1.2.1 Integrated cross-sections

For any scattering process, the full angular and energy dependence is captured by the differential cross-section $\mathrm{d}\sigma/\mathrm{d}\Omega$. An integrated cross-section that is often discussed is the total cross-section,

$$\sigma_{\rm tot} = \int \mathrm{d}\Omega \frac{\mathrm{d}\sigma}{\mathrm{d}\Omega}. \tag{1.3}$$

Naively the larger the total cross-section more probable the scattering event will be. In simulations, the larger cross-section requires smaller time steps as discussed in **section 1.5**. This makes simulating models where the total cross-section diverges very expensive. As an example consider a differential cross-section that is forward peaked. In a single scattering event the momentum transferred is small, but since the $\sigma_{\rm tot}$ is large there are many such scattering events within a unit time. Physics of such interactions can be captured well by momentum transfer cross-section (σ_T). It is a well known quantity in kinetic theory and plasma physics (Vincenti et al. 1965, Pitaevskii et al. 1981, Bittencourt 2013, Pert 2021). The convention used in SIDM models also accounts for the fact that DM particles are identical (Kahlhoefer et al. 2017), and is given by,

$$\sigma_T = 2\pi \int \frac{\mathrm{d}\sigma}{\mathrm{d}\Omega}(1 - |\cos\theta|)\,\mathrm{d}\cos\theta. \tag{1.4}$$

Tulin et al. (2013), Boddy et al. (2014) recommend using the viscosity cross-section. The angular weighting picks out the angle perpendicular to initial direction the most, and it is well known that this angular averaging captures the effects of conductivity, and viscosity (Vincenti et al. 1965, Pitaevskii et al. 1981). It is given by,

$$\sigma_V = 2\pi \int \frac{\mathrm{d}\sigma}{\mathrm{d}\Omega}(1 - \cos^2\theta)\mathrm{d}\cos\theta. \tag{1.5}$$

More recently D. Yang et al. (2022) simulated isolated DM halo with full $\mathrm{d}\sigma/\mathrm{d}\Omega$ and also with the corresponding σ_T and σ_V. They found that simulations run with the full $\mathrm{d}\sigma/\mathrm{d}\Omega$ agree well with the ones performed with σ_V than with the ones performed with σ_T. However, σ_T is still crucial for modelling forward peaked scatterings as discussed in Kahlhoefer et al. (2014), Fischer et al. (2021).

Finally, it is also possible to integrate out both the velocity, and angular dependencies with an integral weighted with the factor by $v^n(1-\cos^2\theta)$, i.e. ,

$$\sigma_{\mathrm{eff,n}} = \frac{\int v^2 \mathrm{d}v \mathrm{d}\cos\theta \frac{\mathrm{d}\sigma}{\mathrm{d}\Omega} v^n (1-\cos^2\theta) \exp - \frac{v^2}{4(\sigma_{\mathrm{1D}}^{\mathrm{eff}})^2}}{\int v^2 \mathrm{d}v \mathrm{d}\cos\theta v^n (1-\cos^2\theta) \exp - \frac{v^2}{4(\sigma_{\mathrm{1D}}^{\mathrm{eff}})^2}}, \tag{1.6}$$

here $\sigma_{\mathrm{1D}}^{\mathrm{eff}}$ is characteristic velocity dispersion of the isolated halo of interest. D. Yang et al. (2022), Outmezguine et al. (2023), S. Yang et al. (2023) propose $n = 5$ to accurately capture the effects of heat conduction, and they verify it with simulations. In fact, it has already been known in kinetic theory that conductivity is related to the inverse of $\sigma_{\mathrm{eff,5}}$ (Pitaevskii et al. 1981). Thus, effectively the evolution of an isolated halo under $\mathrm{d}\sigma/\mathrm{d}\Omega$ can be mapped to the evolution of the same system under a constant cross-section $\sigma_{\mathrm{eff,n}}$. However, this works only for isolated systems, and the moment the evolving system has a preferential direction like in a merger, this mapping breaks down as shown in Sabarish et al. (2024).

1.2.2 Particle physics models for SIDM

The simplest model conceivable is that of scalar DM (ϕ), where the self-interactions arise through quartic coupling $\mathcal{L}_{\mathrm{int}} \sim -\lambda\phi^4$, where λ is the self-coupling constant (Bento et al. 2000, McDonald 2002, Hochberg et al. 2015). Such an interaction is essentially a single four-point vertex diagram, therefore there is no velocity dependence in the total cross-section. A shortcoming of the simple self-coupled scalar model is that observations highlight the viability of velocity-dependent cross-sections (Correa 2021, Sagunski et al. 2021), therefore velocity-independent models have been becoming less popular. To have a viable scalar DM candidate, a more sophisticated model needs to be considered. For example, a complex scalar DM that self-interacts via dark-photon (Balan et al. 2025). This model can have cross-sections with both velocity dependence and independence depending on the mediator mass.

SIDM could be a composite state made of strongly-interacting-massive particles (SIMP). Plenty of models have been proposed along these lines, see Kribs et al. (2016) for a review of these models. In the low-energy limit for an interaction with a finite range, a, the cross-section is dominated by the s-wave contribution. Thus, cross-section for these models are approximately $\sigma \sim a^2$. However, these models can still be salvaged, i.e. they can have velocity dependence when the range a exceeds the de Broglie wavelength of SIDM particles, leading to the condition $ma \gg 1$. Naturally to satisfy the above criteria, either the mass can be made large $m \gg a^{-1}$ (Boddy et al. 2014), or the range can be made large $a \gg m^{-1}$ (Cline et al. 2014a).

SIMP like interactions could also lead to the formation of dark atoms of effective size a_0, when an additional massless $U(1)'$ gauge symmetry is considered (Mohapatra et al. 2002, Khlopov 2006, Cyr-Racine et al. 2013). Similar to the earlier arguments, the cross-section can be made velocity dependent by having dark atoms have de Broglie wavelength smaller than a_0(Chu et al. 2020b).

Dissipative self-interactions can be realized in SIDM models where SIDM particles transition between two states. Some examples that were discussed earlier in this section are atomic DM, and SIMPs. A simple model that can fit this requirement is when fermionic DM charged under $U(1)'$ gauge symmetry (Finkbeiner et al. 2007, Arkani-Hamed et al. 2009, Slatyer 2010). If the symmetry is broken, then the new mass term splits DM into two states with different masses. The scattering cross-section has been calculated using phase-shift analysis in Schutz et al. (2015), Blennow et al. (2017).

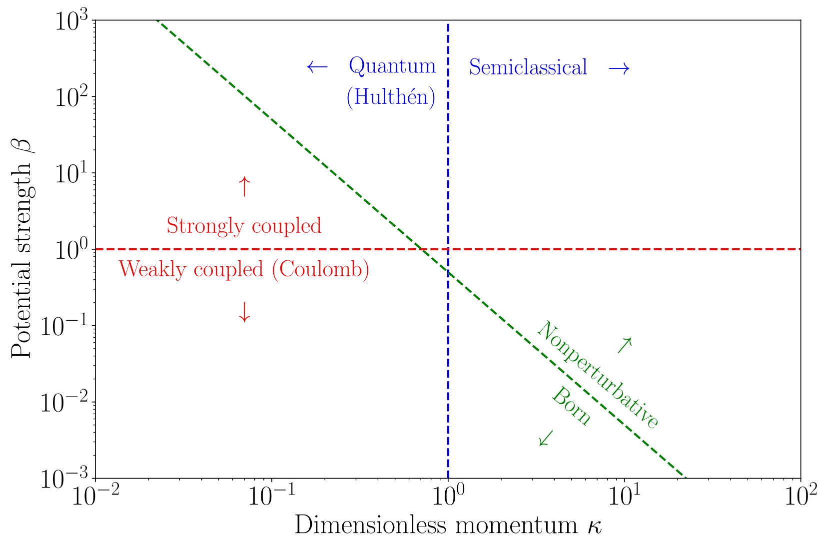

Figure 1.3: Parameter space of the Yukawa model delineated into different regions. Plot taken from Colquhoun et al. (2021).

Ferimonic DM (χ) of mass m_χ can have self-interactions mediated by scalar (ϕ) or a vector boson (ϕ_μ) of mass m_ϕ with the respective interaction terms $\mathcal{L}_{\rm int} \sim g_\chi \bar{\chi}\chi\phi$, $\mathcal{L}_{\rm int} \sim g_\chi \bar{\chi}\gamma^\mu \chi \phi_\mu$. Here, g_χ is the coupling constant. In the non-relativistic limit both of these interaction terms can be approximated by the Yukawa potential,

$$V(r) = \pm \alpha_\chi \frac{e^{-m_\phi r}}{r}, \tag{1.7}$$

here m_ϕ is the mass of the mediator, $\pm$ corresponds to repulsive or attractive potential, $\alpha_\chi = g_\chi^2/4\pi$. Scalar mediator always leads to an attractive potential, while for the vector mediator, DM is charged under $U(1)'$, therefore it can be either attractive or repulsive. This model has been studied extensively in the context of astrophysical simulations. The parameter space of this model can be delineated into different regions based on the parameters $\kappa = m_\chi v_{\rm rel}/m_\phi$ and $\beta = 2\alpha_\chi m_\phi/m_\chi v_{\rm rel}^2$ as shown in **Fig. 1.3**. In the perturbative Born regime and non-relativistic limit, the cross-section can be calculated directly from the tree-level diagram or using phase-shift analysis (Girmohanta et al. 2022). The differential cross-section is,

$$\frac{\mathrm{d}\sigma}{\mathrm{d}\Omega} = \sigma_0 \frac{\sin\theta}{2\left[1 + \frac{v^2}{w^2}\sin^2\frac{\theta}{2}\right]^2}. \tag{1.8}$$

In the above equation, $\sigma_0 := 4\pi{\alpha_\chi}^2 m_\chi^2/m_\phi^4$, $w := m_\phi/m_\chi$. Moreover, phase-shift analysis can be used also in the non-perturbative parameter space, therefore the cross-section can be calculated numerically over the full parameter space (Buckley et al. 2010, Tulin et al. 2013a, Tulin et al. 2013b, Colquhoun et al. 2021). Analytical expressions in the classical regime ($\kappa \gg 1$) can be adapted from standard results for plasma collisions (Khrapak et al. 2003, Khrapak et al. 2004, Fortov et al. 2005). In the quantum regime, analytic approximations for the scattering cross-section have been obtained in Tulin et al. (2013) using the Hulthén approximation (Cassel 2010). Finally, Colquhoun et al. (2021) derived analytic approximations that are valid in the semi-classical regime. In addition, certain parts of the parameter space for the attractive potential can also exhibit resonance (Tulin et al. 2013b, Chu et al. 2019, Gilman et al. 2023). Although these models produce observationally motivated velocity-dependent cross-sections, they face challenges (Bringmann et al. 2017) in meeting cosmological constraints (Poulin et al. 2017, Duerr et al. 2018, Hufnagel et al. 2018, Forestell et al. 2019). However, resolution to these challenges have also been proposed by either changing the production mechanism, or by having the temperature of the thermal bath of DM different from that of SM (Hambye et al. 2020).

A model agnostic parameterization of self-interaction cross-section was proposed in Chu et al. (2020). The parameterization employs the effective range formalism due to Bethe (1949) and is a generic theory applicable to low energy, finite range potentials. The total cross-section is parameterized by the set of parameters a_ℓ, r_ℓ. Here, a_ℓ is the effective scattering length, and r_ℓ is the effective range of interaction. Chu et al. (2020) show for a variety of SIDM models, that the model parameters can be mapped to the effective parameters corresponding to s-wave scattering, a_0, r_0. Since only s-wave is considered, the method fails for regions of the parameter space of the model where higher order partial waves are required. For e.g., in the case of Yukawa interaction, this parameterization is only valid as long as $\kappa < 1$.

Finally, it is worth emphasizing that there are two generic limiting cases in SIDM models, one where the total cross-section is divergent, and the scattering is anisotropic and the other where the total cross-section is finite and is either isotropic or mildly anisotropic. The former case due to the large cross-section leads to more scattering events in unit time, and the anisotropic nature leads to smaller momentum transfers, therefore it is called *frequent* self-interactions, while the latter has larger momentum transfers and is rarer, therefore it is called *rare* self-interactions (Kahlhoefer et al. 2014). For example, frequent self-interactions can arise in the massless mediator limit of the Yukawa model, while rare self-interactions with slightly anisotropic cross-section can arise if the mediator is massive. In the extreme limit $m_\phi \gg m_\chi$, rare self-interactions become isotropic, and they will be called *rare-isotropic*. It is worth highlighting that, in literature whenever rare self-interactions have constant cross-section, it is implicitly implied that they are dealing with *rare-isotropic* limit.

1.3 Astrophysical simulations

In this section the methodology of astrophysical simulations will be discussed. To begin with any astrophysical system is a collection of numerous particles with or without collisions. Most of the arguments here follow from the classics on this topic, Chapman et al. (1970), Pitaevskii et al. (1981), Cercignani et al. (1994), Mehran Kardar (2007). In classical statistical mechanics, it is well known that a collection of N particles, evolving under a total Hamiltonian H, follows the Liouville equation,

$$\frac{\partial \rho}{\partial t} = \{H, \rho\}. \tag{1.9}$$

In the above equation $\rho(\boldsymbol{x}_1, \boldsymbol{x}_2, \ldots, \boldsymbol{x}_N; \boldsymbol{p}_1, \boldsymbol{p}_2, \ldots, \boldsymbol{p}_N, t)$ is the full $6N$ dimensional phase space distribution. The Hamiltonian can be split into three parts, the kinetic energy, potential energy $U(\boldsymbol{x}_i)$ due to some background (e.g. gravitational field), and the inter-particle potential $V(\boldsymbol{x}_i - \boldsymbol{x}_j)$ responsible for collisions.

$$H = \sum_{i=1}^{N} \left[\frac{\boldsymbol{p}_i^2}{2m} + U(\boldsymbol{x}_i) \right] + \frac{1}{2} \sum_{(i,j)=1}^{N} V(\boldsymbol{x}_i - \boldsymbol{x}_j). \tag{1.10}$$

More than often, it is sufficient to have only 1-particle density. 1-particle distribution marginalizes over the knowledge of the labels of particles, and it describes the expectation value of finding any one of the N particles at the position and momentum $\boldsymbol{x}, \boldsymbol{p}$. In other words,

$$f_1(\boldsymbol{x}, \boldsymbol{p}, t) := \left\langle \sum_{i=1}^{N} \delta^3(\boldsymbol{p} - \boldsymbol{p}_i) \delta^3(\boldsymbol{x} - \boldsymbol{x}_i) \right\rangle \tag{1.11}$$

$$= N \int \Pi_{k=2}^{N} \mathrm{d}^3 \boldsymbol{x}_k \mathrm{d}^3 \boldsymbol{p}_k \rho(\boldsymbol{x}_1 = \boldsymbol{x}, \boldsymbol{x}_2, \ldots, \boldsymbol{x}_N; \boldsymbol{p}_1 = \boldsymbol{p}, \boldsymbol{p}_2, \ldots, \boldsymbol{p}_N, t), \tag{1.12}$$

here the averaging denotes an ensemble average, i.e. $\langle f \rangle \sim \int f \, \rho \, \mathrm{d}\Gamma$, where the integral is over the whole $6N$ dimensional phase space. The second equality is obtained assuming that ρ is symmetric under the exchange of particle indices, i.e. $i \leftrightarrow 1$. In astrophysics, the 1-particle density is of primary interest. For example, the number density at a given spatial location can be computed from it. This can be seen from what follows,

$$n(\boldsymbol{x},t) := \left\langle \sum_{i=1}^{N} \delta^3(\boldsymbol{x}-\boldsymbol{x}_i) \right\rangle \tag{1.13}$$

$$= \sum_{i=1}^{N} \int \Pi_{j=1}^{N} \mathrm{d}^3\boldsymbol{x}_j \mathrm{d}^3\boldsymbol{p}_j \delta^3(\boldsymbol{x}-\boldsymbol{x}_i)\rho(\boldsymbol{x}_1,\boldsymbol{x}_2,\ldots,\boldsymbol{x}_N;\boldsymbol{p}_1,\boldsymbol{p}_2,\ldots,\boldsymbol{p}_N,t) \tag{1.14}$$

$$= \int \mathrm{d}^3\boldsymbol{p}_1 f_1(\boldsymbol{x},\boldsymbol{p}_1,t). \tag{1.15}$$

The first equality physically amounts to saying that the average number of particles at the position $\boldsymbol{x}$ across different realizations of the system gives the number density at that point. In the second equality the definition of ensemble average has been used, and in the third the definition for the 1-particle density given in **Eq. (1.12)** is used. Thus, the familiar expression for number density is recovered. In a similar spirit s-particle density $f_s(\boldsymbol{x}_1,\ldots\boldsymbol{x}_s,\boldsymbol{p}_1\ldots\boldsymbol{p}_s)$ was first introduced in Yvon, Jacques et al. (1935), to capture the information on the joint distribution of s particles. Yvon, Jacques et al. (1935), Bogoliubov (1946), Born et al. (1946), Kirkwood (1946), Green (1952) used the s-particle densities along with the Liouville equation, and derived an infinitely long hierarchical list of coupled integro-differential equations. This is the famous Bogoliubov Born Green Kirkwood Yvon (BBGKY) hierarchy. Effectively, what has been done is that a single differential equation with infinite variables has been replaced with a set of infinite differential equations. For brevity, it is not derived explicitly, but only the first equation in this hierarchy for any two particles 1 and 2 is given below,

$$\left[\frac{\partial}{\partial t} - \frac{\partial U}{\partial \boldsymbol{x}_1}\cdot\frac{\partial}{\partial \boldsymbol{p}_1} + \frac{\boldsymbol{p}_1}{m}\cdot\frac{\partial}{\partial \boldsymbol{x}_1}\right] f_1 = \int dV_2 \frac{\partial V(\boldsymbol{x}_1-\boldsymbol{x}_2)}{\partial \boldsymbol{x}_1}\cdot\frac{\partial f_2}{\partial \boldsymbol{p}_1}. \tag{1.16}$$

The terms inside the square bracket on the LHS is total derivative $\mathrm{d}/\mathrm{d}t$. The hierarchy has the trend in which $\partial f_n/\partial t$ depends on f_{n+1}. The LHS of the above equation describes the time evolution of f_1, and the RHS captures the effect of collisions. It does not come as a surprise that the time evolution of f_1 depends on f_2 since f_2 contains the information on correlations between positions and momenta of any two particles. To truncate the series, a very simple approximation can be made and that is to assume that only binary collisions are relevant, and higher order collisions can be neglected. In other words, the only equation we need to solve is the one given above, provided an expression for f_2 is known. An ansatz for f_2 follows from demanding that the colliding particles are uncorrelated until before the collision, i.e. $f_2(\boldsymbol{x}_1,\boldsymbol{x}_2,\boldsymbol{p}_1,\boldsymbol{p}_2,t) = f_1(\boldsymbol{x}_1,\boldsymbol{p}_1,t)f_1(\boldsymbol{x}_2,\boldsymbol{p}_2,t)$. Therefore, from here onwards, phase space distribution f will strictly refer to the 1-particle distribution f_1 unless explicitly stated otherwise. Finally, the inter-particle potential V in the collision integral can be replaced with the differential cross-section with the help of scattering theory. Therefore, the equation finally takes the familiar form of the collisional-Boltzmann equation with some further algebra,

$$\frac{\mathrm{d}f(\boldsymbol{x},\boldsymbol{p},t)}{\mathrm{d}t} = \int \mathrm{d}^3\boldsymbol{p}_1\mathrm{d}\Omega\,\frac{d\sigma}{d\Omega}|\boldsymbol{p}-\boldsymbol{p}_1|\left[f(\boldsymbol{p}',\boldsymbol{x},t)f(\boldsymbol{p}_1',\boldsymbol{x},t) - f(\boldsymbol{p},\boldsymbol{x},t)f(\boldsymbol{p}_1,\boldsymbol{x},t)\right] \tag{1.17}$$

$$= C[f]. \tag{1.18}$$

The main assumptions in the derivation of Boltzmann equation are point-like particles, molecular chaos, negligible higher order collisions (a passing remark is that **Eq. (1.9)** is time reversible, while the approximated Boltzmann equation is irreversible). This limit in which Boltzmann equation can be derived from Liouville equation is called the Boltzmann-Grad limit (Grad 1949, Lanford 1975). The last two assumptions will break down in the case of very dense fluids. For moderately dense fluids made of particles with finite size, the Boltzmann equation has been extended to an empirical Enskog kinetic equation (Chapman et al. 1970, Van Beijeren et al. 1973, Garzó et al. 1999). However, more than often in astrophysics, DM distributions are very sparse and hence these approximations remain valid.

1.4 Simulations of collisionless particles

In the early universe, when the density and velocity perturbations were small the collisional-Boltzmann equation can be solved for these perturbations. ΛCDM cosmology in the linear regime has been covered in detail in many review articles and textbooks (Ma et al. 1995, Piattella 2018, Dodelson et al. 2020, Baumann 2022). Therefore, the focus will mostly be on the non-linear evolution at late stages of a ΛCDM universe. For collisional DM however, the effects on the linear matter power spectrum will be discussed in **section 1.6.4**.

1.4.1 N-Body simulations

To study the CDM in the non-linear regime, the collisionless Boltzmann equation, $\mathrm{d}f/\mathrm{d}t = 0$ must be solved. In addition to CDM particles, stars in galaxies and galaxies in galaxy clusters can be treated to be approximately collisionless. For such collisionless particles, the evolution of the N particles can be deduced from a smooth gravitational potential $\phi(\boldsymbol{x},t)$ arising due to all N-particles (Chandrasekhar 1941, Chandrasekhar 1960, Binney et al. 2008) as long as the relaxation time of the system is much larger than simulation time. Despite the simplifications done so far, solving the Boltzmann equation is still a daunting task. In N-body simulations, the equation is solved by letting a realization of $f(\boldsymbol{x},\boldsymbol{p},t)$ evolve under the gravitational potential $\Phi(\boldsymbol{x})$ due to all the simulation particles, (Hockney et al. 1988, Springel 2016). Consider the sampled phase space density $(\hat{f})$,

$$\hat{f}(\boldsymbol{x},\boldsymbol{p},t) = \sum_{i=1}^{N}\delta^3(\boldsymbol{p}-\boldsymbol{p}_i)\delta^3(\boldsymbol{x}-\boldsymbol{x}_i). \tag{1.19}$$

In practice this amounts to sampling the mass density profile $\rho_{\rm mass}(\boldsymbol{x})$ for the positions and the velocity distribution $f_{\rm vel}(\boldsymbol{v})$ for the velocities. Every individual sample $(\boldsymbol{x}_i, \boldsymbol{p}_i)$ can be thought of as a numerical particle. Procedurally N-body simulations mimic the evolution of f through the evolution of these numerical particles. That is, at each time-step, compute the potential due to the N particles, and update the positions and velocities accordingly. The justification that this works can be seen from what follows. Upon expanding the total derivative, the collisionless Boltzmann equation can be written as,

$$\hat{f}(t+dt) = \hat{f}(t) + \mathrm{d}t\left[\frac{\partial H}{\partial p_i}\frac{\partial}{\partial x_i} - \frac{\partial H}{\partial x_i}\frac{\partial}{\partial p_i}\right]\sum_{i=1}^{N}\delta(p-p_i)\delta(x-x_i) \tag{1.20}$$

$$= \sum_{i=1}^{N}\delta(p-p_i)\delta(x-x_i) + \left[\mathrm{d}x_i\frac{\partial}{\partial x_i} - \mathrm{d}p_i\frac{\partial}{\partial p_i}\right]\delta(p-p_i)\delta(x-x_i) \tag{1.21}$$

$$= \sum_{i=1}^{N}\delta(p-p_i-\mathrm{d}p_i)\delta(x-x_i-\mathrm{d}x_i) - O(\mathrm{d}x^2, \mathrm{d}p^2, \mathrm{d}x\mathrm{d}p). \tag{1.22}$$

In the above equations the dimensionality of the phase space has been reduced to 2 from 6 for simplicity. In the second equality the Hamilton's equation of motion, and in the final equality expansion for the product of Dirac delta functions have been used. The Taylor expansion of the Dirac delta distribution can be justified by approximating the function as a Gaussian of small width. In summary, the value of $\hat{f}(t+\mathrm{d}t)$ can be obtained by evolving the discrete numerical particles, i.e. $(x_i, p_i) \to (x_i + \mathrm{d}x_i, p_i + \mathrm{d}p_i)$, where $\mathrm{d}x_i, \mathrm{d}p_i$ are given by Hamilton's equations of motion.

Due to the finite resolution of the sampling of the phase space, these numerical particles can be very massive. Therefore, the gravitational potential can be arbitrarily large if these particles are very close. In practice, this leads to two major artefacts, *(i)* the required time stepping becomes arbitrarily small *(ii)* due to artificially high masses two body gravitational collisions can become more pronounced. Both of these artefacts can be addressed by "softening" the force by introducing a length scale ϵ below which the $F_{\rm grav}$ is suppressed (Aarseth 1963). Despite the fact that softening reduces the gravitational relaxation time by suppressing close binary encounters, there will still be gravitational relaxation due to long range interactions arising from the artificial discreteness of the sampled system (Dehnen 2001, Dehnen et al. 2011). It has been shown that the overall relaxation timescale of the N-body system under these modified potentials changes at the most by $O(1)$ from Chandrasekhar's relaxation time as long as the softening length is approximately the mean inter-particle distance (Theis 1998).

1.5 Simulations of collisional DM

To understand the effects of SIDM on structures theoretically, the collisional Boltzmann equation **Eq. (1.18)** needs to be solved. To this end, there are different schemes in which the problem can be tackled. The above equation can be solved by the expensive N-body formalism, or relatively cheaper gravothermal fluid formalism. A slightly more empirical approach to deduce the evolution of DM haloes is the semi-analytic method called isothermal formalism. In this thesis, N-body and the fluid methods are used.

1.5.1 N-body Simulations of SIDM

The challenge in simulating particle scattering processes in an astrophysical context is tackled by adopting a Lagrangian Monte-Carlo method. Such simulations have been employed to study SIDM haloes since the 2000s. It was first achieved by Burkert (2000), and to be quickly followed by Kochanek et al. (2000), Yoshida et al. (2000), Craig et al. (2001), Davé et al. (2001), Colín et al. (2002), D'Onghia et al. (2003) Most of the modern N-body codes for SIDM use a method similar to the one in Rocha et al. (2013). The collisional-Boltzmann equation as given in **Eq. (1.18)** can be written in terms of velocities ($\boldsymbol{v}$) instead of momenta as,

$$\frac{\mathrm{d}f(\boldsymbol{x},\boldsymbol{v},t)}{\mathrm{d}t} = \int \mathrm{d}^3\boldsymbol{v}_1\mathrm{d}\Omega\,\frac{d\sigma}{d\Omega}|\boldsymbol{v}-\boldsymbol{v}_1|\left[f(\boldsymbol{v}',\boldsymbol{x},t)f(\boldsymbol{v}_1',\boldsymbol{x},t) - f(\boldsymbol{v},\boldsymbol{x},t)f(\boldsymbol{v}_1,\boldsymbol{x},t)\right]. \tag{1.23}$$

In the above equation, all the other symbols except $\boldsymbol{v}$ are the same as in the previous section. The N-body method essentially discretizes the collisional-Boltzmann equation. Therefore, similar to the discretization assumed in **Eq. (1.19)**, the one particle phase space distribution is represented as,

$$\hat{f}(\boldsymbol{x},\boldsymbol{v},t) = \sum_i \left(\frac{M_i}{m}\right) W(|\boldsymbol{x}-\boldsymbol{x}_i|;h_i)\delta^3(\boldsymbol{v}-\boldsymbol{v}_i). \tag{1.24}$$

Here i labels the i-th numerical particle of mass M_i. For velocity, a Dirac-delta distribution is assumed, while for the position a smooth kernel function $W(\boldsymbol{x})$ with kernel length h_i is assumed. The kernel function of finite support is essential to compute the overlap of phase space regions to calculate the effects of scattering. Since the Lagrangian numerical particles are a discretization of the phase space, the corresponding discretized Boltzmann equation is obtained by integrating **Eq. (1.23)** over a phase space patch for a given particle k, where the integration domain is given by the intervals $\delta\boldsymbol{x}_k$ and $\delta\boldsymbol{v}_k$. Since we are interested in the post-scattering state of the particle p, only the scattering out part of collision operator is considered. Scaling the collision operator by m/M_k is required to ensure that the scattering rate calculated corresponds to the numerical particle of mass M_k. Denoting the net scattering experienced by particle k as $\Gamma(k)$,

$$\Gamma(k) = (m/M_k)\int_{\delta x_k}\mathrm{d}^3\boldsymbol{x}\int_{\delta v_k}\mathrm{d}^3\boldsymbol{v}\int \mathrm{d}^3\boldsymbol{v}_1\mathrm{d}\Omega\,\frac{d\sigma}{d\Omega}|\boldsymbol{v}-\boldsymbol{v}_1|\hat{f}(\boldsymbol{v},\boldsymbol{x},t)\hat{f}(\boldsymbol{v}_1,\boldsymbol{x},t). \tag{1.25}$$

Upon substituting **Eq. (1.24)** in the above equation and simplifying,

$$= (m/M_k) \int_{\delta x_k} d^3\boldsymbol{x} \int_{\delta v_k} d^3\boldsymbol{v} \int d^3\boldsymbol{v}_1 \int d\Omega \frac{d\sigma}{d\Omega} |\boldsymbol{v} - \boldsymbol{v}_1| \Bigg\{ \sum_j (M_j/m) W(|\boldsymbol{x} - \boldsymbol{x}_j|; h_j) \delta^3(\boldsymbol{v} - \boldsymbol{v}_j)$$
$$\sum_i (M_i/m) W(|\boldsymbol{x} - \boldsymbol{x}_i|; h_i) \delta^3(\boldsymbol{v}_1 - \boldsymbol{v}_i) \Bigg\}$$
$$= \sum_j (\sigma/m) M_j \left|\mathbf{v}_j - \mathbf{v}_k\right| \Lambda_{kj} := \sum_j \Gamma(k, j). \tag{1.26}$$

Here Λ_{kj} is the kernel overlap integral which is defined as,

$$\Lambda_{kj} = \int_{\delta x_k} \mathrm{d}\boldsymbol{x}^3 W(|\boldsymbol{x} - \boldsymbol{x}_k|; h_k) W(|\boldsymbol{x} - \boldsymbol{x}_j|; h_j). \tag{1.27}$$

Given that **Eq. (1.26)** is the scattering rate, then the probability that particle k and j scatter can be trivially calculated as $\Gamma(k, j)\Delta t$. Moreover, it is in principle possible that within a given time step, there can be many particles j can have their kernels overlap with the one that of k. This implies that there can be multiple scatterings within a single time step.

Given some initial conditions and a particular particle k, algorithmically this amounts to first finding a kernel size h_k such that there are $N_{\rm ngb}$ neighbouring particles. In the simulations performed in this thesis, a spline kernel has been used (Monaghan et al. 1985). In some implementations, the kernel size h_i is the same for all particles (Vogelsberger et al. 2012, Rocha et al. 2013).

For time stepping, it must be small enough that the probability of scattering stays well below identity. A. Robertson et al. (2017) recommend using small enough of time step that only one scattering event takes place within Δt for keeping numerical errors in energy to a minimum. More recently Fischer et al. (2021) use a scheme that allows multiple scatterings per time step but still ensure energy conservation.

In the discussion so far, only constant cross-sections (σ/m) were considered, but it can be extended to differential cross-sections $(\mathrm{d}\sigma/\mathrm{d}\Omega)$ with angular and velocity dependence (A. Robertson et al. 2017a, A. Robertson et al. 2017b). Some more modern implementations of SIDM within N-body simulations can be found in Correa et al. (2022), D. Yang et al. (2022).

Practical difficulties with N-body methods are that the simulations are expensive, and they get prohibitively expensive for differential cross-sections that have a maximum for small scattering angles. It is in this limit, that SIDM can be simulated with an effective drag-force approach due to Kahlhoefer et al. (2014). This method has been implemented in OpenGadget3 in Fischer et al. (2021).

1.5.2 Gravothermal fluid formalism

The gravothermal fluid formalism solves by approximating the collisional-Boltzmann equation by its first three velocity moments and is applicable for binary collisions of any nature. One assumption commonly made is that the system is spherically symmetric. This method was first applied to stellar systems which evolve under binary gravitational collisions by Lynden-Bell et al. (1968), Lynden-Bell et al. (1980). This method was eventually adapted to SIDM, and some early studies in this direction include (Gnedin et al. 2001, Balberg et al. 2002a, Balberg et al. 2002b, Ahn et al. 2005).

In this subsection, the general formalism will be discussed and eventually specialized to SIDM haloes. In the absence of the collisional operator, taking moments of the Boltzmann equation becomes trivial, i.e. the moments of the LHS essentially become the mass, momentum and energy conservation equations (Binney et al. 2008, Mo et al. 2010). At first sight, taking moments of the collision operator might look daunting, however moments of binary collisional operator is strictly zero (Pitaevskii et al. 1981). This is due to the fact that certain quantities called summation invariants $Q(\boldsymbol{v})$, which are functions of velocity that are conserved during a single binary collision (Chapman et al. 1970). Typically, these correspond to linear momentum, and kinetic energy. The statement can be written as, $\int C[f]\; Q(\boldsymbol{v})\; \mathrm{d}^3\boldsymbol{v} = 0$ for $Q(\boldsymbol{v}) \sim 1, v, v^2$. Therefore, the moments of the collisional equation can be shown to be the standard fluid equations,

$$\frac{\partial \rho}{\partial t} + \nabla \cdot (\rho \boldsymbol{v}) = 0, \tag{1.28}$$

$$\frac{\partial \rho \boldsymbol{v}}{\partial t} + \nabla \cdot (\rho \boldsymbol{v}\boldsymbol{v} + P) = 0, \tag{1.29}$$

$$\frac{\partial E}{\partial t} + \nabla \cdot [(E + P)\, \boldsymbol{v} + \boldsymbol{q}] = 0, \tag{1.30}$$

here $\boldsymbol{q}$ is the heat flux vector, P is the pressure, $\boldsymbol{v}$ is the bulk velocity vector, $\boldsymbol{g}$ is the acceleration experienced by the fluid parcels, ρ is the mass density, and E is the total energy density defined as,

$$E = e + \frac{1}{2}\rho \boldsymbol{v}^2, \tag{1.31}$$

where e is the internal energy density. Note that the RHS of the fluid equations could contain additional acceleration source terms (e.g. due to gravity), and the geometric source terms are implicit here.

Since the fluid equations are independent of the binary collision operator, the above equations are applicable in both collisional and collisionless regimes. The regimes are identified based on the ratio of mean-free-path (λ) of collisions to the characteristic size (H) of the system. One defines the Knudsen number as (Knudsen 1909, Steckelmacher 1986),

$$\mathrm{Kn} = \frac{\lambda}{H}. \tag{1.32}$$

For astrophysical systems, the characteristic length $H(\boldsymbol{x})$ is given by the size of a typical orbit or equivalently the local Jeans length. In the case of collisional fluids like gas, $\mathrm{Kn} \ll 1$. Pressure arises due to frequent collisions. This is also called the short-mean-free-path (SMFP) regime. In this case, the pressure is responsible for maintaining *hydrostatic equilibrium* against gravity. For weakly collisional systems, i.e. $\mathrm{Kn} \gg 1$, there is no collisional pressure and velocity dispersion provides an effective pressure that maintains *virial equilibrium*. This regime is often dubbed as long-mean-free-path (LMFP) regime. The intermediate regime, i.e. $0.1 \lesssim \mathrm{Kn} \lesssim 10$ is the intermediate-mean-free-path (IMFP) regime.

It is also worth emphasizing that astrophysical systems typically have inhomogeneity in temperature, velocity and mass distributions leading to dissipative processes like conduction and viscosity. In particular heat conduction plays a significant role in self-gravitating systems (Lynden-Bell et al. 1968). An expression for heat conduction in the SMFP can be derived from first principles using Chapman-Enskog expansion due to Chapman (1912), Chapman (1916), Enskog (1917). Using this expansion leads to the following form for heat flux vector for a spherically symmetric system (Pitaevskii et al. 1981, D. Yang et al. 2022),

$$\boldsymbol{q} = \kappa_{\mathrm{SMFP}} \nabla T \tag{1.33}$$

$$\approx 2.1 k_B \frac{\sigma_{\mathrm{1D}}}{\sigma} \nabla T. \tag{1.34}$$

Here, k_B is the Boltzmann constant, σ_{1D} is the RMS velocity dispersion and σ is the cross-section corresponding to the binary collisions. On the other hand in LMFP, there is only an empirical formula for conduction due to Lynden-Bell et al. (1980). It was later adapted to SIDM models with constant isotropic cross-section, the heat flux vector in this case is given as (Balberg et al. 2002b),

$$\boldsymbol{q} = \kappa_{\mathrm{LMFP}} \nabla T \tag{1.35}$$

$$= \frac{3}{2} k_B \beta \rho \frac{H(r)^2}{t_r^2} \frac{\partial \sigma_{\mathrm{1D}}^2}{\partial r} \nabla T. \tag{1.36}$$

In the above expression, β is a dimensionless parameter that has to be calibrated against N-body simulations, t_r is the relaxation timescale set by the collisions.

Note that up until the derivation has been agnostic about the nature of collisions. For SIDM, $t_r = t_{\mathrm{SIDM}} \sim 1/\rho\sigma_{\mathrm{1D}}\sigma_m$. Here, $\sigma_m := \sigma/m_{\mathrm{DM}}$ is the cross-section per unit mass. It is also known that β has been calibrated to be of order unity, and in the range 0.5 to 1.0 (Koda et al. 2011, Essig et al. 2019, S. Yang et al. 2023a). For DM, $T = m_{\mathrm{DM}}\sigma_{\mathrm{1D}}^2/k_B$, $e = (3/2)\sigma_{\mathrm{1D}}^2$, $P = \rho\sigma_{\mathrm{1D}}^2$. In addition, for most haloes, the bulk velocity of DM ($\boldsymbol{v}$) is much smaller than the velocity dispersion (σ_{1D}), i.e. $\boldsymbol{v} \ll \sigma_{\mathrm{1D}}$. This simplifies the equations to the standard form for gravothermal equations,

$$\frac{\partial M}{\partial r} = 4\pi r^2 \rho, \tag{1.37}$$

$$\frac{\partial(\rho\sigma_{1\mathrm{D}}^2)}{\partial r} = -\frac{\mathrm{G}M\rho}{r^2}, \tag{1.38}$$

$$\frac{\partial q}{\partial r} = 4\pi r^2 \rho\sigma_{1\mathrm{D}}^2 \left[\frac{D}{Dt}\left(\frac{3}{2}\sigma_{1\mathrm{D}}^2\right) + P\frac{D}{Dt}\left(\frac{1}{\rho}\right)\right], \tag{1.39}$$

$$q = -m_{\mathrm{DM}}\kappa(\sigma)\frac{\partial\sigma_{1\mathrm{D}}^2}{\partial r}. \tag{1.40}$$

where $\kappa(\sigma)$ has different expressions in SMFP, LMFP and IMFP.

The ODE system can be fully specified once the parameters ρ_s, r_s, σ_m are known. The solutions to this set of ODEs in the LMFP are self-similar and that the solutions obtained for one parameter set can be rescaled to obtain the solution corresponding to any-other parameter set. The method discussed so far considered only constant cross-sections. It has been extended recently to velocity dependent models (Outmezguine et al. 2023, S. Yang et al. 2023a)

1.5.3 Isothermal Jeans formalism

Scattering between DM particles can lead to heat transport as highlighted in the earlier subsection. Such a process can lead to the formation of a core (see. **section 1.6.2** for more details). Therefore, it is expected that the inner regions form a core, while the outer regions are NFW-like. The transition radius r_1 is a characteristic radius within which DM particles would have experienced at least one scattering event over the lifetime of the halo (Kaplinghat et al. 2016).

$$\frac{4}{\sqrt{\pi}}\rho(r_1)\sigma_{1\mathrm{D}}(r_1)\sigma_m = \frac{1}{t_{\mathrm{age}}}. \tag{1.41}$$

Therefore, the DM profile can be written as,

$$\rho(r) = \begin{cases} \rho_{\mathrm{iso}}(r), & r < r_1 \\ \rho_{\mathrm{NFW}}(r), & r > r_1 \end{cases} \tag{1.42}$$

ρ_{iso} can be easily obtained by solving the Jeans equation in spherical coordinates along with the Poisson equation, i.e. ,

$$\frac{\mathrm{d}}{\mathrm{d}r}\rho(r)\sigma_{1\mathrm{D}}(r)^2 + \frac{2\beta}{r}\sigma_{1\mathrm{D}}(r)^2 = -\rho(r)\frac{\mathrm{d}\Phi}{\mathrm{d}r}, \tag{1.43}$$

$$\nabla^2\Phi(r) = 4\pi\mathrm{G}\rho_{\mathrm{total}}. \tag{1.44}$$

In the above equation, Φ is the total gravitational potential, ρ_{total} is the total matter density including both baryons and DM, ρ is the DM density, β is the anisotropy parameter in the Jeans model. It is typically assumed that the $\sigma_{1D}(r)$ is isotropic and is constant, i.e. $\sigma_{1D}(r) = \sigma_{1D}$, and $\beta = 0$. Given these assumptions, Jeans equation admits a simple generic solution for DM density profile for $r < r_1$ as,

$$\rho_{\rm iso}(r) = \rho_0 \exp\left[\frac{\Phi(r) - \Phi(0)}{\sigma_{1D}^2}\right]. \tag{1.45}$$

To solve the Poisson equation, a baryonic profile is still required. It is commonly assumed to be a Hernquist profile (Kaplinghat et al. 2014, Kaplinghat et al. 2016, Jiang et al. 2023), or to be a thin disk (Kamada et al. 2017). An additional effect that needs to be accounted for is adiabatic contraction (Blumenthal et al. 1986, Gnedin et al. 2004, Gnedin et al. 2011), i.e. the contraction experienced by the initial NFW profile due to the presence of the baryons at the halo centre. Algorithmically this amounts to the following *(i)* compute the contracted NFW profile due to the presence of baryons *(ii)* find r_1 using **Eq. (1.41)** for the modified NFW profile *(iii)* integrate the Poisson equation assuming some values for ρ_0 and σ_{1D} - repeat this step iteratively until the $\rho_{\rm iso}$ stitches smoothly to the outer profile at r_1.

1.6 Astrophysical Effects of SIDM

In this section, the physical effects of self-interactions on astrophysical systems are discussed in increasing length scales.

1.6.1 Dark matter spikes

On the smallest length scales around black holes, DM is expected to accumulate forming dense spikes. It was first proposed by Gondolo et al. (1999) assuming Newtonian gravity. It was then extended to be consistent with General relativity by Sadeghian et al. (2013). Both of these works converge on the profile $\rho \sim r^{-\gamma}$. For an NFW profile, they show that $\gamma \approx 7/3$. On the other hand for SIDM, spikes can only exist if such a profile can be a solution to the gravothermal equations. Shapiro et al. (2014) argue that $\gamma = 3 + a/4$ for SIDM with the cross-section $\sigma \sim v^{-a}$. The first self-consistent verification of the formation of SIDM spikes in N-body simulations, for $a = 0$ case can be found in **chapter 3**. An interesting observable signal from DM spikes is that the presence of the spike can affect the orbital dynamics of SMBH inspirals, or extreme mass-ratio inspirals (EMRI) leading to different gravitational wave signatures (C. Feng et al. 2026). For a detailed introduction see **section 3.2**.

1.6.2 Isolated dark matter haloes

DM haloes grow through two major processes, *(i)* accretion *(ii)* hierarchical mergers. If there are self-interactions then during these processes energy can be transferred from one region to another. For cross-sections $\lesssim 2\,\mathrm{cm^2\,g^{-1}}$, the SIDM relaxation timescale is much larger than the dynamical timescale of the halo, that the self-interactions play a little role in the formation phase of haloes. Therefore, it is very reasonable to assume that evolution follows CDM like halo formation. Once the halo has formed, the effects of self-interactions kick-in on larger timescales.

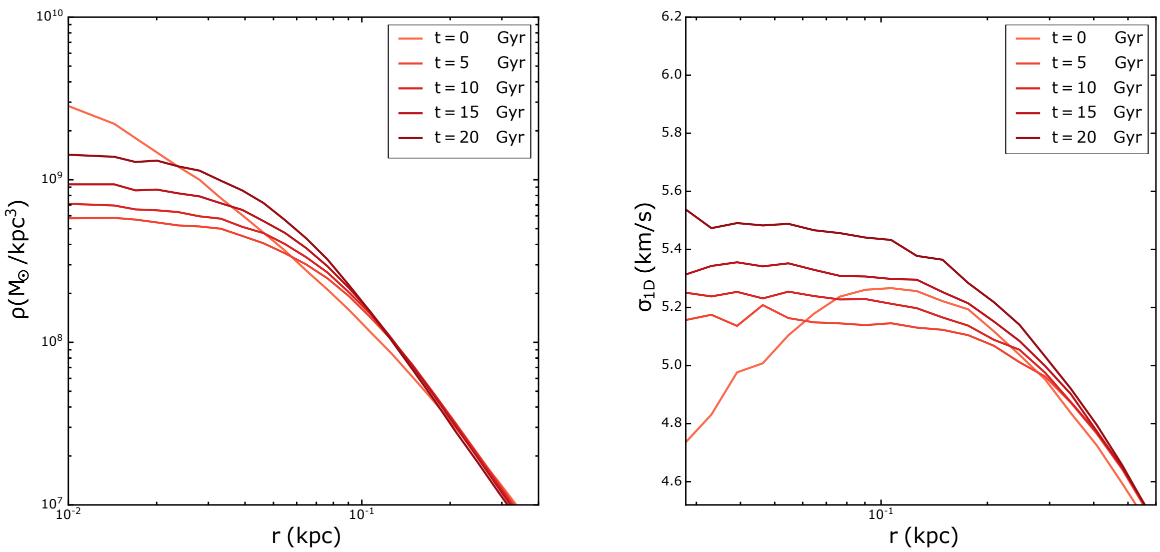

Figure 1.4: Evolution of an isolated NFW halo using N-body simulations. The host halo has a $r_s \sim 0.1$ kpc, $\rho_0 \sim 10^8\,\mathrm{M_\odot\,kpc^{-3}}$, and$M_{200} \sim 10^7\,\mathrm{M_\odot}$. SIDM model considered is the Yukawa model, and the full differential cross-section (see. **Eq. (1.8)**) is simulated. In the left and right panel the density and RMS velocity dispersion are shown respectively. The system has initial NFW profile, and evolves into an isothermal profile. Figure adapted from D. Yang et al. (2022), licensed under CC BY.

For an NFW halo, the velocity dispersion has a positive gradient in the innermost region, and for larger radius it has a negative gradient. Therefore, from **Eq. (1.40)** it can be seen that there will be a heat flow towards the centre. **Fig. 1.4** shows the evolutions of an NFW halo with the parameters $r_s \sim 0.1$ kpc, $\rho_0 \sim 10^8\,\mathrm{M_\odot\,kpc^{-3}}$, and $M_{200} \sim 10^7\,\mathrm{M_\odot}$. The left panel shows the evolution of density profile, while the right one shows that of the RMS velocity dispersion. Due to self-interactions and the fact that conductivity is proportional to the gradient in $\sigma_{1\mathrm{D}}$, energy will flow from outer regions to the inner regions, thermalizing it. On a timescale of approximately $100 t_{\mathrm{SIDM}}$, the central density reaches the lowest value. This feature can be seen in both the panels in **Fig. 1.4**, as density drops and velocity dispersion increases. This initial phase is called the core formation case. Once the core is formed, the halo starts transitioning into the second phase. Since the $\sigma_{1\mathrm{D}}$ gradient is no longer positive in the inner regions, heat flow from the outskirts stops. Eventually, the gradient becomes negative, and the core starts losing energy. Since gravitating systems have negative heat capacity (Binney et al. 2008), the core gets hotter as it loses energy. Therefore, this sets the stage for the gravothermal collapse. On a longer timescale, $t_{\mathrm{collapse}} \sim 300\ t_{\mathrm{SIDM}}$, the halo starts collapsing.

1.6.3 Merging galaxy clusters

In a merger, there are two major observables that are sensitive to the effects of self-interactions. First one being mass evaporation, and the second being effective drag experienced by dark matter component, i.e. $\dot{M} = -\mu_e M$ and $\dot{v} = -\mu_d v$. Here, μ_e, μ_d are the evaporation and deceleration rates and are given as, (Kahlhoefer et al. 2014, Kummer et al. 2018),

$$\mu_e = f_e \rho v^{p(2-p)}, \quad \mu_d = f_d \rho v^{p(2-p)}. \tag{1.46}$$

where ρ is the background density through which the test particle is moving, v is the velocity of test particle with respect to the background, $p = -1$ for frequent self-interactions, and $p = 1$ for rare self-interactions, f_d and f_e are functionals with the differential cross-section as an argument. In general there are two regimes that needs to be factored in during the calculation of evaporation rates, *(i)* immediate evaporation, that is if a particle is kicked out of the halo in scattering event *(ii)* cumulative evaporation, that is a particle kicked eventually after multiple scattering events. In both these regimes, the evaporation rates are formally identical, but the difference lies in f_e.

For rare self-interactions, $f_d \sim \sigma_{\rm tot}$, $f_e \sim \sigma_{\rm tot}$ while for frequent case, it not only depends on the model parameters but also on the logarithm of the minimum scattering angle. Effects of isotropic-rare, and frequent self-interactions limits has been discussed in depth in Kahlhoefer et al. (2014). DM only merger simulations comparing both these limits were first done in Fischer et al. (2021), Fischer et al. (2022), eventually they were performed also including baryons in Fischer et al. (2023). Within rare self-interactions, it is possible to have some angular dependence, and Kummer et al. (2018), show that anisotropic cross-sections tend to have lesser evaporation than isotropic ones.

1.6.4 Linear matter power spectrum

All of WIMP like CDM candidates are in the non-relativistic regime during matter domination. Cyr-Racine et al. (2016) show using perturbed Boltzmann equation that, a model with only DM $\leftrightarrow$ DM scattering (also assuming that DM is non-relativistic during structure formation) will not modify the linear matter power spectrum. Therefore, in cosmological SIDM simulations where the model only contains DM-DM scattering, it is reasonable to start with a CDM-like initial matter power spectrum for ICs. To introduce modifications to the linear matter power spectrum, it is required that DM also scatters of a relativistic species (RS), i.e. DM RS $\leftrightarrow$ DM RS. This could be DM interacting with photons (Sigurdson et al. 2004, Boehm et al. 2014), dark photons (Holdom 1986, Bœhm et al. 2001, Ackerman et al. 2009), neutrinos (Bœhm et al. 2002, Wilkinson et al. 2014), other types of dark radiation (van den Aarssen et al. 2012, Bringmann et al. 2014). It is worth noting that in all of these models, if there is any additional relativistic component it must satisfy the $N_{\rm eff}$ bounds coming from CMB and BBN. Alternatively, the linear spectrum can be modified by considering self-interacting warm dark matter (SIWDM) (Yunis et al. 2020, Egana-Ugrinovic et al. 2021, Garani et al. 2022).

In a series of papers Cyr-Racine et al. (2016), Vogelsberger et al. (2016), Bose et al. (2019), Bohr et al. (2020), a model agnostic parameterization called ETHOS was proposed that captures the effects of DM interactions with a relativistic species. In the ETHOS parameterization, the particle physics model parameters are mapped to ETHOS parameters, and then the corresponding modified linear matter power spectrum can be calculated using modified CAMB provided by the authors or by using its implementation in CLASS (Archidiacono et al. 2017). In Vogelsberger et al. (2016), the first set of zoom-in simulations within the ETHOS framework was run. The effects of DM-DR scatterings were captured in the ICs by realizing the modified power-spectrum on a cosmological grid, and then non-linear effects of DM-DM scatterings were captured by N-body scattering algorithm as discussed in **section 1.5**. More recently, Nadler et al. (2025) ran zoom-in simulation of a similar setup, but pushing the simulation until gravothermal collapse happens. One of the main findings of this paper is that the population of core-collapsed subhaloes is reduced when simulations start with an initial $P(k)$ that features extreme suppression. This trend continues i.e. , with reduced $P(k)$ suppression, the population of subhaloes that collapses increases.

1.7 Constraints

In this section, existing constraints on σ_m along with the analysis methodologies are summarized. In **Fig. 1.5**, different constraints obtained on σ_m at different velocity scales are shown. Results pertaining to specific SIDM models are discussed without showing a plot of the constrained parameter space.

Dark matter spikes

Constraints from DM spikes have become an area of active research only in recent years. Tiruvaskar et al. (2025) is one of the first papers that highlighted the possibility to constrain a cross-section of the type $\sigma \sim (w/v)^4$. As discussed in **section 1.7**, the presence of SIDM can have an influence on the GWs produced at SMBH mergers. Therefore, they use the NANOGrav (Agazie et al. 2023) data to constrain SIDM.

Although not a constraint, Alonso-Álvarez et al. (2024) claim that SIDM is required to explain the GW background signal observed by NANOGrav and PPTA (Reardon et al. 2023). The argument is two-fold, *(i)* dynamical friction from DM be it CDM or SIDM is required to ensure that the binary SMBH can lose energy when they are separated by a distance of $\sim$ 1 pc. Without this mechanism, it will take a Hubble time to cross the final parsec. *(ii)* During the initial phase of the inspiralling of SMBHs, energy injected into the DM spike via dynamical friction can completely disrupt the CDM spike. Therefore, without this friction, the merging process practically comes to a halt. However, the presence of SIDM can enable the transport of the injected energy to outskirts of the spike and eventually to the host halo preventing the disruption of the spike. This ensures the sustainment of the DM spike, leading to a merger on shorter timescales.

Dwarf scale

At the lowest velocity scale/mass scale dwarf galaxies exist. Carignan et al. (1988), Flores et al. (1994), Moore (1994) were some of the earliest works that found that many dwarves and LSB galaxies better fit a cored density profile than to an NFW profile. Correa (2021) gravothermally

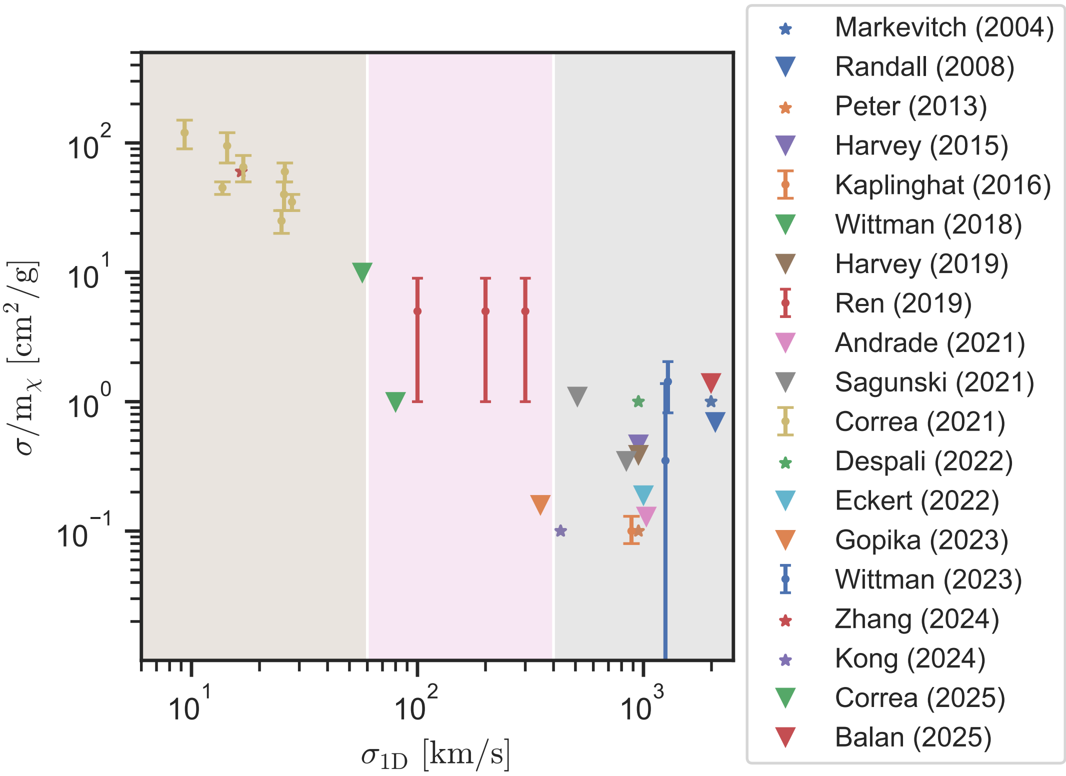

Figure 1.5: Constraints on σ_m across different velocity scales. Inverted triangles refer to upper bounds (it can be either 95% or 98%), stars refer to single values of cross-sections simulated that are favoured/consistent with observations, points with error bars are ranges of σ_m that is favoured/consistent with observations.

evolve the Milky Way satellites along their orbits also accounting for tidal stripping. They showed that a σ_m in the range 50 to 100 $\mathrm{cm^2\,g^{-1}}$ is required to be consistent with observations. Slone et al. (2023) do a similar analysis but also accounting for more physical effects like dynamical friction and ram pressure evaporation of dark matter due to interactions. They constrained the parameter space (σ_0, w) of the Yukawa model (see **Eq. (1.8)**). In the above discussed two constraints, the orbital parameters for the satellites are taken from GaiaDR2(Fritz et al. 2018). Robustness of these results can improve with smaller uncertainties in the measured orbital parameters as highlighted by Correa (2021).

Zhang et al. (2024) quote a value of $\sigma_m \approx 60\,\mathrm{cm^2\,g^{-1}}$ for the Milky Way satellite Crater II to be consistent with observations (Caldwell et al. 2017, Ji et al. 2021, Pace et al. 2022). They capture the tidal effects accurately by performing N-body simulations of the satellite falling into the host which is modelled as a static gravitational potential.

Milky Way scale

Similarly, at the scale of Milky Way type galaxies there are no robust constraints. Ren et al. (2019) fit the rotation curves expected from SIDM's isothermal-Jeans model to observations from the SPARC dataset (Lelli et al. 2016) and find that a $\sigma_m \approx 3$ to $10\,\mathrm{cm^2\,g^{-1}}$ is needed to explain the observations. However, Zentner et al. (2022) show that SIDM is not preferred over CDM+Baryons using the same SPARC dataset, and that it is merely consistent with observations. Therefore, it is safe to state that SIDM requires $\sigma_m \approx 3$ to $10\,\mathrm{cm^2\,g^{-1}}$ to be consistent with observations at these scales.

At the same scales, Correa et al. (2025) find that by comparing the observed Tully-Fisher relation to hydrodynamical simulations with SIDM (Correa et al. 2022) and the SWIFT-EAGLE galaxy formation model (Crain et al. 2015, Schaye et al. 2015, Bahé et al. 2022, Borrow et al. 2023) an upper limit of $\sigma_m \approx 0.5\,\mathrm{cm^2\,g^{-1}}$ and $10\,\mathrm{cm^2\,g^{-1}}$ at $\langle v_{rel} \rangle \approx 130\,\mathrm{km\,s^{-1}}$ and $180\,\mathrm{km\,s^{-1}}$ respectively.

Kong et al. (2024) showed that for slightly larger mass scales a $\sigma_m \approx 0.1\,\mathrm{cm^2\,g^{-1}}$ is favoured. They employed the isothermal-Jeans model to explain the strong lensing object JWST-ER1 found by van Dokkum et al. (2024).

Groups and cluster scale

At group and cluster scales, the constraints are more robust. The most stringent constraints on the cross-section are due to the observations of inner density profiles of galaxy clusters. Andrade et al. (2021) place an upper limit on σ_m of $0.13\,\mathrm{cm^2\,g^{-1}}$ by comparing the core sizes of 8 galaxy clusters to the predictions of the isothermal-Jeans model. Core sizes were inferred from lensed images of the cluster. Using a similar analysis method, Sagunski et al. (2021) analyse 7 galaxy clusters (Newman et al. 2013a, Newman et al. 2013b) and place $\sigma_m < 0.35\,\mathrm{cm^2\,g^{-1}}$, but they also take into account the adiabatic contraction of the host haloes. In addition, they also consider galaxy group scale objects provided in (Newman et al. 2015) to obtain an upper bound of $\sigma_m < 1.1\,\mathrm{cm}^2\,\mathrm{g}^{-1}$.

Eckert et al. (2022) propose a fitting relation between σ_m and the Einasto profile parameter α using simulation data (A. Robertson et al. 2021). Using this fitting relation, along with the observed density profiles of 12 galaxy clusters (Eckert et al. 2017), they quote an upper bound of $\sigma_m < 0.19\,\mathrm{cm}^2\,\mathrm{g}^{-1}$. Identical methods were applied by Gopika et al. (2023) to galaxy groups (Zappacosta et al. 2006, Gastaldello et al. 2007) to obtain $\sigma_m < 0.16\,\mathrm{cm}^2\,\mathrm{g}^{-1}$. All the upper bounds discussed so far are at 95% confidence level (C.L.). Finally, S. Yang et al. (2023) constrain the parameter space $\sigma_0 - w$ for a velocity dependent cross-section $\sigma = \sigma_0/(1 + v^2/w^2)^2$ which is similar to the velocity dependence of the Yukawa model. The physics of SIDM is modelled using both gravothermal and isothermal-Jeans modelling. And then, they perform a joint analysis of two datasets, baryon-poor galaxies from the SPARC dataset (Lelli et al. 2016) and 7 galaxy clusters from Newman et al. (2013).

SIDM cross-sections can also be constrained with the help of galaxy cluster mergers. In this context, the Bullet cluster has been the most considered system in deriving constraints for self-interactions. To recap, the Bullet cluster is merging galaxy cluster system, where a subcluster had passed through the main cluster's central region along the plane of the sky. The mass peaks of the merging clusters were reconstructed using lensing observations (Clowe et al. 2004), while the gas distribution (Tucker et al. 1998, Markevitch et al. 2002) is observed to be hot in X-Rays.

As summarized in **section 1.6.3**, SIDM can lead to evaporation of DM haloes, formation of DM-Baryon offset and reduction in the infall velocities of the haloes. Markevitch et al. (2004) constrain the cross-section by all the three above-mentioned physical effects. They obtain an upper limit of *(i)* $\sigma_m < 5.0\,\mathrm{cm}^2\,\mathrm{g}^{-1}$ due to the absence of large DM-Galaxy offset. *(ii)* $\sigma_m < 7\,\mathrm{cm}^2\,\mathrm{g}^{-1}$ due to the large observed velocity for the subcluster ($4500\,\mathrm{km\,s}^{-1}$), implying very little drag or friction *(iii)* $\sigma_m < 1\,\mathrm{cm}^2\,\mathrm{g}^{-1}$ due to the small observed subcluster mass loss due to evaporation. The mass loss estimation is done by measuring the mass-to-light-ratio (MLR) of both the subcluster and main cluster. In this analysis, they assume both the clusters have identical initial MLRs, and they compare the assumed initial MLR to the observed one for the subcluster to place an upper bound. The assumptions on the initial MLR have been relaxed in a recent work (Balan et al. 2025) where they do Bayesian analysis and marginalize over the unknown initial MLR. They find an upper limit of $1.4\,\mathrm{cm}^2\,\mathrm{g}^{-1}$ using a Gaussian prior for the initial MLR. By using a realistic prior for the initial MLR the upper limit from evaporation constraint relaxes to $5\,\mathrm{cm}^2\,\mathrm{g}^{-1}$. By measuring a statistical average of DM-Galaxy offsets in merging galaxy clusters Harvey et al. (2015) quote an upper bound of $0.47\,\mathrm{cm}^2\,\mathrm{g}^{-1}$, while Wittman et al. (2018) looked at similar systems and estimated it to be $2\,\mathrm{cm}^2\,\mathrm{g}^{-1}$. Finally, cross-sections can also be constrained by comparing the off-centering of BCG in relaxed galaxy clusters to the ones from SIDM cosmological simulations. Using this method Harvey et al. (2019) quote an upper limit of $0.39\,\mathrm{cm}^2\,\mathrm{g}^{-1}$.

The structure of the thesis is as follows. In **chapter 2**, the effects of frequent, and rare-isotropic self-interactions with velocity dependence on galaxy cluster mergers are studied, and the results are reported. Then, in **chapter 3**, DM spikes of velocity independent SIDM are simulated using N-body simulations and an analytic expression for the accretion rate in LMFP is derived. Similarly, in **chapter 4**, hydrodynamical simulations of SIDM spike with SMFP thermal conductivity are performed, and a comparison of accretion rates across different MFP regimes is discussed. Finally, in **chapter 5**, we summarize the main results of this thesis and conclude.

2 Simulations of galaxy cluster mergers with velocity-dependent, rare and frequent self-interactions

This chapter presents work as published in Sabarish et al. (2024).

Abstract

Self-interacting dark matter (SIDM) has been proposed to solve small-scale problems in ΛCDM cosmology. In previous work, constraints on the self-interaction cross-section of dark matter have been derived assuming that the self-interaction cross-section is independent of velocity. However, a velocity-dependent cross-section is more natural in most theories of SIDM. Using idealized N-body simulations without baryons, we study merging clusters with velocity-dependent SIDM. In addition to the usual rare scattering in the isotropic limit, we also simulate these systems with anisotropic, small-angle (frequent) scatterings. We find that the collision-less brightest cluster galaxy (BCG) has an offset from the DM peak that grows at later stages. Finally, we also extend the existing upper bounds on the velocity-independent, isotropic self-interaction cross-section to the parameter space of rare and frequent velocity-dependent self-interactions by studying the central densities of dark matter-only isolated haloes. For these upper-bound parameters, the DM-BCG offsets just after the first pericentre in the dark matter-only simulations are found to be $\lesssim 10\,\mathrm{kpc}$. On the other hand, because of BCG oscillations, we speculate that the distribution of BCG offsets in a relaxed cluster is a statistically viable probe. Therefore, this motivates further studies of BCG off-centring in hydrodynamic cosmological simulations.

2.1 Introduction

Cold dark matter (CDM) is a fundamental component of the standard ΛCDM cosmology. It plays a vital role in explaining the formation of the large-scale structure of the universe and the anisotropies in the cosmic microwave background. While cosmological N-body simulations within ΛCDM have successfully reproduced many observations of the large-scale structure, there seem to be discrepancies between observations and simulations on small scales (see Bullock et al. (2017) for a review of the small-scale problems). A solution to the small-scale problems was proposed by D. N. Spergel et al. (2000) via a model of DM, where DM particles can non-gravitationally scatter off each other. Constraints on the self-interaction cross-section can be obtained by studying different astrophysical systems. In particular, relaxed galaxy clusters (e.g., Andrade et al. 2021, Sagunski et al. 2021) have provided the most stringent constraint on the cross-section. We also have constraints from galaxy cluster mergers (Randall et al. 2008, Harvey et al. 2015). For a review on astrophysical constraints on self-interacting dark matter (SIDM) see Adhikari et al. (2022).

Velocity-dependent anisotropic cross-sections are natural in most theories of SIDM (for a review of SIDM models see Tulin et al. 2018). Examples of such models include light mediator models (Ackerman et al. 2009, Tulin et al. 2013a), atomic DM (Cline et al. 2014b), strongly interacting DM (Boddy et al. 2014). Moreover, velocity-dependent cross-sections are also well motivated observationally. Most constraints on the self-interaction cross-section per unit mass of DM particle (σ/m_χ) in the literature, have been derived assuming velocity-independent and isotropic scattering. For example, Sagunski et al. (2021) quote an upper limit of $\sigma/m_\chi < 0.35\,\mathrm{cm}^2\,\mathrm{g}^{-1}$(95%C.L.) at cluster scales and $\sigma/m_\chi < 1.1\,\mathrm{cm}^2\,\mathrm{g}^{-1}$(95%C.L.) at group scales. On the galactic scales, Ren et al. (2019) find that σ/m_χ is required to be in the range 3-10 $\mathrm{cm}^2\,\mathrm{g}^{-1}$ to explain the observed diversity in the rotation curves in the SPARC data set. Similarly, Sankar Ray et al. (2022) quote an upper-bound of $\sigma/m_\chi < 9.8\,\mathrm{cm}^2\,\mathrm{g}^{-1}$(95%C.L.). At the scale of dwarf galaxies, there is no concrete upper bound on the cross-section. A cross-section with $\sigma/m_\chi > 30\,\mathrm{cm}^2\,\mathrm{g}^{-1}$ is favoured by the observed central densities of Milky Way's dwarf spheroidal galaxies (Correa 2021). Elbert et al. (2015) find that σ/m_χ can be as large as $50\,\mathrm{cm}^2\,\mathrm{g}^{-1}$ at these scales and still be consistent with observations. These considerations highlight the viability of velocity-dependent cross-sections.

Observationally probing the angular dependence is a daunting task. One reason being that the effects of angular dependence are not strong enough when studying the evolution of systems that do not have a preferred direction. For example, A. Robertson et al. (2017) and Fischer et al. (2021) simulated isolated haloes using N-body simulations and found that there is no big difference in the evolution of core-sizes between isotropic and anisotropic cross-sections for a given choice of parameters. Moreover, simulating differential cross-sections which peak for tiny scattering angles, using conventional SIDM implementations (e.g. Rocha et al. 2013) is prohibitively expensive. This type of interaction will be called frequent self-interactions (as introduced in Kahlhoefer et al. 2014) as opposed to rare self-interactions corresponding to large-angle scattering. Frequently self-interacting dark matter (fSIDM) is natural in the mass-less mediator limit of light mediator models. The scattering of DM particles in this regime can be modelled as a drag force, where the drag force depends not on the total cross-section but on the momentum transfer cross-section given by Kahlhoefer et al. (2017) and A. Robertson et al. (2017)

$$\sigma_\mathrm{T} = 2\pi \int_{-1}^{1} \frac{\mathrm{d}\sigma}{\mathrm{d}\Omega_\mathrm{cms}} (1 - |\cos\theta_\mathrm{cms}|)\, \mathrm{d}\cos\theta_\mathrm{cms}. \tag{2.1}$$

where θ_{cms} and Ω_{cms} are the scattering angle, and solid angle in the centre of mass frame. Frequent self-interactions have previously been studied by Kahlhoefer et al. (2014),Kummer et al. (2018), Kummer et al. (2019),Fischer et al. (2021), Fischer et al. (2022) assuming velocity independence.

Mergers of galaxy clusters are interesting test beds for models of SIDM since the mass distribution of the system could be measured through lensing. The gas and galaxies can be probed through their direct emission in various wavelengths. The existence of offsets between the DM component and galaxies may hint at DM self-interactions (Randall et al. 2008). Moreover, mergers are sensitive to both velocity and angular dependence of the scattering cross-section. First, as the haloes undergo many pericentre passages, the collisional velocity changes with time. Scattering velocities are the largest at the first pericentre passage and, subsequently, the haloes slow down with every passage. The self-interactions at the pericentre passages are mainly responsible for an increase in the offset. Thus, the evolution is sensitive to the parameters of velocity-dependent cross-section. Secondly, mergers unlike isolated haloes also have a preferred direction, i.e. the merger axis. Fischer et al. (2022) find that offsets are larger for frequent self-interactions with a given σ_{T}, when compared to rare self-interactions of the same σ_{T}. They also showed that small-angle scattering can produce larger offsets than the maximal possible offset from isotropic scattering. There have been earlier studies that have simulated mergers. For example, studies with velocity-independent isotropic cross-sections have been done by S. Y. Kim et al. (2017) who simulated equal-mass mergers ; A. Robertson et al. (2017) simulated a bullet cluster like system. Fischer et al. (2021), Fischer et al. (2022) studied equal and unequal-mass mergers with isotropic and anisotropic velocity-independent cross-sections. A. Robertson et al. (2017) looked at mergers until just after the first pericentre passage. They used a velocity-dependent isotropic cross-section and a velocity-dependent cross-section that corresponds to Yukawa scattering under the Born approximation. It is unknown as to how the merger evolution is affected at late stages by velocity-dependent self-interactions. Similarly, mergers in the fSIDM regime with velocity dependence are yet to be studied. In this work, we aim to *(i)* study the qualitative differences in merger simulations between velocity-dependent and independent cross-sections, *(ii)* extend the upper bound on constant cross-section quoted by Sagunski et al. (2021) to the parameter space of velocity-dependent cross-section, *(iii)* find the maximum offsets between DM and the brightest cluster galaxy (BCG) with velocity-dependent cross-section parameters that are consistent with upper bound parameters. To this end, we simulate the full evolution of galaxy cluster mergers and isolated haloes with rare and frequent self-interactions. In a companion paper (Fischer et al. 2024b), cosmological simulations are studied with velocity-dependent fSIDM. The paper is presented as follows. In **section 2.2** we briefly describe our numerical scheme and the SIDM models that are considered. In **section 2.3** we present our simulation results, which illustrate the qualitative differences between velocity-dependent and velocity-independent cross-section simulations. In **section 2.4**, we describe the simulations of mergers with cross-section parameters that correspond to the 95% C.L. limits provided in Sagunski et al. (2021). In **section 2.5**, we summarize our results and conclude. Additional details are provided in **App. 2.B** and **App. 2.A**.

2.2 Methods

In this section, we describe the numerical setup of our simulations, and we discuss our choice for the self-interaction cross-section that is used in the simulations.

2.2.1 Numerical method

For our simulations, we use the cosmological N-body simulation code OpenGadget3, adapted for frequent self-interactions using the implementation given in Fischer et al. (2021). In this section, we briefly describe the implementation of rare and frequent self-interactions. The numerical scheme for the self-interactions of rarely self-interacting dark matter (rSIDM) follows Fischer et al. (2021), which is similar to the method described in Rocha et al. (2013). In this scheme, the probability that a numerical particle 1 with mass m_1 scatters off another numerical particle 2 with mass m_2 is given by,

$$P_{12} = \frac{\sigma(v_{12})}{m_\chi}\, m_2\, |v_{12}|\, \Delta t\, \Lambda_{12}, \tag{2.2}$$

where v_{12} is the relative velocity between the numerical particles 1 and 2, Δt is the time-step used in the simulation, Λ_{12} is the kernel overlap integral, $\sigma(v_{12})/m_\chi$ is the total cross-section per unit mass of DM particle. For more details on the implementation and the choice for the kernel, see appendix A and B of Fischer et al. (2021). A collection of kernels used in other modern implementations of SIDM within N-body simulations can be found in Adhikari et al. (2022), equations 11-15. The drag force of frequent self-interactions is based on the relation derived in Kahlhoefer et al. (2014), which describes the deceleration rate experienced by a particle as it travels through a constant background density of DM,

$$R_{\mathrm{dec}} = \frac{1}{v_0}\frac{\mathrm{d}v_{\parallel}}{\mathrm{d}t} = \frac{\rho_0 v_0 \sigma_{\mathrm{T}}}{2m_\chi}, \tag{2.3}$$

v_0 is the velocity of the particle, $v_{\parallel}$ is the parallel component of the velocity of the particle, ρ_0 is the background density, σ_{T} is the momentum transfer cross-section defined in (2.1). We can also see that the deceleration rate captures the rate of change of the parallel component of the velocity. Therefore, the above expression can then be cast into an expression for drag force for the physical particles. The drag force as experienced by numerical particles, labelled 1 and 2, in the N-body code is given as (Fischer et al. 2021),

$$F_{\mathrm{drag}} = \frac{1}{2}|v_{12}|^2 \frac{\sigma_{\mathrm{T}}(v_{12})}{m_\chi} m_1 m_2 \Lambda_{12}, \tag{2.4}$$

which is proportional to the momentum transfer cross-section σ_{T}. From here on, we will drop the subscripts and let v denote the relative velocity between DM particles.

In addition to the drag force, momentum is added to the particles in a random but perpendicular direction relative to the motion in the centre-of-mass frame. As for rSIDM, the post-scattered momenta in the centre-of-mass frame have the same absolute value as the pre-scattered ones. In our SIDM implementation, we search for pairs of potentially interacting particles. A search for the neighbours of each particle achieves this, employing the same tree structure as used in the gravity computation.

The code employs an adaptive time-stepping scheme, where the time-step of an individual particle is obtained by the minimum of different time-step criteria, i.e. given by gravity and self-interactions.

The implementation of rSIDM and fSIDM does conserve momentum as well as energy explicitly. This is achieved by executing the scattering computations for pairs of particles in a consecutive manner such that their velocities are updated after each scattering event and used for the next one. At the same time, we allow for multiple interactions per particle per time-step.

Massively parallel computations of the self-interactions are enabled by a parallelized implementation using the message passing interface (MPI). Note, here we order the communication and computation of the processes in a manner to reduce waiting time.

The implementation of the velocity-dependent self-interactions into the SIDM module has been described in detail by Fischer et al. (2024). To ensure numerically stable results, a novel time-step criterion has been added. This criterion uses the velocity at which self-interaction effects are the strongest, i.e. on the maximum of $\sigma_{\mathrm{T}}(v)\, v$, instead of the velocity distribution that an individual particle encountered in the previous time-step. In principle, such a scheme guarantees that the simulation time-step is always sufficiently small to account for $\sigma_{\mathrm{T}}(v)$ for any v.

2.2.2 Initial conditions and simulation parameters

In this work, we simulate both DM-only isolated haloes and galaxy cluster merger with two different merger mass ratios (MMR). Firstly for the isolated DM-only haloes, they have a virial mass of $10^{15}\,\mathrm{M}_{\odot}$ and are initialized with an NFW density profile Navarro et al. (1996), i.e.

$$\rho(r) = \frac{\delta_c \rho_{\mathrm{crit}}}{(r/r_s)(1 + r/r_s)^2} := \frac{\rho_0}{(r/r_s)(1 + r/r_s)^2}. \tag{2.5}$$

DM positions are sampled from a probability density function such that the density profile follows the NFW profile. Given the virial mass of the halo and the critical density ρ_{crit} of the universe, the parameters of the NFW profile are determined as follows: *(i)* the concentration parameter c_{vir} is determined using the concentration-mass relation given in Dutton et al. (2014), *(ii)* characteristic density δ_c is computed using c_{vir} from the earlier step (using Eq.2 of Navarro et al. 1996), *(iii)* scale radius r_s is computed using its definition $r_s = r_{\mathrm{vir}}/c_{\mathrm{vir}}$. The NFW parameters thus obtained are given in **Tab. 2.1**. Using the resulting density profile, the initial velocity dispersion $\left\langle v^2 \right\rangle_{\mathrm{ini}}(r)$ is obtained by integrating the Jeans equation (Binney et al. 2008). Then, initial velocities in each radial bin are drawn from a Gaussian distribution with the variance $\left\langle v^2 \right\rangle_{\mathrm{ini}}(r)$.

Table 2.1: This table contains the NFW parameters used in generating the ICs for merger simulations. The first column contains the virial mass, the second the density parameter $\rho_0 := \delta_c\, \rho_{\rm crit}$, followed by scale radius r_s, concentration parameter and number of DM and galaxy particles. DM-only isolated haloes have the same NFW parameters as given in the first row.

$\mathrm{M_{vir}}$ ($\mathrm{M_\odot}$)	ρ_0 ($\mathrm{M_\odot\,kpc^{-3}}$)	r_s (kpc)	c	$N_{\rm DM} = N_{\rm Gal}$	$N_{\rm BCG}$
10^{15}	1.33×10^6	389.3	5.42	1009878	1
2×10^{14}	1.908×10^6	194.76	6.33	181319	1

Table 2.2: This table contains the initial separation, initial relative velocity between the two clusters and the relative velocity of the BCGs at the first pericentre passage.

Merger mass ratios ($\mathrm{M_\odot : M_\odot}$)	$x_{\rm ini}$ (kpc)	$\Delta v_{\rm ini}$ ($\mathrm{km\,s^{-1}}$)	$\Delta v^{\rm (BCG)}_{\rm FPP}$ ($\mathrm{km\,s^{-1}}$)
$10^{15} : 10^{15}$	4000	1000	5500
$10^{15} : 2 \times 10^{14}$	4000	1000	4800

The isolated DM halo simulations use the same NFW parameters as the main halo of the merger for initial conditions (ICs). We simulate mergers with MMR $\in \{1, 5\}$. The barycentre of the clusters are initially 4000 kpc apart and they are put on course towards each other with a relative velocity of $1000\,\mathrm{km\,s^{-1}}$ as summarized in **Tab. 2.2**. In the galaxy cluster used in the merger simulations, the cluster has three particle species: DM, galaxy and BCG. Galaxies and BCG are approximated to be collision-less, while DM is collisional with self-interaction characterized by its cross-section. An equal number of DM and galaxy particles is used in the simulation. A sufficient number of galaxy particles are chosen to ensure that it is easier to find the peak position of the galaxies. The main halo has a virial mass of $10^{15}\mathrm{M_\odot}$ and both species initially follow an NFW profile. The particle masses are as follows: for DM, $m_{\rm DM} = 2 \times 10^9\ \mathrm{M_\odot}$, for galaxies, $m_{\rm Gal} = 4 \times 10^7 \mathrm{M_\odot}$. In addition, the brightest cluster galaxy (BCG) is represented by a single particle at the centre of the halo with a mass $m_{\rm BCG} = 7 \times 10^{11}\ \mathrm{M_\odot}$. As the BCG is approximated to be a point particle, the effects of gravitational scattering become strong if the mass is large, therefore the BCG particle is taken to be less massive than the observed BCGs. This choice is adopted from earlier studies (e.g. S. Y. Kim et al. 2017, Fischer et al. 2022b). The mass resolution chosen works reasonably well for measuring offsets in simulation since the simulation is run only for a few dynamical time-scales. The detailed effects of such a treatment on measurements other than offsets are yet to be studied. We use a fixed gravitational softening length of $\epsilon = 1.2$ kpc for all particles. For both mergers and isolated haloes we use an adaptive kernel size for the DM self-interactions, such that the number of neighbours within each particles' kernel, $N_{\rm ngb}$ is equal to 64. This choice follows from Fischer et al. (2021). All simulations have been performed with a resolution of $\mathcal{O}(10^6)$ particles. For certain cross-section parameters, the simulations were rerun at a higher resolution of $\mathcal{O}(10^7)$ particles to validate the lower resolution runs (see Appendix **App. 2.B**).

2.2.3 Dark matter cross-section model

We assume a fairly generic form for the self-interaction momentum transfer cross-section for rare and frequent self-interactions, parametrized as follows (Gilman et al. 2021, S. Yang et al. 2023a),

$$\frac{\sigma_{\rm T}(v)}{m_\chi} = \frac{\sigma_0}{m_\chi}\left(1 + \frac{v^2}{w^2}\right)^{-2}, \tag{2.6}$$

where v is the relative velocity of the DM particles. We furthermore assume that the total

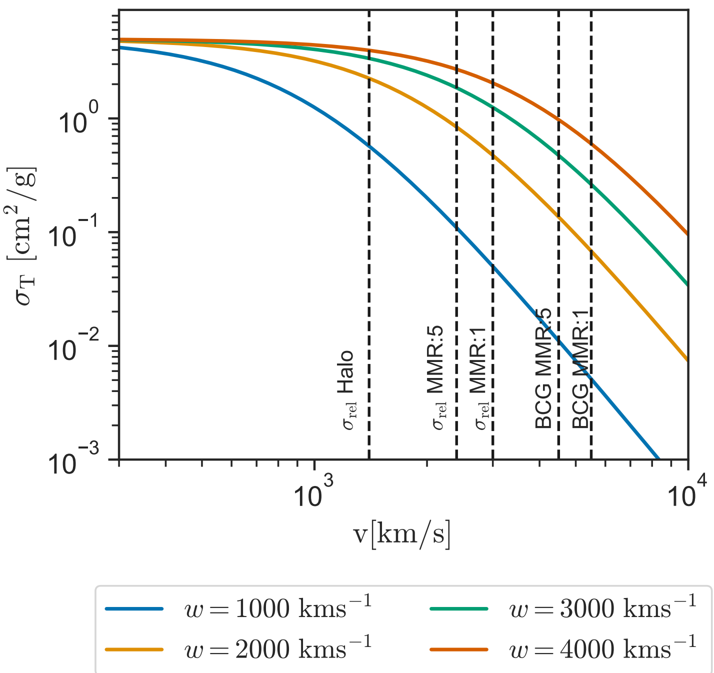

Figure 2.1: Momentum transfer cross-section for $\sigma_{0m} = 5\,{\rm cm}^2\,{\rm g}^{-1}$, and the values of w are given in the legend. The vertical coloured dashed lines correspond to different velocity scales in the system. The left most is the relative velocity dispersion within 100 kpc of the $10^{15}\,{\rm M}_\odot$ cluster. The second and third from the left correspond to the relative velocity dispersion within 100 kpc around the barycentre at the first pericentre for MMR:5 and MMR:1 respectively. Finally, the second last and the last are the relative velocity of the BCGs at the first pericentre passage of the system with MMR:5 and MMR:1, respectively.

cross-section has the same velocity dependence as the momentum transfer cross-section, such that

$$\frac{\sigma_{\mathrm{T}}(v)}{\sigma_{\mathrm{T}}(v=0)} = \frac{\sigma(v)}{\sigma(v=0)} \,. \tag{2.7}$$

This assumption is automatically satisfied if the differential cross-section is a separable function, i.e. it is of the following form,

$$\frac{\mathrm{d}\sigma}{\mathrm{d}\cos\theta} = N\frac{\sigma_0}{m_\chi}\Theta(\theta)g(w,v), \tag{2.8}$$

where N is a normalization constant, $\Theta(\theta)$ captures the angular dependence and $g(w,v) = (1+v^2/w^2)^{-2}$. However, even for non-separable differential cross-sections, such as Rutherford scattering, the assumption in (2.7) gives a useful approximation. Depending on the choice of N and $\Theta(\theta)$, the above differential cross-section can correspond to either frequent or rare self-interactions. In this work, we consider isotropic scattering for the case of rare self-interactions, such that $\Theta(\theta)$ is simply a number. The total cross-section to calculate the scattering probability in (2.2) is then given by $\sigma(v) = 2\sigma_{\mathrm{T}}(v)$, see (2.1). For frequent self-interactions, on the other hand, $\Theta(\theta)$ is strongly peaked for small angles. The normalization, N, is then chosen such that the momentum transfer cross-section given in (2.6) is recovered, which is used in the simulations to compute the drag force experienced by the particles, see (2.4).

To run the simulations, the parameters σ_{0m} and w must be chosen, where $\sigma_{0m} := \sigma_0/m_\chi$. In this paper, we are interested in studying the qualitative differences in the evolution of galaxy cluster mergers between the different regions of $\sigma_{0m} - w$ parameter space. A priori, it is conceivable that there are degeneracies in this parameter space, such that different parameter combinations lead to very similar merger observables. Such a degeneracy was found by S. Yang et al. (2023) (see their fig. 8) when analysing the rotation curve of LSB dwarf galaxy UGC 128. In other words, it was possible to compensate a change in w by an appropriate change in σ_{0m}. We refer to a prescription to determine the cross-section normalization σ_{0m} for a given velocity dependence (determined by w) as *matching*. In the following, we will explore different matching procedures. The choice for w follows from the typical relative velocity scales. These scales can be estimated by running CDM simulations. The observed values are displayed as dashed lines in **Fig. 2.1**. The largest observed scales are the relative velocities of the infalling BCGs shown as the last two lines corresponding to MMR:5 and MMR:1 respectively. The average scattering velocity with which DM particles scatter off each other within 100 kpc around the barycentre at the first pericentre passage are shown. Finally, the relative velocity dispersion within 100 kpc of a $10^{15}\,\mathrm{M}_\odot$ halo is displayed as the leftmost vertical dashed line and it is approximately $1400\,\mathrm{km\,s^{-1}}$. This implies that for any value of w larger than $1400\,\mathrm{km\,s^{-1}}$, the self-interactions within the halo will be in the weakly velocity-dependent regime. Therefore, the following choice for w is made, $w \in \{1000, 2000, 3000, 4000\}\mathrm{km\,s^{-1}}$. We have analysed cluster mergers with σ_{0m} chosen according to two matching procedures: The first is to choose the same value of σ_{0m} for all chosen values of w, the second is to choose σ_{0m} such that the evolution of the central density of the isolated haloes for different values of w is similar. These procedures will be explained further in the following sections.

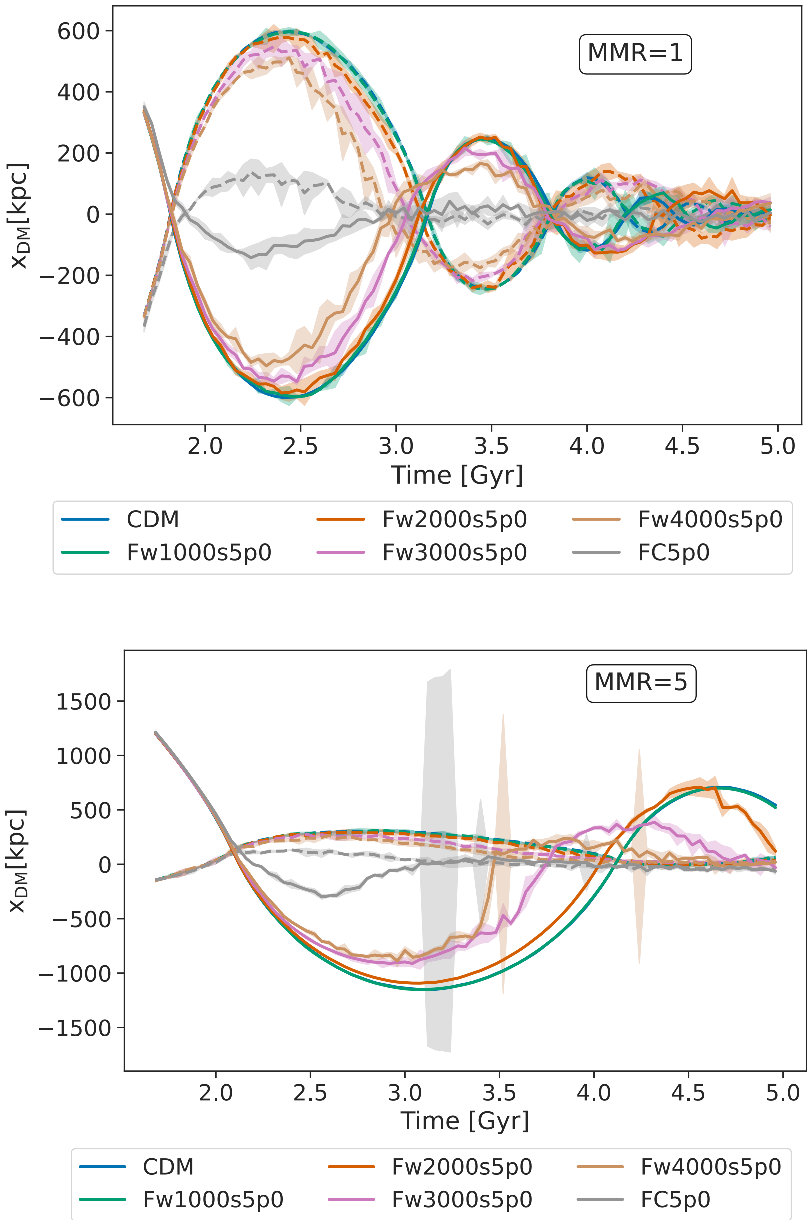

Figure 2.2: The dotted and solid lines correspond to the DM peak position of the main halo and subhalo respectively. Upper panel: DM peaks in equal-mass merger, lower panel: Merger with mass ratio 5. Plot labels are described in **Tab. 2.3**. Simulation results presented in this center corresponds to varying values of w and a fixed σ_{0m}.

.

2.2.4 Analysis methods

In order to find the peak position of any component, i.e. DM or galaxies, we use the peak finding method based on the gravitational potential, see Fischer et al. (2022). In the simulations, all particles have a unique particle ID assigned to them. Using the ID, particles belonging to a given halo can be identified. Then, the gravitational potential in each cell in a grid is computed. The cell with the lowest potential corresponds to the position of the peak. Fischer et al. (2022) also propose the isodensity-based peak finding algorithm. In this algorithm, the peaks are identified as the cell in the merger plane with the highest projected density. This method is closer to observations where, for example, gravitational shear measurements can be used to infer mass densities. We find that gravitational potential based peak finding is more reliable when the simulation is run with low resolution. Hence, this is our choice for finding peaks. To find the errors on the peak position, we bootstrap the particle distribution 20 times and determine 20 such peaks. Then we estimate the error, by finding the standard deviation in the obtained peak positions. We define offsets as the distance between the peaks of two different species of the same cluster. For example, $d_{\mathrm{DM-BCG}}$ is the distance between the DM and BCG peak of a given cluster.

2.3 Varying w only

In this scheme, the same value of σ_{0m} is used for different values of the parameter w. Even though it is a very simple choice, it is easier to observe the qualitative difference introduced by velocity-dependent cross-sections. To make the differences stand out, we use a large value of $\sigma_{0m} = 5.0\,\mathrm{cm^2\,g^{-1}}$. The results hold even for smaller values of σ_{0m}, but the qualitative differences are less pronounced. We confirmed the results to be qualitatively similar but less pronounced for smaller values of σ_{0m}. The names for the individual runs shown in the plots are tabulated in **Tab. 2.3**.

2.3.1 DM peak position

The plots of the peak positions of DM against time for equal and unequal-mass mergers are given in **Fig. 2.2**. The peaks of the main halo are marked by dotted lines, while those of subhalo are indicated by solid lines. First we observe that for constant σ_T the drag force from self-interaction is strong enough to stop the DM component in their tracks and they coalesce at the first pericentre passage. For the same σ_{0m}, the DM peak positions in the velocity-dependent SIDM runs are closer to the CDM run for smaller values of w. This observation matches our expectation that, for fixed σ_{0m}, increasing w increases the effective self-interaction strength.

The separation of the peaks at the first apocentre is largest for CDM and decreases with increasing self-interaction strength. This can be attributed to the fact that DM particles experience a drag force and thus stay closer to the centre-of-mass of the system.

Simulation name	σ_{0m} [cm^2 g^{-1}]	w [km s^{-1}]
FC5p0	5	∞
Fw1000s5p0	5	1000
Fw2000s5p0	5	2000
Fw3000s5p0	5	3000
Fw4000s5p0	5	4000

Table 2.3: Simulation labels and the corresponding cross-section parameters. The generic form of labels is XwDsNpM, where X is F(frequent), R(rare), or C(constant). D that follows w is the value of the parameter w to be read as D km s^{-1} and NpM following the s is the value of σ_{0m} to be read as N.M cm^2 g^{-1}.

The first pericentre passage occurs at different times for different parameter combinations. Albeit a small effect, self-interactions tend to increase the time taken to reach the first pericentre passage. Then the second passage occurs earlier for increasing self-interaction strength. For example, we see that the first pericentre passage occurs slightly later in the simulation with constant σ_T. This could be understood as self-interactions generating pressure that resists the infall, thus slowing the halo down. The difference is large for constant σ_T because the effective self-interaction strength of the velocity-dependent ones is much smaller than the one of constant σ_T at early stages, as $\sigma_{\mathrm{T}}(v)$ is small for $v > w$.

At later stages of the evolution, the scenario changes. For example, at the third apocentre passage, we see that the oscillation in the DM peak for $w = 2000\,\mathrm{km\,s^{-1}}$ has an amplitude that is greater than that of CDM. During these stages, the central density of the haloes are lower for SIDM simulations (see **Fig. 2.C2**). Therefore, the oscillations are less dampened by dynamical friction for SIDM simulations. For the unequal-mass mergers, the subhalo dissolves faster, making it difficult to identify the DM peaks during later stages of the evolution. Both equal and unequal mass mergers have identical initial separation and initial relative velocity. Therefore, in unequal mass merger, the less massive cluster traverses more distance than the massive one and this leads to fewer oscillations. For instance, in **Fig. 2.2**, we see that within 5 billion years, the subhalo in MMR:5 system has undergone fewer pericentre passages than the equal-mass merger.

2.3.2 BCG peak position

The BCG positions for subhaloes are given in **Fig. 2.3**, the upper panel corresponds to the equal-mass merger system, while the lower panel corresponds to the unequal-mass merger. In CDM simulations, the BCG oscillations are damped faster compared to SIDM simulations. This general feature has already been observed in earlier work (S. Y. Kim et al. 2017, Fischer et al. 2021, Fischer et al. 2022b). This could be explained by noting that the merger remnants have a cored density distribution at the centre owing to the self-interactions. On the other hand, merger remnants in CDM simulations have larger central densities. As a result, the oscillations dampen out faster in CDM due to dynamical friction.

In the equal-mass merger, we observe that the peak positions of subhalo BCGs are closer to the CDM for smaller values of w at the early stages of the merger evolution. At later stages, around 5 billion years, the BCG oscillations in the CDM simulation have dampened considerably. On the other hand, the oscillations approximately stay constant for the constant σ_{T} simulation for the period $1-8$ billion years, as shown in **Fig. 2.3**. The position of the BCG in velocity-dependent simulations start deviating from CDM with time. For example, let us consider the $w = 2000\,\mathrm{km\,s^{-1}}$ simulation : *(i)* we see that the curve is initially close to the CDM simulation *(ii)* during the period $4-7$ billion years, the oscillations have approximately a constant amplitude, and they have significantly deviated from the CDM simulation. The typical velocities around the DM peak at various stages of the evolution are given in **Fig. 2.D2**. The central relative velocity dispersion around the DM peak is large at the first pericentre owing to the active merging. At later stages, when the haloes have slowed down, they have a very slowly rising relative velocity dispersion for the rest of the simulated time period. Therefore, from **Fig. 2.1** we see that for $w = 2000\,\mathrm{km\,s^{-1}}$ and $v > 2000\,\mathrm{km\,s^{-1}}$, the σ_{T} is less than $1\,\mathrm{cm^2\,g^{-1}}$, whereas for $v < 2000\,\mathrm{km\,s^{-1}}$ the cross-section is larger than $1\,\mathrm{cm^2\,g^{-1}}$. Thus, merger remnants experience larger self-interactions at later stages, leading to more cored distributions and lesser dynamical friction. Cumulatively, this leads to steady oscillations at later stages.

The distance travelled by the BCGs at the first apocentre is observed to become smaller with increasing values of w. This can be understood by looking at the DM peaks. For example, the DM haloes coalesce at the first pericentre passage for the constant σ_T simulation. As a result, the BCG experiences a larger gravitational force due to the coalesced DM distribution at the barycentre. This accumulation of DM at the barycentre reduces with decreasing w since the average interaction strength reduces with w. This effectively leads to smaller amplitudes at the first apocentre in both equal and unequal-mass mergers. Immediately after the second pericentre passage, the amplitude of the velocity-dependent SIDM and CDM curves have decreased significantly due to dynamic friction. In the constant σ_T simulation , the DM peaks have come to rest, and the merger remnants start coring. This leads to the persistence of the BCG oscillation amplitude.

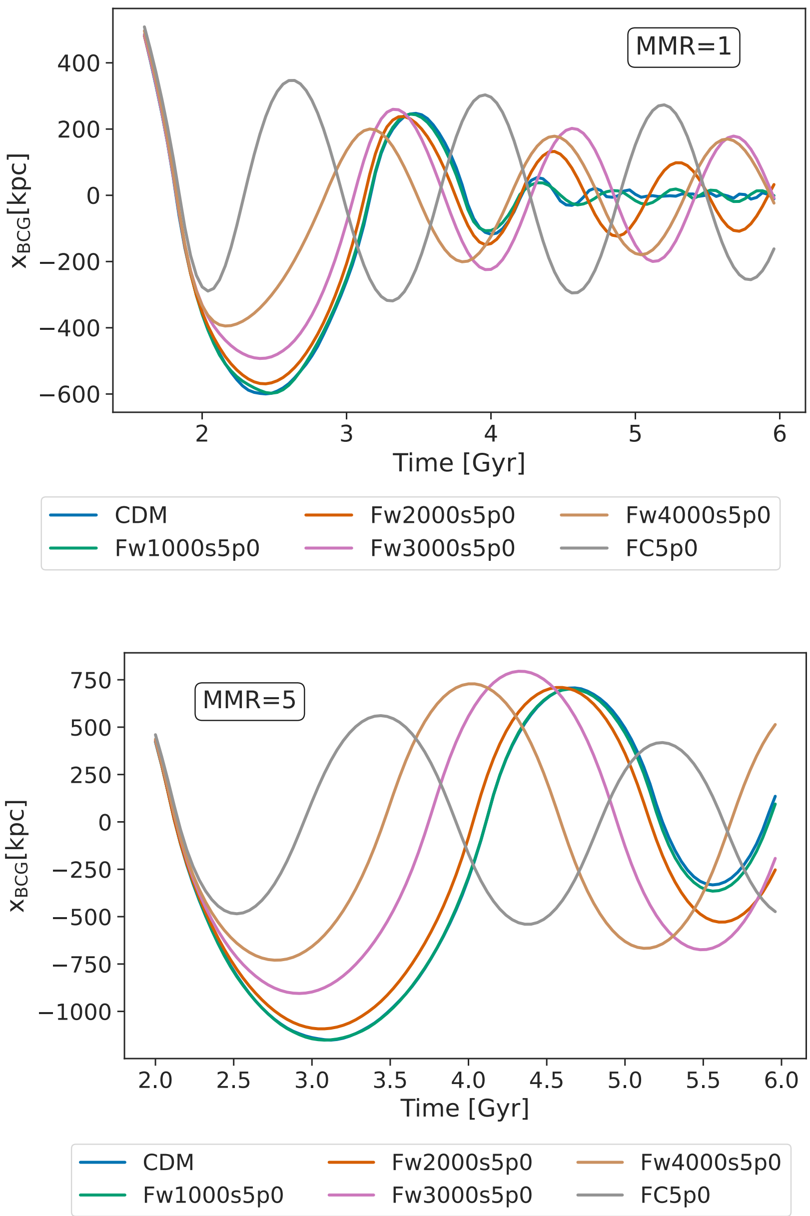

Figure 2.3: BCG position of the subhalo vs. time. The upper panel shows peak positions in the equal-mass merger, while the lower panel corresponds to the unequal-mass merger. For better visibility, we plot only the position of the BCG of the subhalo. Plot labels are described in **Tab. 2.3**.

2.3.3 Morphology

In **Fig. 2.4**, we show the physical density of DM within the slice $|z| < 100\,\text{kpc}$ projected on the merger plane.

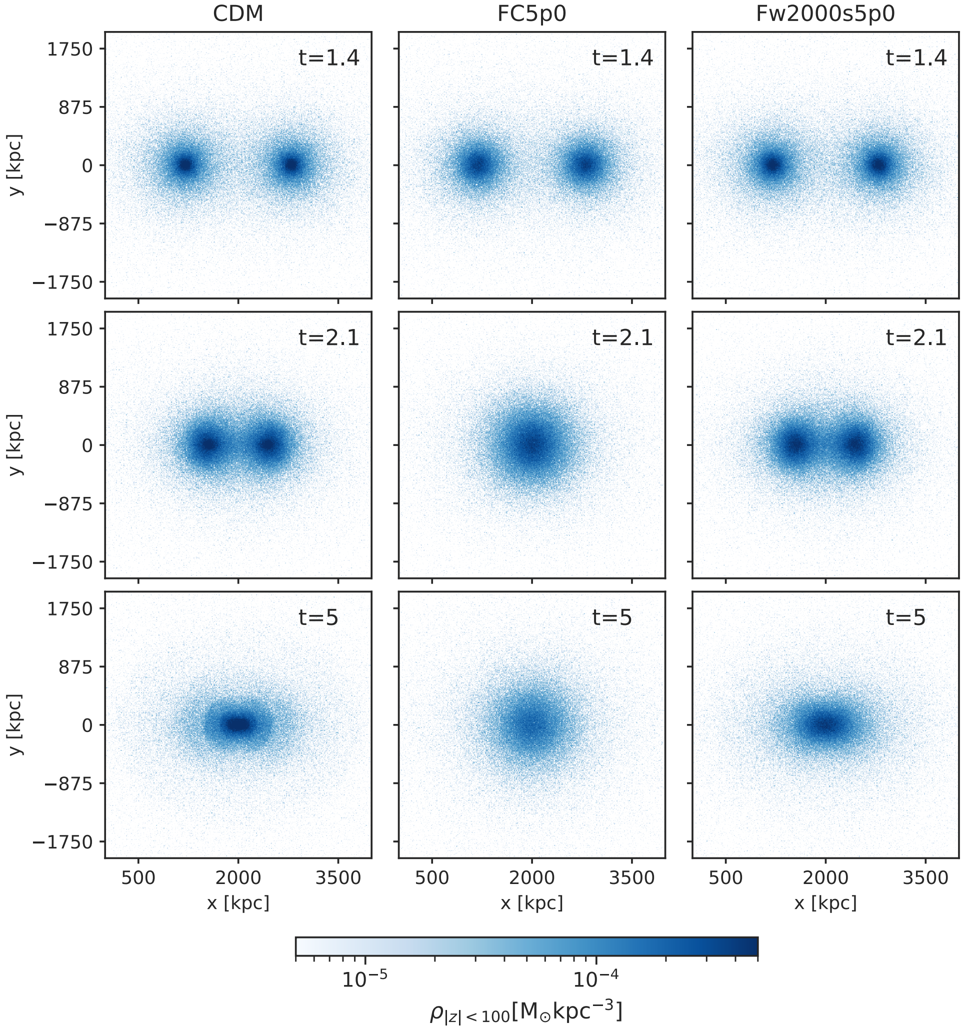

Figure 2.4: The density of DM haloes, accounting for the particles within $|z| < 100$ kpc. The first column corresponds to CDM simulations, while the second and the third columns correspond to simulations with the following momentum transfer cross-sections (σ_{0m}, w) : $(5, \infty), (5, 2000)$. The rows correspond to different times. The first row being before the pericentre passage, the second, just after the first pericentre passage and the third being at later stages. The time stamps in the images are in units of Gyr.

There are three columns, each correspond to a DM model and each row corresponds to a particular simulation time. First we look at time $t = 1.4$ Gyr, i.e. before the first pericentre passage. Both haloes in the constant σ_T simulation (column 2) have lower central densities than in the CDM (column 1) and velocity-dependent simulations (column 3). The second row shows results at a time $t = 2.1$ Gyr, which is just after the first pericentre passage. Owing to the large self-interaction strength, the haloes in the constant σ_T simulation have coalesced, while for CDM and velocity-dependent self-interactions the DM haloes pass through each other.

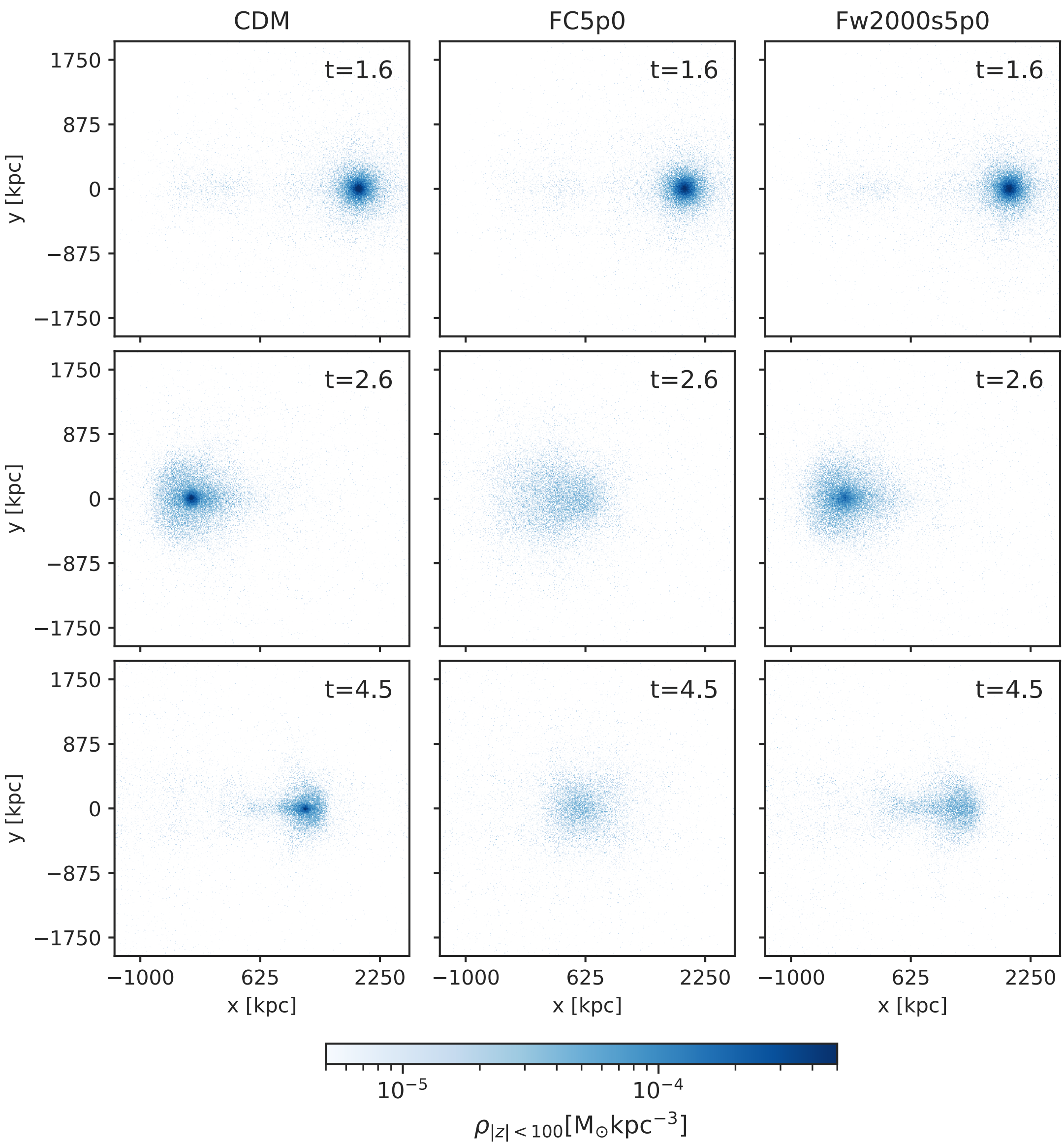

Figure 2.5: Plot similar to **Fig. 2.4**, but displaying only the subhalo of MMR:5 simulation.

At later stages, $t > 5$ Gyr, the merger remnant in the constant σ_T simulation has a lower central density. While for the velocity-dependent simulations, the effects of velocity-dependence slowly becomes relevant as the system slows down. Thus, this leads to more cored distribution at the centre of the merger remnant when compared to the one from CDM simulation. This feature essentially leads to the persistent BCG oscillations at late stages. In **Fig. 2.5** we have a similar plot displaying only the subhalo's projected density for MMR:5. Independent of the choice for the $\sigma_T(v)$, the subhaloes are observed to evaporate with time. With self-interactions, the evaporation is more pronounced. At $t = 4.5$ Gyr, the subhalo experiencing constant σ_T has its core dissolved significantly and comes to rest. For CDM, the core has remained relatively intact. Finally, in the velocity-dependent simulation, the core has dissolved. Although the merger remnant seems to be oscillating even at these stages. In addition, in the CDM simulation, we see shell-like features. These features are missing in the constant σ_T simulation, since the haloes have coalesced.

2.4 Central Density matched cross-section

In this section, we explore a more refined matching procedure based on simulations of isolated haloes. In this matching scheme, parameters $\{\sigma_{0m}, w\}$ are chosen such that different parameter combinations lead to similar central density evolution. We will refer to parameters matched according to this scheme as CD-matched. To avoid performing multiple simulations to find the matched parameter set, we make use of the self-similar nature of the gravothermal fluid equations of an isolated halo (Balberg et al. 2002b, Essig et al. 2019). This allows us to obtain the central density evolution without running a suite of simulations. In Balberg et al. (2002), they assume that the total cross-section is velocity independent. In order to illustrate the rescaling, consider two constant cross-section parameters $\sigma^A_{0m}, \sigma^B_{0m}$. Then, the central density evolution obeys the following scaling relation:

$$\rho_c(t^A) = \rho_c\left(t^B \times \frac{\sigma^B_{0m}}{\sigma^A_{0m}}\right), \tag{2.9}$$

where t^A, t^B correspond to the evolution time of the isolated haloes simulated with parameters $\sigma^A_{0m}, \sigma^B_{0m}$.

Velocity-dependent cross-sections contain two parameters, and it is not immediately clear how the central densities can be rescaled. D. Yang et al. (2022) propose an effective cross-section σ_{eff} to model the halo evolution. For a differential cross-section $\mathrm{d}\sigma/\mathrm{d}\cos\theta$, the effective cross-section is given by

$$\sigma_{\text{eff}} = \frac{1}{512(\sigma_{1\text{D}})^8}\int v^2\mathrm{d}v\,\mathrm{d}\cos\theta\, v^5\sin^2\theta\frac{\mathrm{d}\sigma}{\mathrm{d}\cos\theta}\exp\left(-\frac{v^2}{4\sigma^2_{1\text{D}}}\right). \tag{2.10}$$

In the expression given above, v is the relative velocity of DM particles, $\sigma_{1\text{D}}$ is the characteristic velocity dispersion of the halo. D. Yang et al. (2022) show that the evolution of central density in a simulation with the differential cross-section can be mimicked by a constant cross-section simulation with the same σ_{eff}. They also note that the equivalence holds well when the halo is in short-mean-free-path regime. In the long-mean-free-path regime, σ_{eff} does not capture the effects of self-scattering accurately. However, it provides a reasonable approximation to the halo evolution. Therefore, we extend the rescaling procedure given in (2.9) to any differential cross-section by using the corresponding effective cross-section σ_{eff}.

Integrating the angular part of (2.10), we get

$$\sigma_{\text{eff}} \propto \int v^2\mathrm{d}v v^5\sigma_{\text{V}}(v,w)\exp\left(-\frac{v^2}{4\sigma^2_{1\text{D}}}\right) \propto \sigma_{0m}f(w), \tag{2.11}$$

where,

$$\sigma_{\rm V} = \int \mathrm{d}\cos\theta \sin^2\theta \frac{\mathrm{d}\sigma}{\mathrm{d}\cos\theta}, \tag{2.12}$$

is the viscosity cross-section.

Thus, for a given w, $\sigma^A_{\rm eff}/\sigma^B_{\rm eff} = \sigma^A_{0m}/\sigma^B_{0m}$. In other words, rescaling by $\sigma_{\rm eff}$ is equivalent to rescaling by σ_{0m} for the same w. We verify this method by performing tests with some parameter combinations, see **App. 2.A**.

In order to find the value σ_{0m} given a w, such that the evolution of the central density matches that of a target simulation with parameter set, $Q = \{\sigma^Q_{0m}, w^Q\}$ we follow the procedure given below.

1. Simulate an isolated halo with the target parameter set. Find the evolution of the central density $\rho^Q_c(t^Q)$ from the simulation snapshots.

2. Simulate an isolated halo with the parameter set $A = \{\sigma^A_{0m}, w\}$, followed by the estimation of the evolution of central density $\rho^A_c(t^A)$ from the simulation data.

3. To obtain the evolution $\rho^B_c(t^B)$ corresponding to the parameter set $B = \{\sigma^B_{0m}, w\}$, rescale the time axis of the simulation A, i.e.,

$$\rho^B_c(t^B) = \rho^A_c\left(t^A \times \frac{\sigma^A_{0m}}{\sigma^B_{0m}}\right). \tag{2.13}$$

4. Repeat the previous step with different values of σ^B_{0m} until $\rho^B_c(t^B)$ matches $\rho^Q_c(t^Q)$.

Thus, we have obtained the CD-matched σ^B_{0m} for the given w. To make a guess for the value of σ^A_{0m} for one of our chosen values of w, we solve,

$$\sigma_{\rm eff}(\sigma^A_{0m}, w) = \sigma^Q_{\rm eff}. \tag{2.14}$$

To this end, we need a value for $\sigma_{\rm 1D}$. In D. Yang et al. (2022), they propose to use the velocity dispersion in the central region of the halo at the maximal core expansion stage for the characteristic dispersion $\sigma_{\rm 1D}$. Using semi-analytic modelling, Outmezguine et al. (2023) show that the 1D velocity dispersion is $0.64V_{\rm max}$ at the maximal core expansion phase. Using $V_{\rm max} \approx 1.65 r_s\sqrt{G\rho_0}$ for our NFW parameters, we find $\sigma_{\rm 1D} \approx 980\,\mathrm{km\,s^{-1}}$. On the other hand, we observe $\sigma_{\rm 1D} \approx 1000\,\mathrm{km\,s^{-1}}$ in our simulations. Thus, we find consistency between our simulations and the semi-analytic result.

We calculate the initial guess σ^A_{0m} for rare self-interactions and use the same for frequent self-interactions. For this calculation, we use the differential cross-section given in **section 2.2.3**. We choose the target set Q to correspond to the values quoted in Sagunski et al. (2021). They quoted a 95% upper limit on σ/m_χ of $0.35\,\mathrm{cm^2\,g^{-1}}$, assuming isotropy and velocity independence. Therefore, this value translates to $\sigma_{0m} = 0.175\,\mathrm{cm^2\,g^{-1}}$ for rare self-interactions (because $\sigma = 2\sigma_{\rm T}$). In other words, we choose the target set $Q = \{0.175\,\mathrm{cm^2\,g^{-1}}, \infty\}$. In **Fig. 2.6**, we show an example for the matching procedure in detail. The black band corresponds to the target central density of constant σ_T with $\sigma_{0m} = 0.175\,\mathrm{cm^2\,g^{-1}}$. The orange band corresponds to a simulation with $\{2.72\,\mathrm{cm^2\,g^{-1}}, 2000\,\mathrm{km\,s^{-1}}\}$. This value for σ_{0m} is our initial guess calculated using (2.14). After rescaling by trial and error, the desired value of σ_{0m} is found to be $1.2\,\mathrm{cm^2\,g^{-1}}$. This procedure can be extended to all chosen values of w and the obtained results are tabulated in **Tab. 2.4**. The inferred values of σ_{0m} at different values of w can then be used to calculate the corresponding viscosity cross-section σ_V. This is shown in **Fig. 2.7**.

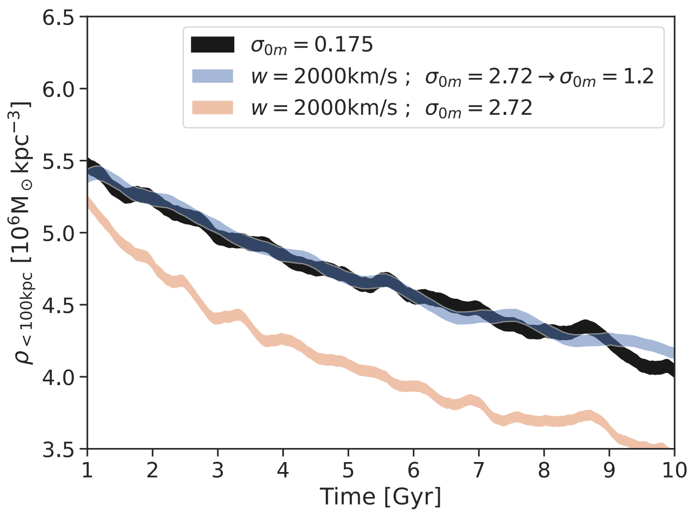

Figure 2.6: Evolution of central density of an isolated halo of virial mass $10^{15}\mathrm{M_\odot}$. There are three bands in the plot corresponing to, (i) simulation with rare self-interactions with constant σ_T of $\sigma_{0m} = 0.175$ (ii) simulation for $w = 2000\,\mathrm{km\,s^{-1}}$ with an initial guess for $\sigma_{0m} = 2.72\,\mathrm{cm^2\,g^{-1}}$ (iii) the same simulation as the earlier one, but rescaled to $\sigma_{0m} = 1.2\,\mathrm{cm^2\,g^{-1}}$. The width of the band corresponds to the uncertainty in the estimation of central density, and it is proportional to $1/\sqrt{N}$.

The orange triangles and blue stars represent the values of σ_V obtained using the inferred values of σ_{0m} from N-body simulations for rare and frequent self-interactions, respectively. Similarly, the solid line corresponds to the σ_V calculated from the values of σ_{0m} inferred by solving (2.14). The fact that the results obtained from σ_{eff} and N-body simulations are different can be attributed to the fact that the isolated halo is in the long-mean-free-path regime. This was already noted in D. Yang et al. (2022).

The evolution of an isolated halo has a feature that, as long as it is in the core expansion phase, at any given time the central density is monotonically decreasing with σ_{eff}. This implies that for a given value of w, and at a given time in the evolution of the halo, core-size is larger for larger values of σ_{0m}. Sagunski et al. (2021),Andrade et al. (2021),and Eckert et al. (2022) constrain σ_{0m} using the observed core-size in clusters. Hence, for every value of w, there is a value of σ_{0m} that produces core sizes, or central densities, similar to the current upper bound.

Increasing σ_{0m} any further would increase the core size to values larger than what is observed. Thus, this matching procedure can be used to extend the bounds from constant σ_T to different values of w.

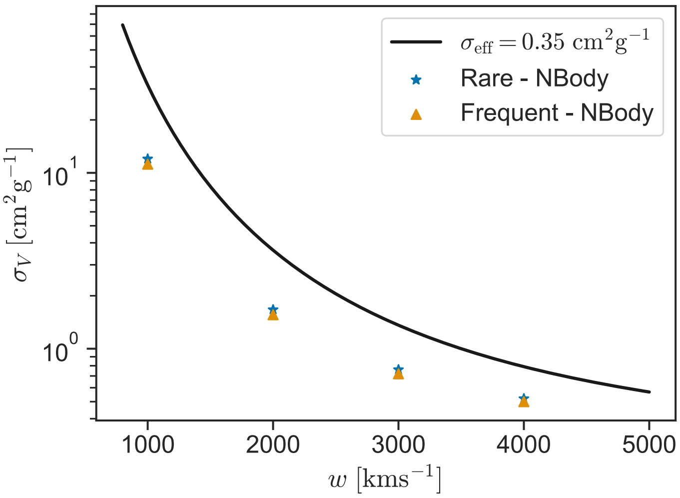

Figure 2.7: The plot contains viscosity cross-section evaluated at $v = 0$, for different values of w. At each w, the inferred value of σ_{0m} is used to compute σ_V. The triangles and stars represent σ_V calculated using the σ_{0m} inferred from N-body simulations for fSIDM and rSIDM, respectively. The solid line corresponds to σ_{0m} inferred by solving $\sigma_{\rm eff} = 0.35\,{\rm cm}^2\,{\rm g}^{-1}$.

When matched using $\sigma_{\rm eff}$ or central density evolution, we observe that the ratio between the σ_{0m}'s of rare and frequent is approximately 0.64 at every chosen values of w. This can be understood from the definition of $\sigma_{\rm eff}$. From (2.11), we have for any w, for rare self-interactions,

$$\sigma_{\rm eff} = C\sigma_{0m} \int {\rm d}\theta \sin^3\theta \int {\rm d}v v^7 \exp\left(\frac{-v^2}{4\sigma_{\rm 1D}^2}\right)\left(1 + \frac{v^2}{w^2}\right)^{-2} \tag{2.15}$$

$$= C\frac{4}{3}\sigma_{0m} f(w). \tag{2.16}$$

Here, $C = 1/(512\sigma_{\rm 1D}^8)$. Now from (2.6), for rare self-interactions we have $\sigma_{\rm T} = \sigma_{0m} g(w, v)$, which implies that

$$\sigma_{\rm eff} = \frac{4}{3}\sigma_{\rm T} C f/g. \tag{2.17}$$

For frequent self-interactions, we consider a differential cross-section of the form given in (2.8) with the function $\Theta(\theta)$ having support only for values of θ close to 0. A simple choice for $\Theta(\theta)$ is a step-function that is non-zero in the interval $[0, \epsilon]$, where ϵ is some small number. Therefore, $\sigma_{\rm eff}$ is given as

$$\sigma_{\text{eff}} = CN\sigma_{0m} \int d\theta \sin^3\theta\Theta(\theta) \int dv v^7 \exp\left(\frac{-v^2}{4\sigma_{1D}^2}\right) g(w, v) \tag{2.18}$$

$$\approx CN\sigma_{0m} \int d\theta\theta^3\Theta(\theta) f(w) = CN\sigma_{0m} f(w)\epsilon^4/4, \tag{2.19}$$

where in the second equality we have Taylor-expanded and retained only the leading order in θ in the angular integrand. Similarly, for the momentum transfer cross-section we have

$$\sigma_{\text{T}} = N\sigma_{0m} g(w, v) \int d\theta \sin\theta(1 - |\cos\theta|)\Theta(\theta) \tag{2.20}$$

$$\approx N\sigma_{0m} g(w, v)\epsilon^4/8. \tag{2.21}$$

Thus for frequent self-interactions, we have

$$\sigma_{\text{eff}} = 2\sigma_{\text{T}} Cf/g. \tag{2.22}$$

Now for matching with σ_{eff} or the central density we require $\sigma_{\text{eff}}(\text{Rare}) = \sigma_{\text{eff}}(\text{Freq.})$. Upon using (2.17) and (2.22), this requirement leads to the matching condition

$$\sigma_{\text{T}}(\text{Freq.}) = (2/3)\sigma_{\text{T}}(\text{Rare}) \implies \sigma_{0m}(\text{Freq.}) = (2/3)\sigma_{0m}(\text{Rare}), \tag{2.23}$$

and this can be seen in the below given table (**Tab. 2.4**).

2.4.1 Central density matched simulations – qualitative features

In this subsection, we look at the qualitative differences in mergers when parameters are chosen according to the central density matching procedure. Again, as in **section 2.3**, we only simulate frequent self-interactions. In **section 2.3**, we investigated the effects arising from changing the value of w. To ensure that the effects of self-interaction are not negligible for $w = 1000\,\text{km}\,\text{s}^{-1}$, we used a large value for σ_{0m} of $5.0\,\text{cm}^2\,\text{g}^{-1}$. On the other hand, in this section the cross-section parameters are CD-matched for which we choose the target set to be $Q = \{1.0\,\text{cm}^2\,\text{g}^{-1}, \infty\}$. The matched parameters are given in **Tab. 2.5**. We have chosen a value for σ_{0m} such that the effects of self-interaction are observable, but not as large as the previous value $5.0\,\text{cm}^2\,\text{g}^{-1}$.

For brevity, we show only the BCG oscillations in **Fig. 2.8**. We see that the BCG oscillations of velocity-dependent simulations all have similar amplitudes at early stages. Only at a later stages they start to deviate. This similarity stems from the fact that the parameters are CD-matched. Similar to what was explained in **section 2.3.2**, at early times the DM particles have a large relative velocity. As a result, most of the velocity-dependent cross-sections have a small effective self-interaction strength. At later stages, the system slows down and $v \lesssim w$ and the effective self-interaction strength increases. In addition, the internal evolution around a DM peak is similar for all the cross-section parameters chosen, since they are CD-matched. See **section 2.C** for the evolution of the central density of the main halo.

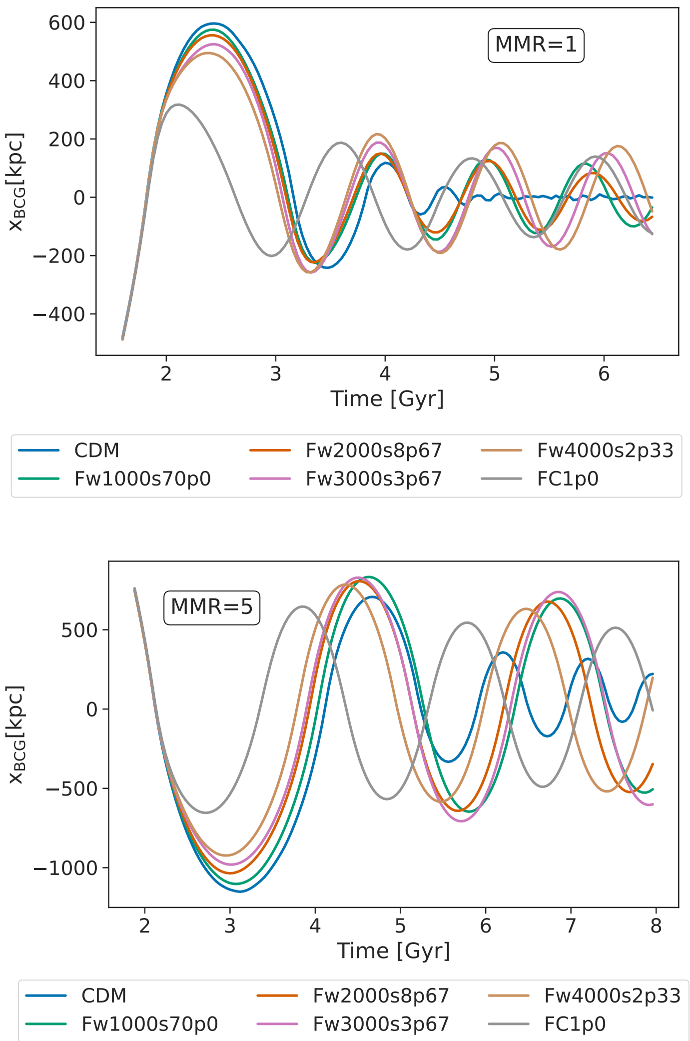

Figure 2.8: BCG positions of the subhalo against time. The upper panel corresponds to equal mass merger, while the lower one corresponds to unequal mass merger.

w	Frequent		Rare	
	σ_{0m}	Label	σ_{0m}	Label
$[\mathrm{km\,s^{-1}}]$	$[\mathrm{cm^2\,g^{-1}}]$		$[\mathrm{cm^2\,g^{-1}}]$	
1000	5.6	Fw1000s5p6	9.0	Rw1000s9p0
2000	0.78	Fw2000s0p78	1.25	Rw2000s1p25
3000	0.36	Fw3000s0p36	0.57	Rw3000s0p57
4000	0.25	Fw4000s0p25	0.39	Rw4000s0p39
∞	0.11	FC0p11	0.175	RC0p175

Table 2.4: This table contains the conservative upper bound on σ_{0m} for different values of w given in the first column. The second column contains σ_{0m} the value for frequent self-interactions, and the third for rare self-interactions.

w $[\mathrm{km\,s^{-1}}]$	σ $[\mathrm{cm^2\,g^{-1}}]$	Label
1000	70.0	Fw1000s70p0
2000	8.67	Fw2000s8p67
3000	3.67	Fw3000s3p67
4000	2.33	Fw4000s2p33
∞	1.0	FC1p0

Table 2.5: This table contains labels and cross-section parameters matched to constant cross-section, $\sigma_{0m} = 1.0\,\mathrm{cm^2\,g^{-1}}$ of frequent self-interactions using central density matching scheme.

2.4.2 Central density matched upper bound simulations

In **section 2.4**, the conservative upper bounds were obtained using the central density matching scheme. Values are tabulated in **Tab. 2.4**. We run merger simulations for this set of parameters and estimate the offsets $d_{\mathrm{DM-BCG}}$. For velocity-independent cross-sections up to $0.5\,\mathrm{cm^2\,g^{-1}}$, Fischer et al. (2021) found that the DM-BCG and DM-Galaxy offsets increase with increasing values of σ_{0m}. By running merger simulations at the upper bound values of the cross-section parameters, we estimate the order of magnitude of the largest possible offsets allowed by current bounds.

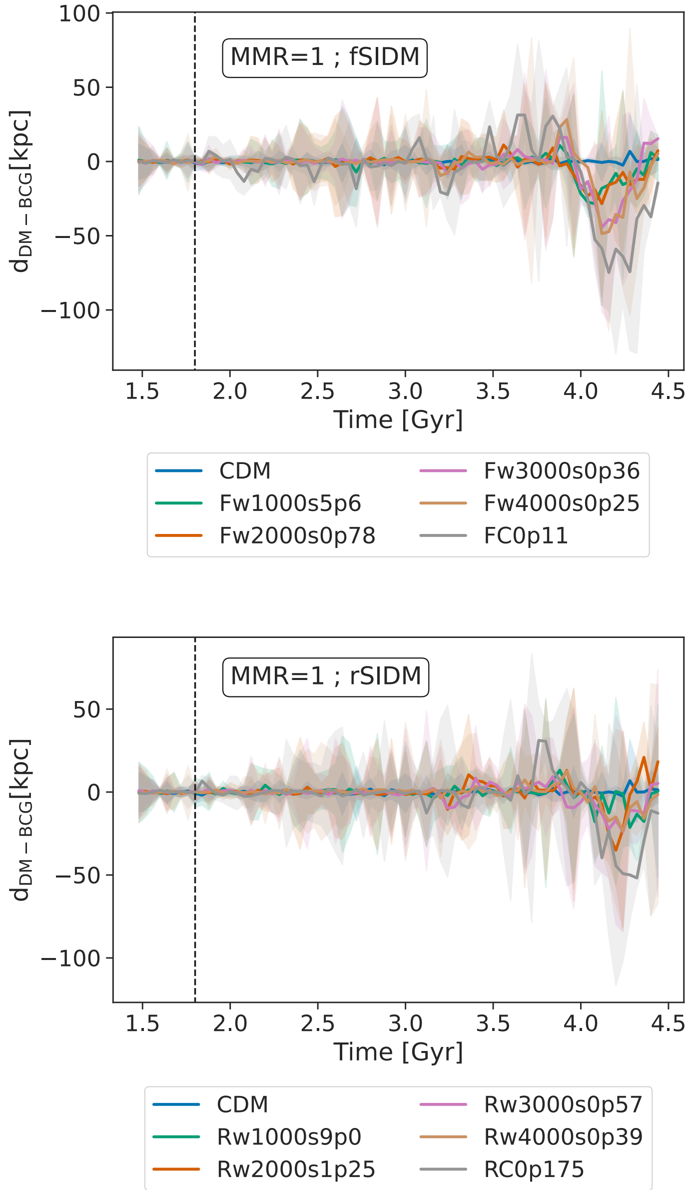

Figure 2.9: DM – BCG offsets in the equal-mass merger. Upper panel corresponds to fSIDM, while bottom panel to rSIDM. The plot labels are described in **Tab. 2.4**. The vertical dashed lines correspond to the time of the first pericentre passage.

In **Fig. 2.9**, we show the DM-BCG offset at the first pericentre passage for the equal mass merger. The offset is $\mathcal{O}(1)$kpc, while the offsets after the third pericentre passage ($t \sim 4$ billion years) start increasing and is seen to be $\mathcal{O}(10)$kpc. The effective self-interaction strength is not large enough to produce an observable offset at the first pericentre. Hence, it might be difficult to find such an offset in real observations. We do not show the offsets for unequal mass merger because, the offsets just after the first pericentre are smaller than the ones of equal mass merger. In addition, at later stages due to the evaporation of halo, we do not have reliable peak positions. We can also see from **Fig. 2.9** that the offsets produced by fSIDM are larger than that of rSIDM, and this is due to the fact that mergers are sensitive to the angular dependence.

2.5 Conclusions

We first discuss the assumptions made in the paper before we conclude. The first assumption that we make is that we use idealized initial conditions. Yet, it is informative to study them to find the appropriate features to look out for in more realistic simulations and observations. One example is the amplitude of BCG oscillation at late stages, which is seen to depend on the velocity-dependent cross-section parameters. Therefore, it is instructive to simulate cosmological boxes with velocity-dependent cross-section at higher resolution in order to estimate the distribution of DM-BCG offsets. Later, this could be compared to observations (e.g. Lauer et al. 2014, Cross et al. 2023). For example, Harvey et al. (2019) studied the DM-BCG offsets in the BAHAMAS–SIDM suite of cosmological simulations and placed constraints on σ/m_χ assuming velocity-independent isotropic SIDM.

In addition, we have modelled the BCG and galaxies as collision-less point particles. A more realistic treatment of BCG's and galaxies is necessary for better comparison with observations. Furthermore, we neglect the effect of galaxies having their own DM halo (Kummer et al. 2018). In reality, approximately 10% of the mass of clusters is made up by the intracluster medium (ICM), which is not included in our simulations. Merger studies that include the ICM, such as A. Robertson et al. (2017), find that the DM-galaxy offset is not significantly affected by the presence of the ICM. Fischer et al. (2023) also finds similar results. Therefore, we argue that the absence of an ICM component does not significantly affect our conclusions. We leave the study of these systems with hydrodynamic simulations to a future study.

As mentioned in **section 2.2.3**, we have assumed that the angular and velocity dependence of the differential cross-sections can be separated into two functions. This assumption has to be dropped when dealing with realistic SIDM models (J. L. Feng et al. 2009, Tulin et al. 2013a). There are other SIDM models leading to different effects that are not included in our studies. For example, in addition to elastic scattering, inelastic scattering could be included (O'Neil et al. 2022). We leave the study of such models to future work.

On the observation side, all observed DM-BCG offsets are inferred to be just after pericentre passage and have uncertainties that make them consistent with zero (Bradač et al. 2008, Dawson et al. 2012, Dawson 2013, Jee et al. 2014, Jee et al. 2015). Similarly, estimating DM-galaxy offsets are difficult due to shot noise arising from the smaller galaxy count. In our simulations we had 10^6 galaxy particles, but in reality we observe at most $\sim 10^3$ of them. On the other hand, Lauer et al. (2014) find a median offset of $\sim 10\,\mathrm{kpc}$, with the offset measured between BCG and cluster centre, the latter being identified by X-ray observations. Their sample comprised 433 BCGs that are located in Abell galaxy clusters. The DM-BCG offset distribution could be compared to predictions of cosmological simulations. Overall, the situation with observations is expected to improve with forthcoming surveys, such as *SuperBIT* (Romualdez et al. 2016) and *Euclid* (Laureijs et al. 2011).

We have simulated idealized, isolated haloes and galaxy cluster mergers with equal and unequal merger mass ratios with velocity-dependent, frequent and rare self-interactions. Mergers are interesting astrophysical probes since the system is sensitive to self-interaction cross-sections with both angular and velocity dependencies. Therefore, we focused on understanding the qualitative effects that arise from velocity dependence in mergers. On the quantitative side, we also investigate the maximum offsets that can be observed given the current bounds on σ/m_χ.

- Independent of the matching procedure used in the paper, the effects of velocity-dependent cross-sections can be observed on galaxy cluster mergers by comparing the early time and late time oscillations of BCG. In particular, the degeneracy in the cross-section parameters when studying the evolution of central density in isolated haloes is broken when studying mergers. This is due to the fact that the relative velocities of the merging clusters change with time.

- The evolution of central densities of isolated haloes are similar between rare and frequent self-interaction, when the momentum transfer cross-section $\sigma_\mathrm{T}(v)$ of fSIDM is chosen to be $2/3\sigma_\mathrm{T}(v)$ of rSIDM. The factor 2/3 follows from matching the angular dependence of fSIDM and rSIDM with viscosity cross-section, as seen in **Fig. 2.7**.

- We extend the existing upper bounds on the constant cross-section σ_{0m} to the parameter space $\{\sigma_{0m}, w\}$ of velocity-dependent, rare and frequent self-interactions.

- In the equal-mass merger simulations with upper-bound cross-section parameters, we find that the offsets after the first pericentre is approximately $\mathcal{O}(1)$kpc. In particular, the offsets are the largest in the constant cross-section simulation. As the system evolves further, offsets grow. After the third pericentre passage, due to the oscillations of BCG, and the galactic component the offsets are $\mathcal{O}(10)$kpc. Thus, mergers in their late stages are interesting to test and constrain SIDM.

In conclusion, we have studied the qualitative effects of velocity-dependent SIDM cross-sections in galaxy cluster mergers. Our models do not have the realism required for a direct comparison with astronomical data, owing to the neglection of baryonic effects. However, they offer insights into the physical processes that govern the phenomenology of SIDM. More realistic predictions can be obtained by performing full hydrodynamical simulations that include stars, cooling and feedback effects. The significantly larger complexity of such models with additional degrees of freedom render the interpretation much harder. Clearly, this is an avenue for future work.

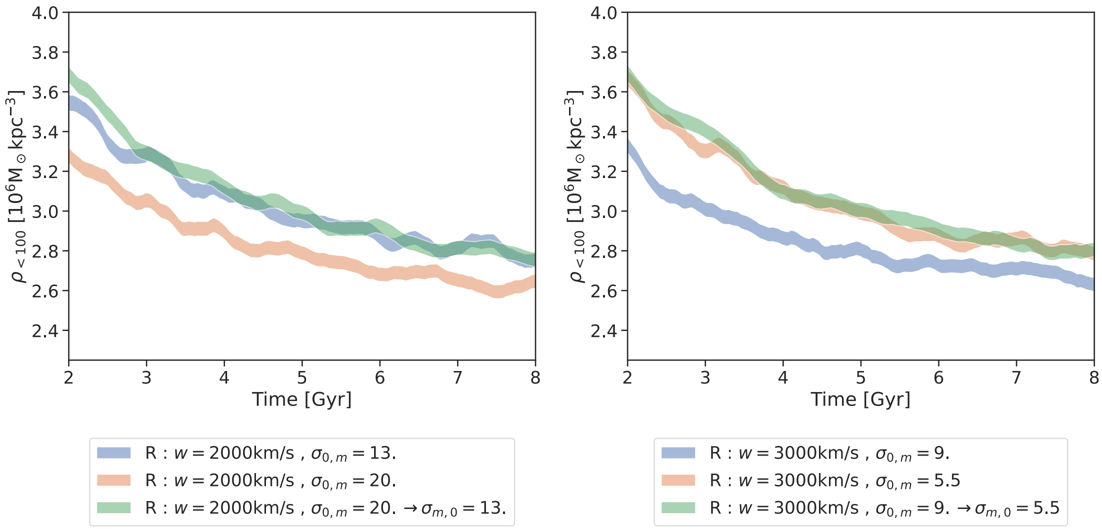

Figure 2.A1: Evolution of central density for two values of w, 2000 km s^{-1} and 3000 km s^{-1} in the top and bottom panel, respectively.

Appendix

2.A Testing rescaling

We test the rescaling by σ_{0m} for a given w with rare self-interactions. **Fig. 2.A1** shows the evolution of central density of an isolated halo for two values of w – 2000 km s^{-1} and 3000 km s^{-1} – in the left and right panel, respectively. For example, in the left panel, after rescaling t of $\sigma_{0m} = 20\,\mathrm{cm^2\,g^{-1}}$ simulation by a factor 20/13, the evolution is similar to the simulation with $\sigma_{0m} = 13\,\mathrm{cm^2\,g^{-1}}$.

2.B Validating lower resolution simulations

In this section, we compare the peak positions of DM, galaxy and BCG components between low resolution and high resolution simulations. The low- and the high-resolution simulation use the NFW parameters given in **Tab. 2.1** for generating the haloes. The only difference being that the DM and galaxy particles in the high-resolution simulation have a resolution of 10^7 particles instead of 10^6 particles. Both of them also use the same initial conditions as given in **Tab. 2.2**. The DM component is simulated with and without self-interactions. For the SIDM case, we simulate with frequent self-interactions with a constant σ_T of $0.5\,\mathrm{cm^2\,g^{-1}}$. We observe that the peak positions evolve almost identically independent of the resolution up until 5 billion years. See **Fig. 2.B1** and **Fig. 2.B2**.

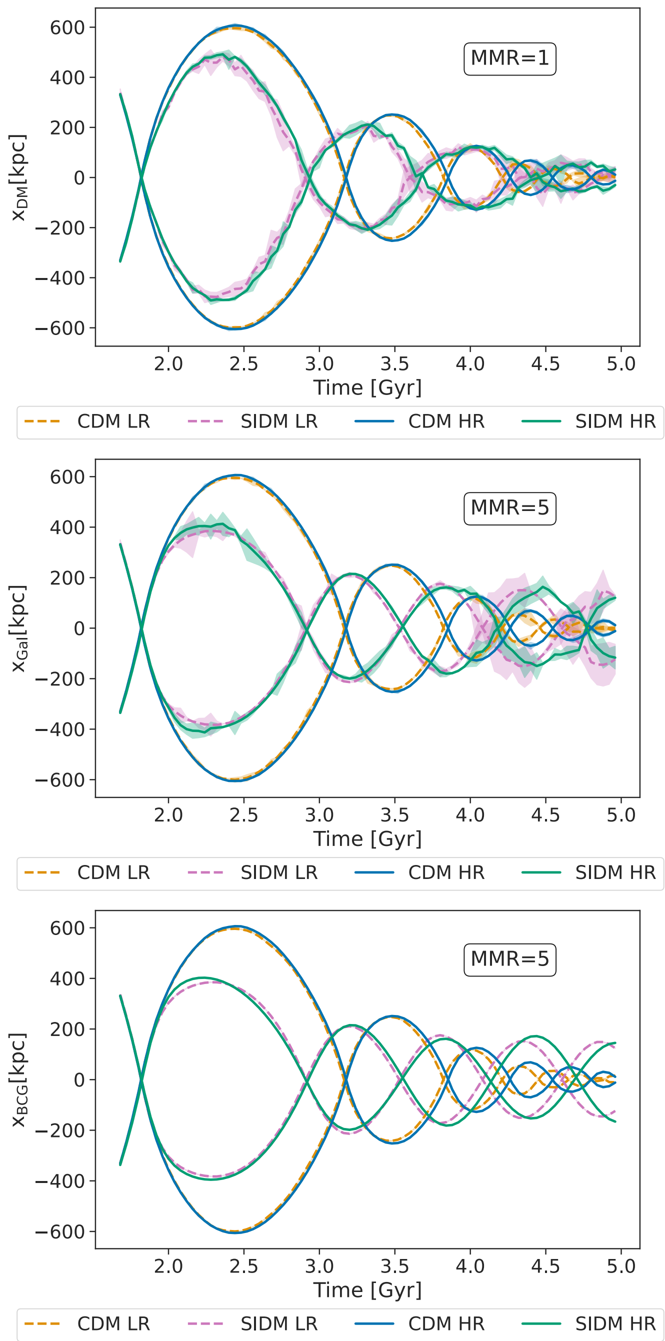

Figure 2.B1: Comparison of peaks positions of different components between low and high resolutions for both CDM and SIDM simulations in the equal mass merger. Top, middle and bottom panels correspond DM, galaxy and BCG components. The dashed lines correspond to low resolution and solid lines correspond to high resolution. The SIDM case corresponds to the frequent self-interactions with $\sigma_{0m} = 0.5\,\mathrm{m^2\,g^{-1}}$.

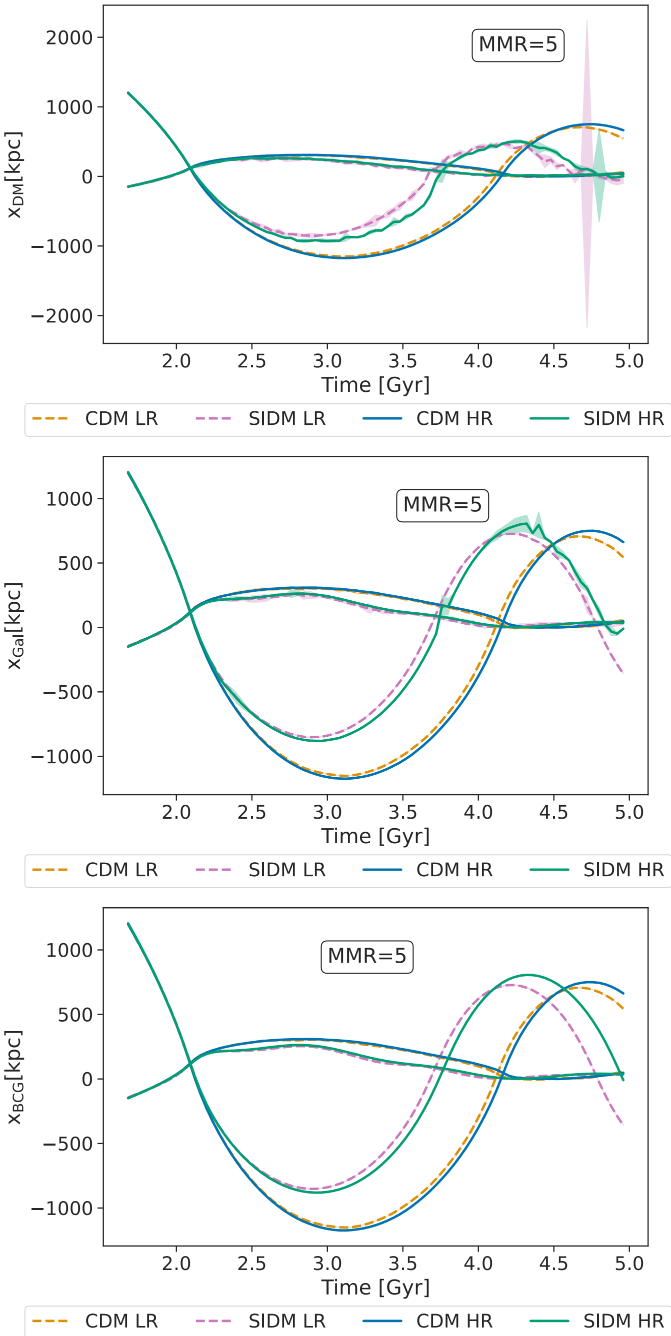

Figure 2.B2: Comparison of peaks positions of different components between low and high resolutions for CDM and SIDM simulations in the unequal mass merger. Top, middle and bottom panels correspond DM, galaxy and BCG components. The dashed lines correspond to low resolution and solid lines correspond to high resolution. The SIDM case corresponds to the frequent self-interactions with $\sigma_{0m} = 0.5\,\mathrm{m^2\,g^{-1}}$.

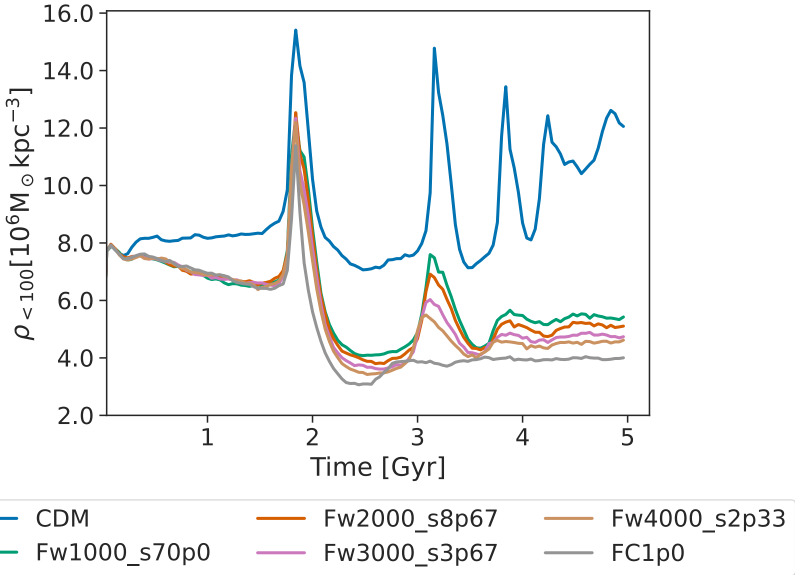

Figure 2.C1: Evolution of the central density measured within 100 kpc around the DM peak of main halo. The parameters are CD-matched and the labels are explained in **Tab. 2.5**.

2.C Central density evolution in Merger

In **Fig. 2.C1**, we show the evolution of the central density around the DM peak of the main halo in the equal mass merger. The curves correspond to simulations where the cross-section parameters are CD-matched. Similarly, in **Fig. 2.C2** we show the central densities for cases when the cross-section parameters have the same σ_{0m}, but with varying w.

2.D Central velocity dispersion evolution in Merger

The relative velocity dispersion around the DM peak within 100 kpc in the equal mass merger is shown as a function of time in **Fig. 2.D1** and **Fig. 2.D2**. The earlier figure corresponds to simulations with cross-section parameters that are CD-matched, while the latter figure corresponds to cross-section parameters with fixed σ_{0m} and varying w. The relative velocity dispersion is calculated from the 1D velocity dispersion, i.e. $\sigma_{\mathrm{rel}} = \sqrt{2}\sigma_{1D}$.

2.E Momentum transfer cross-section of CD-matched parameters

Plots similar to **Fig. 2.1** but with CD-matched parameters are provided. **Fig. 2.E1** and **Fig. 2.E2** correspond to the parameters in **Tab. 2.5** and **Tab. 2.4**, respectively.

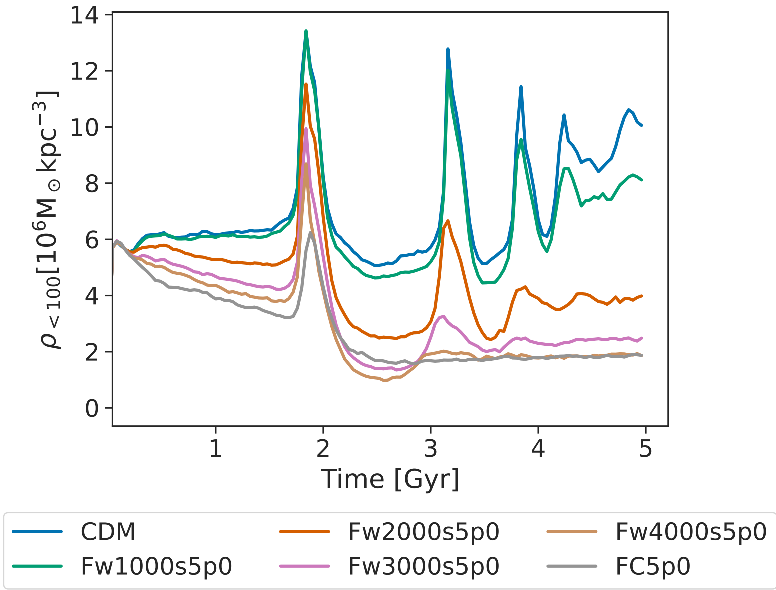

Figure 2.C2: Evolution of the central density measured within 100 kpc, around the DM peak of main halo in the equal mass merger. The parameters have the same value of $\sigma_{0m} = 5\,\mathrm{cm^2\,g^{-1}}$, but with varying values of w. The labels are explained in **Tab. 2.3**.

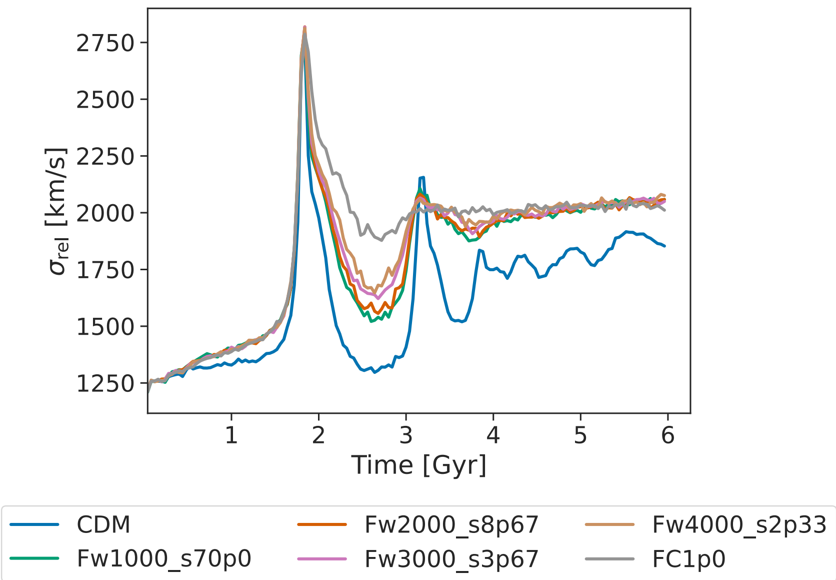

Figure 2.D1: Evolution of the central relative velocity dispersion measured within 100 kpc around the DM peak of main halo. The parameters are CD-matched and the labels are explained in **Tab. 2.5**.

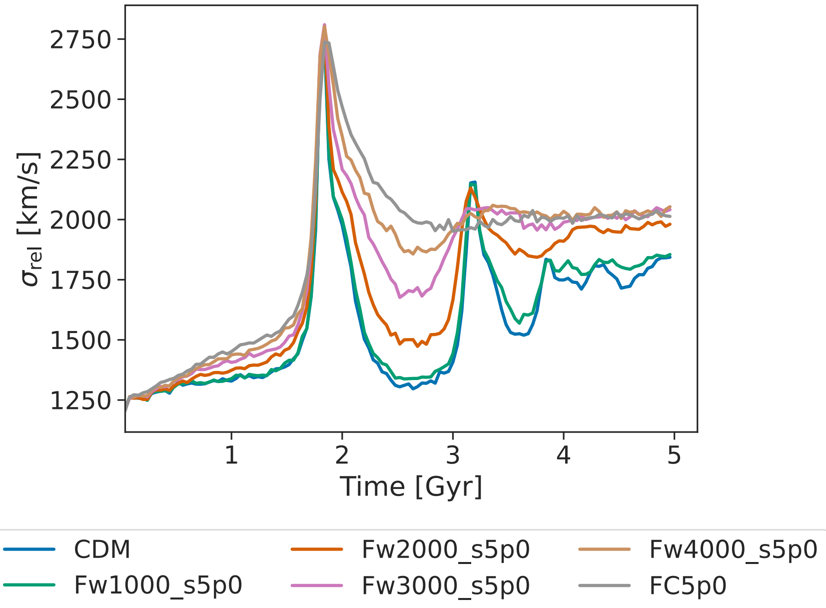

Figure 2.D2: Evolution of the central relative velocity dispersion within 100 kpc around the DM peak of the main halo. The parameters have the same value of $\sigma_{0m} = 5\,\mathrm{cm}^2\,\mathrm{g}^{-1}$, but with varying values of w. The labels are explained in **Tab. 2.3**.

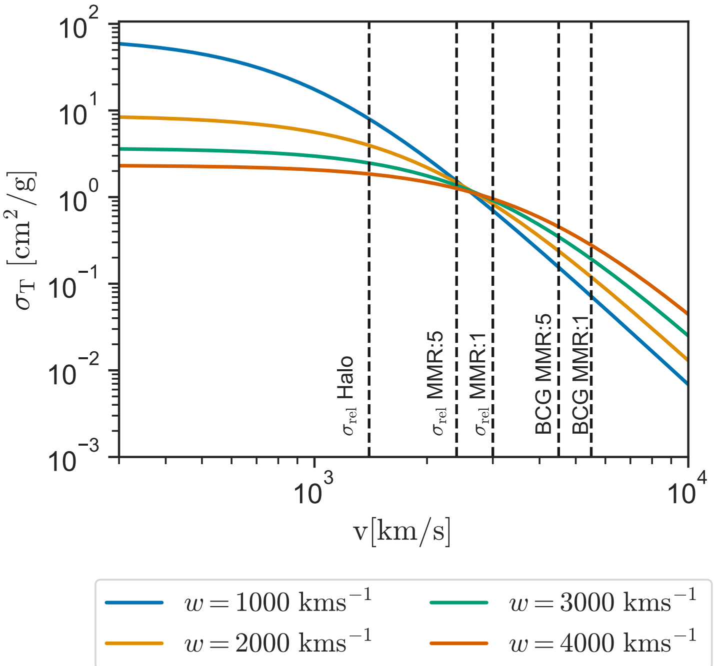

Figure 2.E1: Momentum transfer cross-section as a function of velocity for the parameters given in **Tab. 2.5**. The vertical dashed lines are explained in the captions of **Fig. 2.1**.

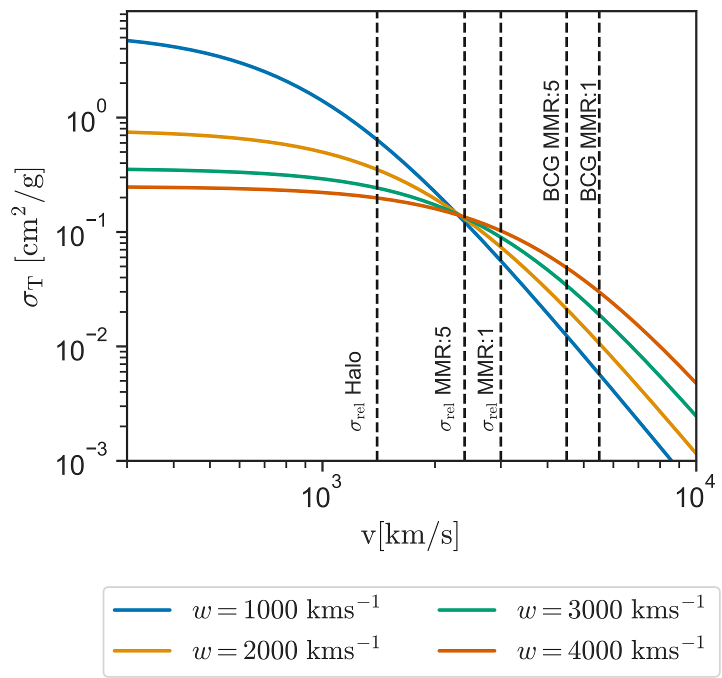

Figure 2.E2: Momentum transfer cross-section as a function of velocity for the parameters given in **Tab. 2.4**.The vertical dashed lines are explained in the captions of **Fig. 2.1**.

3 Accretion of self-interacting dark matter onto supermassive black holes

This chapter presents work as published in Sabarish et al. (2025).

3.1 Abstract

Dark matter (DM) spikes around supermassive black holes (SMBHs) may lead to interesting physical effects such as enhanced DM annihilation signals or dynamical friction within binary systems, shortening the merger time and possibly addressing the 'final parsec problem'. They can also be promising places to study the collisionality of DM because their velocity dispersion is higher than in DM halos allowing us to probe a different velocity regime. We aim to understand the evolution of isolated DM spikes for collisional DM and compute the black hole (BH) accretion rate as a function of the self-interaction cross-section. We have performed the first N-body simulations of self-interacting dark matter (SIDM) spikes around supermassive black holes (SMBH) and studied the evolution of the spike with an isolated BH starting from profiles similar to the ones that have been shown to be stable in analytical calculations. We find that the analytical profiles for SIDM spikes remain stable over the time-scales of hundreds of years that we have covered with our simulations. In the long-mean-free-path (LMFP) regime, the accretion rate onto the BHs grows linearly with the cross-section and flattens when we move towards the short-mean-free-path (SMFP) regime. In both regimes, our simulations match analytic expectations, which are based on the heat conduction description of SIDM. A simple model for the accretion rate allows us to calibrate the heat conduction in the gravothermal fluid prescription of SIDM. Using this prescription, we determine the maximum allowed accretion rate which occurs when $r_{\mathrm{ISCO}}\rho(r_{\mathrm{ISCO}})\sigma_m \sim 1$, where σ_m is the self-interaction cross-section and r_{ISCO} the radius of the innermost stable orbit. Our calibrated DM accretion rates could be used for statistical analysis of SMBH growth and incorporated into subgrid models to study BH growth in cosmological simulations.

3.2 Introduction

Self-interacting dark matter (SIDM) models are a class of models where dark matter (DM) can scatter off each other non-gravitationally (D. N. Spergel et al. 2000). SIDM has been invoked to solve potential small-scale problems of ΛCDM cosmology (Bullock et al. 2017). The most robust constraints on the self-interacting cross-section come from observations of galaxy clusters. In particular, by measuring the central density profiles of galaxy clusters (e.g. Andrade et al. 2021, Sagunski et al. 2021), and merging clusters such as the bullet cluster (Markevitch et al. 2004, Randall et al. 2008).

The effects of SIDM on astrophysical systems have been studied widely using N-body simulations of systems ranging from isolated dwarf galaxies (e.g. D. Yang et al. 2022) over merging galaxy clusters (e.g. S. Y. Kim et al. 2017, Fischer et al. 2022b, Sabarish et al. 2024, Arido et al. 2025) to cosmological simulations (Correa et al. 2022, Fischer et al. 2022a, Ragagnin et al. 2024, Despali et al. 2025). In addition, semi-analytic models exist to understand the evolution of SIDM halos (e.g. Balberg et al. 2002b, Jiang et al. 2023) and are powerful tools to constrain SIDM models (e.g. S. Yang et al. 2023b).

On even smaller scales, it is expected that we find dense DM distributions around black holes (BH) (Gondolo et al. 1999, Alachkar et al. 2023, Chan et al. 2024). The density distribution has a power-law profile $\rho(r) \propto r^{-\gamma}$, and is dubbed a DM spike. In the case of cold dark matter (CDM) it was shown theoretically that an adiabatic contraction of the DM halo that hosts the BH could lead to the formation of a DM spike (Gondolo et al. 1999, Sadeghian et al. 2013). For CDM, the spike index can be estimated from the initial CDM profile in which the BH is found. The resulting index is $\gamma = (9 - 2\delta)/(4 - \delta)$, where δ is the index of the initial density profile in the inner regions (Gondolo et al. 1999), that is $\rho \propto r^{-\delta}$. If the initial DM density follows a Navarro-Frenk-White (NFW) (Navarro et al. 1996) profile, a spike index of $\gamma = 7/3$ is obtained using $\delta = 1$. Therefore, such DM spikes are expected to be found around supermassive black holes (SMBH) since they are typically found inside a galactic halo. More recently, it was suggested that DM forms shallower mounds ($\gamma \approx 1$) instead of denser spikes due to different assumptions regarding the formation scenario Bertone et al. (2024). Specifically, they consider the formation and growth of a BH following the evolution of a supermassive star positioned at the centre of a DM halo.

DM spikes are not only expected around SMBHs, but also around intermediate mass BHs (IMBH) (Zhao et al. 2005). Studies of such systems using N-body simulations have been conducted before (e.g. Kavanagh et al. 2020, Kavanagh et al. 2024, Mukherjee et al. 2024). These authors set up the DM spike in equilibrium, and they study the effects of the spike profile on inspiralling secondary BHs. In particular, they find that the effect of dynamical friction (e.g. Binney et al. 2008) to play a significant role in speeding up the BH merger. Similarly, semi-analytic studies have also shown that dynamical friction can have an impact on the evolution of the binary by making the orbits less eccentric over time (e.g. Becker et al. 2022).

Non-negligible DM self-interactions will influence the dynamics within a DM spike and lead to some differences with respect to the collisionless case (e.g. Alonso-Álvarez et al. 2024, Fischer et al. 2024c, M.-C. Chen et al. 2025). Assuming velocity-isotropy and spatial-isotropy, Shapiro et al. (2014) solve the gravothermal fluid equations to find a static solution for an SIDM spike profile. It was shown that for self-interaction cross-sections with a velocity dependence that scales as $\sigma(v) \propto v^{-a}$, a stable spike profile exists with a spike index $\gamma = (3 + a)/4$. The steady-state solutions for SIDM have the same power-law index with and without relativistic corrections. To date, such an SIDM system has been studied in the fluid approximation but not yet with N-body simulations Shapiro (2018).

Observationally, DM spikes are interesting for various reasons. In 2021, NANOGrav (Agazie et al. 2023) detected a gravitational wave (GW) signal in the nHz-frequency regime using Pulsar Timing Array (PTA) data. The leading candidate for the production mechanism for this signal is the merger of SMBHs. It was pointed out that the observations made by PTAs are slightly different from the predictions that arise from the simplest model of a binary SMBH merger (Ellis et al. 2024). While not statistically significant at this point, it is still interesting to speculate about possible mechanisms that could lead to such a deviation. There are two possible sources: Either the environment of SMBHs, for example DM spikes, may have an effect on the merging process leading to a slightly different spectrum of GWs, or the signal could arise from some other, unrelated, beyond the standard model (BSM) physics. See Burke-Spolaor et al. (2019), Afzal et al. (2023), Ellis et al. (2024) for an overview of different models.

Finally, DM could accelerate SMBH mergers solving the final parsec problem as shown in Dosopoulou et al. (2017), Kavanagh et al. (2020), Alonso-Álvarez et al. (2024).

Observations of SMBHs with masses $\gtrsim 10^9\,\mathrm{M}_\odot$ at high redshifts are yet to be explained within the framework of ΛCDM cosmology (Inayoshi et al. 2020). For such objects to exist, a very massive seed is needed, and various mechanisms have been proposed for the formation of such seeds. One such mechanism is based on the gravothermally collapsing nature of SIDM halos (Jiang et al. 2025, Shen et al. 2025). In a similar spirit, W.-X. Feng et al. (2021), W.-X. Feng et al. (2022) argue that self-interactions can lead to the formation of dense, collapsing cores, which can eventually undergo a gravitational instability leading to the formation of such seeds.

In this paper, we investigate the spike profile as well as the accretion rate of the central SMBH dressed in a DM spike for varying self-interaction cross-sections. To this end, we perform N-body simulations. In this work we study velocity-independent self-scatterings and neglect the effects of gas and stars, i.e. we concentrate on the behaviour of DM only.

The structure of the paper is as follows: In **section 3.3**, we briefly introduce DM spikes and introduce equations that give an effective analytic description of these systems. Then, in Sect. 3.4, we describe the setup of our simulations. In Sect. 3.5 and Sect. 3.6 we present the results of our study of the accretion rates in DM spikes. Finally, in Sect. 3.7, we discuss our results and conclude.

3.3 Dark matter spikes

In this section, we review properties of DM profiles around a BH of mass $M_{\rm BH}$. The density profile for DM around a BH is typically parameterised as (e.g. Gondolo et al. 1999),

$$\rho(r) = \rho_{\rm sp} \left(\frac{r}{r_{\rm sp}} \right)^{-\gamma}, \tag{3.1}$$

where $\rho_{\rm sp}$ and $r_{\rm sp}$ are the spike density and spike radius, respectively. From Gondolo et al. (1999), Sadeghian et al. (2013), it is known that in a fully relativistic analysis, the profile will be suppressed by a factor $F(r) = (1 - 2R_s/r)^3$, with R_s being the Schwarzschild radius of the central SMBH. This factor can be interpreted as depletion of the inner spike at radius $r = 2R_s = 4\mathrm{G}M_{\rm BH}/c^2$. As we use Newtonian N-body simulations in this work, we neglect this correction in the initial profile. As briefly discussed in the appendix, our implementation should still capture the leading effects. The profile in **Eq. (3.1)** is valid for, both, CDM and SIDM. Given the density profile, the 1D velocity dispersion of the DM spike can be obtained by solving the Jeans equation and is given by

$$\sigma_{\rm 1D}^2 = \frac{\mathrm{G}M_{\rm BH}}{r(1+\gamma)}, \tag{3.2}$$

assuming the potential is dominated by the BH. For the remainder of the section, we will discuss how the parameters $r_{\rm sp}, \rho_{\rm sp}$ are determined. First, we consider the case of CDM with a host halo described by a NFW profile. For CDM, $\gamma = (9 - 2\delta)/(4 - \delta)$, where δ is the index with which the DM profile of the host halo scales in the inner region. For example, NFW (Navarro et al. 1996), and Hernquist (Hernquist 1990) profiles scale as $\rho \propto r^{-1}$ at small radii, therefore, leading to a spike index of $\gamma = 7/3$ (Gondolo et al. 1999, Sadeghian et al. 2013). We have two more parameters in the spike profile, i.e. $r_{\rm sp}$ and $\rho_{\rm sp}$. For a CDM spike attached to a NFW profile, the spike radius can be shown to be $r_{\rm sp} := \alpha_f r_{\rm in}$, where $r_{\rm in}$ is the radius of influence, the factor α_f is approximately 0.2 for NFW like host halos (Merritt 2004a, Merritt 2004b, Kavanagh et al. 2020). The radius of influence can be determined using

$$2M_{\rm BH} = \int_0^{r_{\rm in}} 4\pi r^2 \rho_{\rm NFW}(r) \mathrm{d}r, \tag{3.3}$$

from which we get the following expression for the spike radius

$$r_{\rm sp} = \left[\frac{(3-\gamma) 0.2^{3-\gamma} M_{\rm BH}}{2\pi \rho_{\rm sp}} \right]^{1/3}. \tag{3.4}$$

Another requirement is that the spike profile joins onto the NFW profile of the host halo at $r = r_{\rm sp}$ (Gorchtein et al. 2010, Lacroix et al. 2017), i.e.,

$$\rho(r_{\rm sp}) = \rho_{\rm NFW}(r_{\rm sp}). \tag{3.5}$$

Equations (3.4) and (3.5) determine the two parameters r_{sp} and ρ_{sp} and $\rho_{\text{NFW}}(r)$ follows from the properties of the host halo.

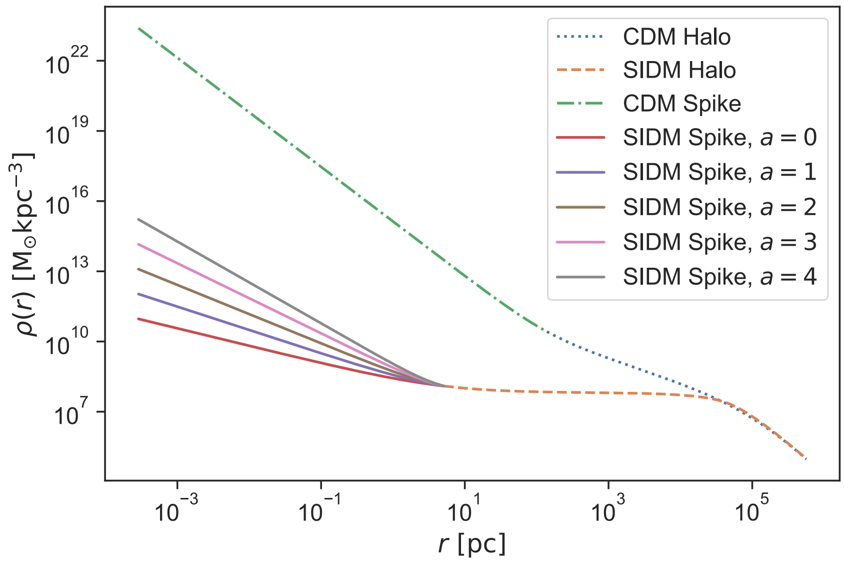

Figure 3.3.1: Plot illustrating different DM spike profiles for a SMBH with mass $M_{\text{BH}} = 10^9\,\text{M}_\odot$. The corresponding host halo has a mass of $M_{\text{vir}} \approx 3 \times 10^{13}\,\text{M}_\odot$. The solid lines correspond to spike profiles with indices $\gamma = (3 + a)/4$, where a is related to the nature of the velocity dependence of the cross-section characterised via $\sigma \propto v^{-a}$. The dashed line corresponds to the SIDM halo of the host halo outside the spike-radius. Dotted lines at the end mark a NFW profile of the host halo in the outer parts. Dashed-dotted lines correspond to the CDM spike with $\gamma = 7/3$.

For SIDM, the spike index is set by the nature of the velocity-dependence of the self-interaction cross-section. If the velocity dependence is given by $\sigma(v) \propto v^{-a}$, then the spike index is $\gamma = (3 + a)/4$, (Shapiro et al. 2014).

It is worth noting that for $a = 4$, the density profile scales as $r^{-7/4}$. The same applies for star clusters, as shown in J. N. Bahcall et al. (1976). The similarity of the profiles is due to the Coulombic nature of the interactions, whose cross-section has a v^{-4} dependence. The remaining two parameters, r_{sp} and ρ_{sp}, are related to the properties of the host halo, which we assume to have a cored profile (Adhikari et al. 2022) with a core radius r_c. Within the core, we have constant velocity dispersion, σ_0, and a constant core density, ρ_0. The host halo is usually assumed to be a NFW profile initially, and over time, the halo develops an isothermal core due to self-interactions, while the outer regions are still well described by a NFW profile. The parameters $\{\sigma_0, \rho_0\}$ are determined from σ_m and the NFW parameters of the initial halo in two steps: Firstly, the core radius r_c is determined from the scattering cross-section σ_m by demanding that at least one scattering event has taken place given within a given time t (assuming $t = 0$ as initial condition).

Specifically we have:

$$\frac{\langle \sigma v_{\rm rel} \rangle}{m_\chi} \rho_{\rm NFW}(r_c(t)) \cdot t \sim 1, \tag{3.6}$$

where $v_{\rm rel}$ is the relative velocity between DM particles. This equation implies that, starting from the initial NFW profile, the core radius will grow with time. Note however that the timescale of spike formation is typically much shorter than the self-interaction relaxation timescale. If the central black hole grows adiabatically, we would therefore expect the formation of a steep CDM spike initially, which will then subsequently relax to the steady state SIDM solution described above (cf also **Fig. 3.3.1** for a visualisation of the overall system at late times and for different velocity dependencies of the SIDM scatterings). If we are interested in the spike properties today, we would take $t = t_{\rm age}$ with $t_{\rm age}$ the age of the system under consideration.

To fully determine the SIDM halo parameters, one needs to also solve the spherical Jeans equation $\nabla(\rho_{\rm DM}\sigma_0^2) = -\rho_{\rm DM}\nabla\Phi(r)$ along with the Poisson equation $\nabla^2\Phi(r) = -4\pi G\rho_{\rm DM}$ (see (Kaplinghat et al. 2016, Jiang et al. 2023) for more details). The spike radius and spike density are then given by Shapiro et al. (2014), Alonso-Álvarez et al. (2024),

$$r_{\rm sp} = \frac{GM_{\rm BH}}{\sigma_0^2}, \tag{3.7}$$

and

$$\rho_{\rm sp} = \rho_0, \tag{3.8}$$

respectively. Since the potential in the inner regions is dominated by the SMBH, and since the contribution of stars and gas to the potential is negligible we neglect them in our study. We now study the evolution of spikes in the presence of DM self-interactions with numerical simulations, which we will describe in the next section.

3.4 Simulation setup

We employ the cosmological, hydrodynamical N-body code OpenGadget3 (e.g. Ragagnin et al. 2016, Groth et al. 2023, Dolag et al. in prep.) a derivative of Gadget-2 (Springel 2005) that performs gravitational force calculations using a tree method.

3.4.1 Numerical setup

We simulate velocity-independent, isotropic self-interactions. The self-interactions are modelled in a Monte-Carlo fashion by scattering pairs of numerical particles using OpenGadget3. The particular implementation used is described as rare self-interactions in Fischer et al. (2021), Fischer et al. (2022), Fischer et al. (2024). In this scheme, the probability that a numerical particle labelled i with mass m_i scatters off another numerical particle j with mass m_j is given by

$$P_{ij} = \frac{\sigma(v_{ij})}{m_\chi}\, m_j\, |v_{ij}|\, \Delta t\, \Lambda_{ij}, \tag{3.9}$$

where v_{ij} is the relative velocity between the numerical particles i and j, Δt is the time-step used in the simulation, Λ_{ij} is the kernel overlap integral and $\sigma(v_{ij})/m_\chi$ is the total cross-section per unit mass of DM particle. Note that the indices i, j are not summed over. Each particle is assigned a kernel adaptively such that each particle has at least $N_{\rm ngb}$ number of neighbours. In addition, all numerical DM particles have the same mass, i.e. $m_i = m_j = M_{N,DM}$. For more details on the implementation and the choice for the kernel, see appendix B of Fischer et al. (2021). A collection of kernels used in other modern implementations of SIDM in N-body codes can be found in Adhikari et al. (2022), equations 11–15. The SIDM implementation, we use, explicitly conserves energy and linear momentum (Fischer et al. 2024a).

We model accretion the following way: at the end of each time-step, we remove every particle that passes the innermost stable circular orbit $r_{\rm ISCO} = 3R_S = 6GM_{\rm BH}/c^2$, of the (assumed to be non-rotating) central BH. Here c is the speed of light. As mass accretion is negligible in all our simulations, i.e. $\Delta M_{\rm BH}/M_{\rm BH} \lll 1$, it is a good approximation to assume that the total BH mass does not change. The accretion rate is then given by the loss rate of the total number of particles.

3.4.2 Precision parameters

The simulations contain a number of parameters that control the precision of the force calculations. We fix the gravitational softening length, $\epsilon_{\rm soft}$, for the particles to be approximately the Schwarzschild radius of the BH, and it sets the smallest length scale of the simulated system. The opening angle for the gravitational force calculations using the tree method is chosen to be small enough to ensure that errors arising from the asymmetric force evaluation of the one-sided oct-tree (Barnes et al. 1986) are negligible. Similar values have been adopted by Kavanagh et al. (2020). We provide the numerical values in **Tab. 3.1**.

For all simulations we fix the time-step, Δt, to a constant value which is the same for all particles. We denote the maximum allowed value of the gravitational time-step corresponding to the gravitational force calculation as $\Delta t_{\rm grav}$. This is in practice at least 100 times smaller than the smallest dynamical timescale in the system. For simulations with SIDM, there is an additional condition that we have to respect for choosing the time-step, $\Delta t_{\rm SIDM}$. The condition being that the time-step must be small enough to ensure that the scattering probability stays well below unity. For more information see Fischer et al. (2024). Therefore, we choose the minimum of the two, i.e. $\Delta t = \min(\Delta t_{\rm grav}, \Delta t_{\rm SIDM})$. We ensure that this criterion is fulfilled for the entire simulation period. In **App. 3.D**, we show that energy is conserved numerically to within 0.1%. The time step is chosen to be small enough such that this criterion is fulfilled during the entire simulation.

Table 3.1: Precision parameters used in OpenGadget3.

Parameter	Value
`ErrTolForAcc`	10^{-4}
$\epsilon_{\rm soft}$	0.0017 pc
Δt	10^{-4} yr
$N_{\rm ngb}$	48

As described in the **section 3.4.1**, the scattering probability is calculated using kernels. The size of the kernel is chosen such that there are $N_{\rm ngb}$ number of particles within the kernel. The kernel size must be smaller or at the most be roughly equal to the physical mean-free-path of SIDM scatterings. This requirement ensures that, energy and momentum are not transferred per scattering on length scales that are greater than the mean-free-path. The ratio between the kernel size, h, and the mean free path, λ,

$$\frac{h}{\lambda} \approx \frac{\sigma}{m_\chi} \rho^{2/3} \sqrt[3]{\frac{3\, M_{\rm N,DM}\, N_{\rm ngb}}{\pi \sqrt{2}}}, \tag{3.10}$$

therefore indicates which cross-sections can be simulated faithfully. This ratio should at most be of order of unity in order to yield reliable results (Fischer et al. 2024a). See **Fig. 3.4.1** for a two-dimensional histogram of the kernel size to mean-free-path ratio as a function of radius (in units of $r_{\rm ISCO}$) and cross-section, σ/m. This figure shows that for radii close to the ISCO radius and $\sigma_m = 0.8\,{\rm cm}^2\,{\rm g}^{-1}$, the ratio h/λ gets larger than unity. In all other parts of this parameter space, this value is smaller than 1.

3.4.3 Astrophysical parameters

To ensure that we have a sufficient number of particles in the inner region to faithfully simulate the interesting physics of the spike, we adopt a slightly different prescription of the initial condition in our numerical analysis. Specifically we simulate the DM density around the BH with a truncated spike profile, which is given by

$$\rho(r) = \rho_{\rm sp} \left(\frac{r}{r_{\rm sp}}\right)^{-\gamma} \left(1 + \left(\frac{r}{r_t}\right)^{\eta}\right)^{-\alpha}, \tag{3.11}$$

where $r_{\rm sp}$ is the spike radius and $\rho_{\rm sp}$ the spike density, as before. Rather than imposing a cut 'by hand' in **Eq. (3.1)**, the profile is modified at large radii by a power law with a steeper slope, i.e., $\alpha > \gamma$ according to **Eq. (3.11)**, which provides a smooth truncation to the profile for larger radii. This truncated profile has been employed previously for the case $\eta = 1$ in the context of CDM N-body simulations in Kavanagh et al. (2020).

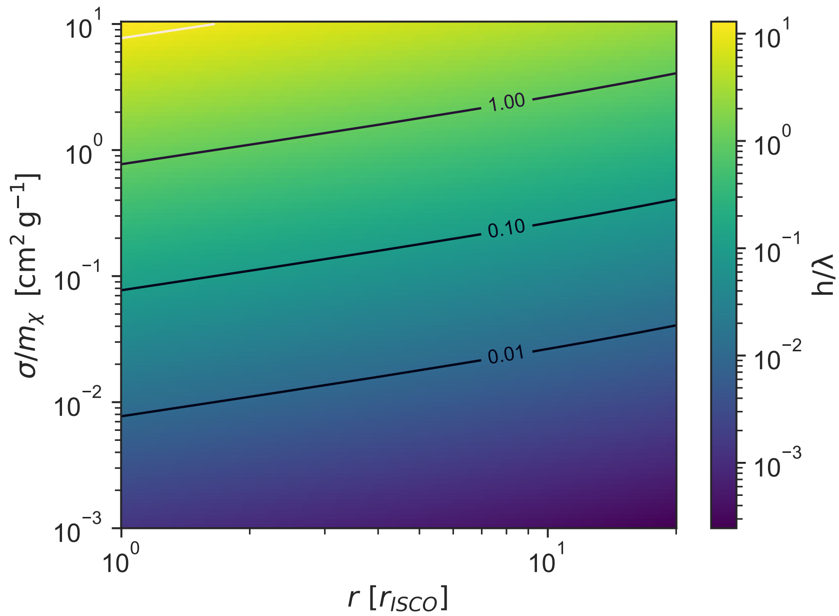

Figure 3.4.1: Two-dimensional histogram of the kernel size to mean-free-path ratio as a function of radius (in units of $r_{\rm ISCO}$) and cross-section, σ/m. The black lines correspond to constant values of h/λ.

We sample the radii using the spike profile as the target distribution, and for sampling velocities we use the Eddington-inversion method (Binney et al. 2008, Lacroix et al. 2018). In our simulation we sample particles in the radial range between $r_{\rm min} = r_{\rm ISCO}$ and $r_{\rm max} = 0.1 r_{\rm sp}$. We simulate a system that is similar to the OJ287 system described in Dey et al. (2018), Alachkar et al. (2023), which has a binary SMBH at the centre. In Dey et al. (2018) they estimate the mass of the primary SMBH $M_{\rm BH}$ to be $1.8 \times 10^{10}\,{\rm M}_\odot$ and the secondary SMBH to be $1.5 \times 10^8\,{\rm M}_\odot$. Since we are interested in studying an isolated DM spike, we only consider the primary SMBH in this work. The NFW profile parameters of the corresponding host halo follows from Chan et al. (2024). The virial mass of the host galaxy of OJ287 is obtained to be $M_{\rm vir} \approx 2 \times 10^{14}\,{\rm M}_\odot$ from the mass of the SMBH. This is achieved using the scaling relations between the virial mass of the host and the mass of the central SMBH (Bandara et al. 2009). Then, given the virial mass, the NFW parameters can be determined using mass-concentration relations (Dutton et al. 2014), yielding a concentration of $c \approx 4.8$.

In SIDM, for any given self-interaction cross-section, we solve the Jeans-Poisson equations to determine $\{\rho_0, \sigma_0\}$ of the SIDM halo. To this end, we use the publicly available isothermal code provided in Jiang et al. (2023). The only input needed is the time the system had to evolve to set the initial condition. In the following, we use the approximate age of the system ($t_{\rm age}$) to solve **Eq. (3.6)**, noting that at earlier times the spike density will have been larger. We find that for a scattering cross-section of $\sigma_m = 0.1\,{\rm cm}^2\,{\rm g}^{-1}$ and an age of $t_{\rm age} = 10\,{\rm Gyr}$ the resulting density is $\rho_0 \sim 10\,{\rm M}_\odot\,{\rm pc}^{-3}$. The choice of these parameters should not affect our results that we present in the next sections. In **Tab. 3.2** we provide the parameters of the simulated spike profile. We note that the collisionless case is setup with $\gamma = 3/4$ instead of $7/3$. This choice is unphysical, however, we use it to estimate the loss-cone contribution (see **section 3.5** for more details). N-body simulations of CDM spikes with $\gamma = 7/3$ have been studied in Kavanagh et al. (2020), Kavanagh et al. (2024), Mukherjee et al. (2024). The gravitational timescale is simply given by

$$t_{\rm G} \sim r^{3/2}({\rm G}M_{\rm BH})^{-1}, \tag{3.12}$$

since $M_{\rm BH}$ contributes the most to the gravitational dynamics.

Finally, the relaxation timescale due to self-interactions is given by

$$t_{\rm SIDM} = \frac{1}{\rho(r)\sigma_m\,\sigma_{\rm 1D}} \simeq \frac{r^{\gamma+1/2}}{\sqrt{{\rm G}M_{\rm BH}}r_{\rm sp}^{\gamma}\rho_{\rm sp}\sigma_m}, \tag{3.13}$$

where in the last step we used $\sigma_{\rm 1D}^2(r) \sim {\rm G}M_{\rm BH}/r$ from **Eq. (3.2)** and the density profile given in **Eq. (3.1)**.

3.5 Black hole mass accretion with CDM

In the case of collisionless DM, there are no processes that can lead to the loss of angular momentum, which prevents the effective accretion of DM particles. Still, there can be some particles with insufficient angular momentum and energy such that they get accreted by the BH. In this section – in addition to the numerical analysis – we attempt an order-of-magnitude analytical estimate for the accretion rate due to the lose-cone population in the initial conditions of the $\gamma = 3/4$ simulation. Therefore, we use the same initial conditions as the ones used in the SIDM simulation. A fully relativistic counterpart of this calculation can be found in Shapiro (2023). Since the major contributor to the gravitational potential is the SMBH, the accretion rate of CDM through a spherical surface can be calculated from the initial phase-space distribution, $f(E, J)$, where E and J are energy and angular momentum, respectively. Here, $f(E, J)$ is normalised to yield the total mass when integrated over the full phase space, i.e.

$$\rho(r) = \int f(E, J){\rm d}^3\mathbf{v}. \tag{3.14}$$

In CDM spikes, the contribution to the accretion comes from particles that initially have a mostly radial velocity with small angular momentum. The mass of the phase space patch with the radial velocity directed towards the BH is given by

$${\rm d}M(\mathbf{x}, \mathbf{v}) = \frac{1}{2}f(\mathbf{x}, \mathbf{v})\,{\rm d}^3\mathbf{x}\,{\rm d}^3\mathbf{v}, \tag{3.15}$$

where the factor 1/2 accounts for the radially inward moving particles. Since the initial distribution is spherically symmetric and isotropic in, both, coordinate and velocity subspaces, we can write for the mass in the interval dr dE dJ centred on (r, E, J):

$$M^{-}(r, E, J)\,\mathrm{d}r\,\mathrm{d}E\,\mathrm{d}J = 8\pi^2 f(E, J)\frac{J}{|v_r|}\mathrm{d}r\,\mathrm{d}E\,\mathrm{d}J, \tag{3.16}$$

where the ”$^{-}$” indicates that it is the mass that is moving inwards and will be accreted.

$\rho_{\rm sp}$ ($\mathrm{M_\odot\,pc^{-3}}$)	γ	$r_{\rm sp}$ (kpc)	α	$r_{\rm t}$ ($r_{\rm ISCO}$)	σ_m ($\mathrm{cm^2\,g^{-1}}$)
20	3/4	1.5	4	200	0
20	3/4	1.5	4	200	0.2
20	3/4	1.5	4	200	0.4
20	3/4	1.5	4	200	0.6
20	3/4	1.5	4	200	0.8
20	3/4	1.5	4	200	1.4
20	3/4	1.5	4	200	2.0
20	3/4	1.5	4	200	4.0
20	3/4	1.5	4	200	8.0
20	1/2	1.5	4	500	1.0
20	7/4	1.5	2	200	$2 \cdot 10^{-5}$

Table 3.2: Physical parameters of the DM spike. The columns from the left to the right are the following: spike density $\rho_{\rm sp}$, spike index γ, spike radius $r_{\rm sp}$, truncation index α, truncation radius r_t, and finally the cross-section per unit mass σ_m . The first row corresponds to the collisionless case, which we nevertheless assume to have the same initial spike profile to enable a more direct comparison. For all our simulations, we have set the profile parameter η to be 1.

Hence, the accretion rate through a spherical surface of radius R is given by

$$\dot{M} = \int_{\Phi(R)}^{\infty} \mathrm{d}E \int_0^{J_{\min}} \mathrm{d}J\,|v_r| M^{-}(r, E, J) \tag{3.17}$$

$$= \int_{\Phi(R)}^{\infty} \mathrm{d}E \int_0^{J_{\min}} \mathrm{d}J\,|v_r| 8\pi^2 f(E, J)\frac{J}{|v_r|} \tag{3.18}$$

$$= 8\pi^2 \int_{\Phi(R)}^{\infty} \mathrm{d}E \int_0^{J_{\min}} f(E, J)\,J\mathrm{d}J. \tag{3.19}$$

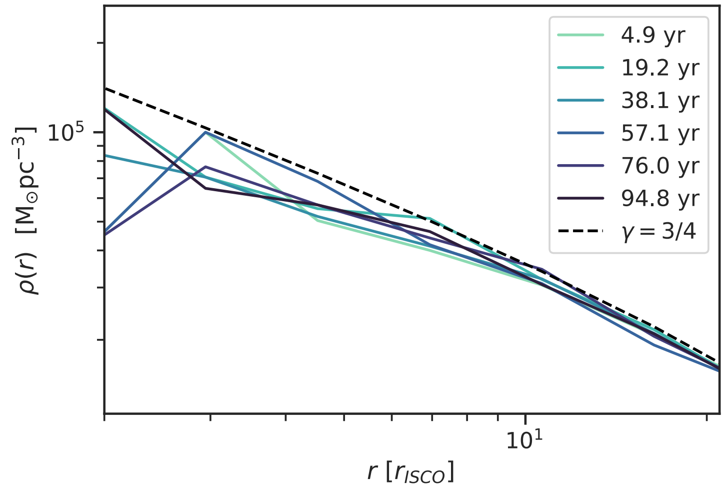

Figure 3.5.1: Evolution of the CDM spike profile. The initial condition contains particles sampled from the profile given by the dashed line. The bottom panel displays the deviation from the initial profile.

For our system, the distribution function has no dependence on angular momentum, and therefore the integral can be evaluated numerically using the $f(E)$ we constructed using the Eddington inversion method.

When computing the integral we set the upper limit for the energy integral to 0 instead of ∞ since the spike is gravitationally bound and has been set up dynamically stable in the ICs. Hence, no particle has an energy greater than 0 by construction. Similarly, the lower limit for the energy integral cannot be smaller than the potential energy on the surface of interest.

The minimum angular momentum for a bound orbit is, $J_{\min} = R\sqrt{2\,(E + \mathrm{G}M/R)}$, and this expression follows from the Keplerian two-body energy of the DM-SMBH system evaluated at the pericentre, with the pericentre being at the imaginary radial surface.

Taking the same halo parameters as used for the simulation (cf. **Tab. 3.2**), the integral above evaluates to $5.1\,\mathrm{M}_\odot\,\mathrm{yr}^{-1}$ for $R = r_{\mathrm{ISCO}}$. In the numerical simulations we find a somewhat smaller value, $\dot{M}_{\mathrm{sim}} \approx 1.7\,\mathrm{M}_\odot\,\mathrm{yr}^{-1}$, which we estimated by linear fitting for an initial period of 15 yr, where the accretion rate is approximately linear. For later stages, due to the loss cone depletion and the fact that the lost mass is not replenished from the outer halo, the accretion rate will decrease further. This implies that $f(E, J)$ of the simulated system will slowly change in the collisionless case due to accretion. In contrast, in the SIDM case, $f(E, J)$ is affected by the DM scattering events even in the absence of accretion.

The result of our N-body simulation for the collisionless case is shown in **Fig. 3.5.1**. The profile undergoes evolution due to accretion. As time progresses, the accretion rate goes down as the loss cone is getting depopulated. This leads to a stable profile at later times. Note that in our simulation we start from a fully populated spike with parameters as given in **Tab. 3.1** and do not take into account the spike formation. In reality, as the CDM spike forms due to adiabatic contraction, it is natural to expect that the particles in the loss cone are steadily accreted during the formation of the spike. Since we start with a profile that has not undergone such a process, the initial accretion is artificially high in the CDM simulations.

3.6 Black hole mass accretion with SIDM

In **section 3.6.1** we fit an ansatz for accretion rate as function of σ_m in the LMFP and the IMFP regime to simulations and verify it against theoretical expectations. Later, in **section 3.6.2** we obtain an approximate expression for the maximum accretion rate given the parameters M_{BH}, r_{sp}, and ρ_{sp}.

3.6.1 Accretion rate and SIDM cross-section

Let us start this subsection with a discussion of the gravothermal fluid equations in order to obtain a qualitative understanding of the behaviour of the spike index as well as the accretion rates for varying cross-sections. The gravothermal fluid equations can be written as (Balberg et al. 2002b, Koda et al. 2011, Shapiro et al. 2014, Essig et al. 2019, D. Yang et al. 2022):

$$\frac{\partial M}{\partial r} = 4\pi r^2 \rho, \tag{3.20}$$

$$\frac{\partial(\rho\sigma_{1\mathrm{D}}^2)}{\partial r} = -\frac{\mathrm{G}M\rho}{r^2}, \tag{3.21}$$

$$\frac{\partial L}{\partial r} = 4\pi r^2 \rho\sigma_{1\mathrm{D}}^2 \frac{D}{Dt} \ln \frac{\sigma_{1\mathrm{D}}^2}{\rho}, \tag{3.22}$$

$$\frac{L}{4\pi r^2} = -m_\chi \kappa \frac{\partial \sigma_{1\mathrm{D}}^2}{\partial r}. \tag{3.23}$$

Here, D/Dt denotes a Lagrangian time derivative, κ characterizes the heat conductivity, L is the luminosity, and M is the enclosed mass. The luminosity quantifies the heat flux arising due to self-interactions. A positive luminosity implies that energy is flowing outwards. **EQS. (3.20)** to **(3.22)** are the first three moments of the collisional Boltzmann equation and **Eq. (3.23)** provides a closure relation. **Eq. (3.20)** is the continuity equation corresponding to the conservation of mass, **Eq. (3.21)** is the equation of hydrostatic equilibrium, **Eq. (3.22)** corresponds to the first law of thermodynamics. Finally, **Eq. (3.23)** defines the heat flux. If the evolution is dominated by the effects of SIDM (instead of gravity), the system is said to be in the short-mean-free-path (SMFP) regime, while if the evolution is dominated by effects of gravity the system is said to be in the long-mean-free-path (LMFP) regime. These regimes are delineated with the help of the Knudsen number. It is defined as the ratio of the scale height to mean-free-path corresponding to SIDM scatterings.

$$\mathrm{Kn}(r) = \frac{\lambda(r)}{H(r)} = \frac{1}{r\rho(r)\sigma_m}. \tag{3.24}$$

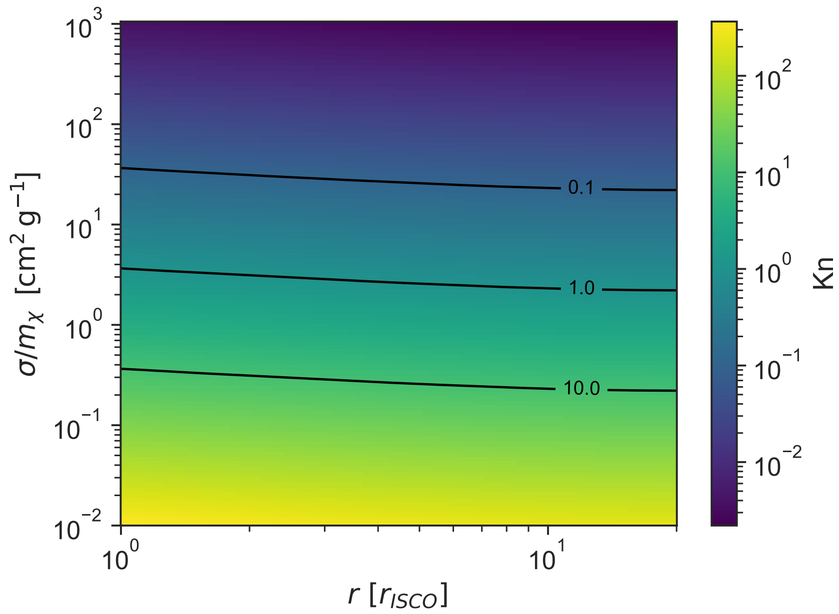

Figure 3.6.1: Radial profile of Knudsen number for varying cross-sections.

Here, λ is the mean free path for a given self-interaction cross-section, i.e. $\lambda = m_\chi/(\rho\sigma)$. H is the gravitational scale height, effectively given by the distance from the BH, $H \simeq t_G\sigma_{1D} \sim r^{3/2}r^{-1/2} = r$ (Shapiro et al. 2014). We show the radial profile of the Knudsen number for the case $\gamma = 3/4$ in **Fig. 3.6.1**, observing a scaling $\sim r^{-1/4}$ as expected. In the LMFP, Kn $\gg 1$ and in the SMFP, Kn $\ll 1$. We further identify Kn ~ 1 as the intermediate-mean-free-path (IMFP) regime. Depending on the regime, the nature of thermal conductivity changes. Under the assumption of velocity isotropy, the conductivity in these regimes scales as

$$\kappa_{\rm lmfp} \propto \rho\frac{H^2}{t_{\rm SIDM}} \quad \text{yielding} \quad L_{\rm lmfp} \propto \frac{1}{t_{\rm SIDM}} \propto (\sigma_m) \tag{3.25}$$

for the LMFP and

$$\kappa_{\rm smfp} \propto \rho\frac{\lambda^2}{t_{\rm SIDM}} \quad \text{yielding} \quad L_{\rm smfp} \propto \frac{\lambda^2}{t_{\rm SIDM}} \propto (\sigma_m)^{-1} \tag{3.26}$$

for the SMFP.

In the weakly collisional limit, $\lambda \gg H$, and the system is in the LMFP. On the other hand, in the limit of large cross-section, the system will be in the SMFP regime, since $\lambda \ll H$. Moreover, for $\sigma_m \to \infty \implies \kappa_{\rm smfp} \to 0$, implying that the SIDM effectively behaves like a non-conducting fluid in this limit. Given the conductive nature of SIDM spikes, one can seek a steady-state solution to the spike density profile, by demanding that the spike has a constant luminosity. Such a constant luminosity could lead to a steady-state accretion (Pringle 1981, Frank et al. 2002, Carroll et al. 2017). This requirement can be used to determine what the spike-index needs to be. For example, in the constant cross-section case, we require from Eqs. (3.23) and (3.25) that $L \propto r^{3/2} r^{-2\gamma} = \text{const.}$, and this results in $\gamma = 3/4$.

Let us now present the numerical evolution of the spike profile and compare it to analytical expectations. Specifically, we are interested in the question if and how quickly the steady-state profiles are reached if we start with profiles that are either steeper or shallower than the expected equilibrium state with $\gamma = 3/4$.

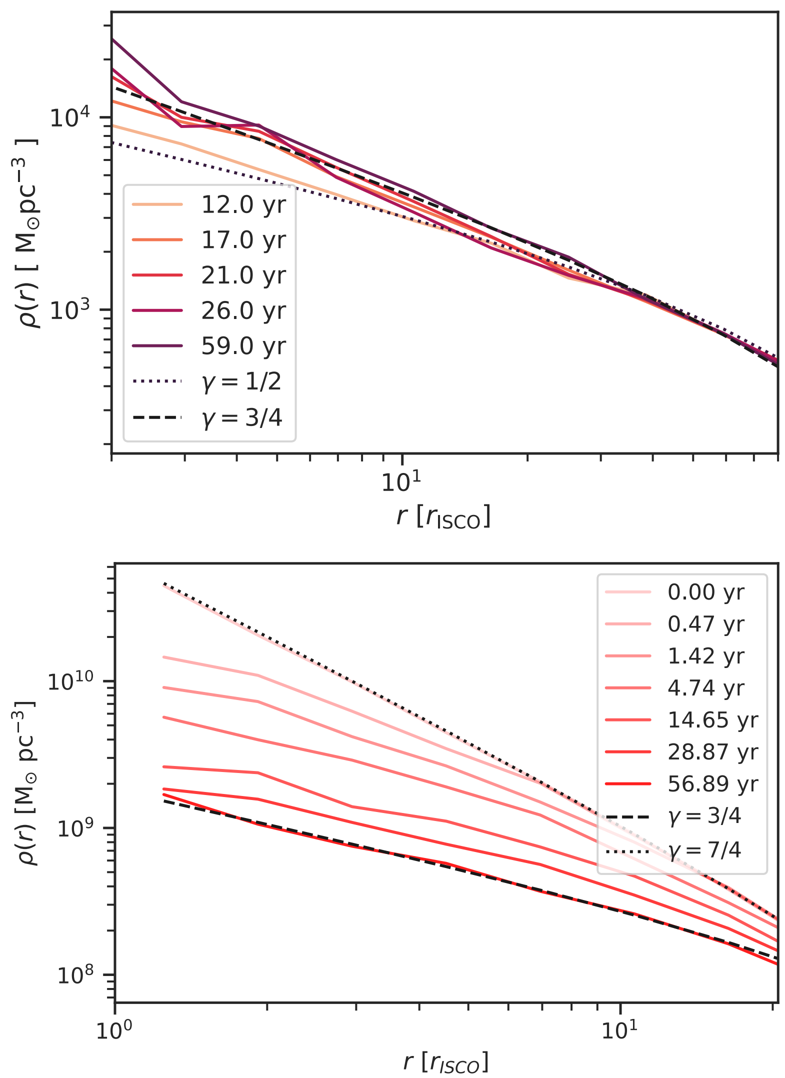

Figure 3.6.2: Spike density profile in the inner regions at various times for a DM spike setup initially with two different spike indices. Left and right panel correspond to $\{\gamma, \sigma_m\}$ of $\{1/2, 1.0\,\text{cm}^2\,\text{g}^{-1}\}$, and $\{7/4, 2 \cdot 10^{-5}\,\text{cm}^2\,\text{g}^{-1}\}$ respectively. In both panels, the dotted lines are the initial density profile that is sampled and dashed lines correspond to a spike profile with index 3/4. For both steeper and shallower starting profiles we see that the spike index evolves towards $\gamma = 3/4$.

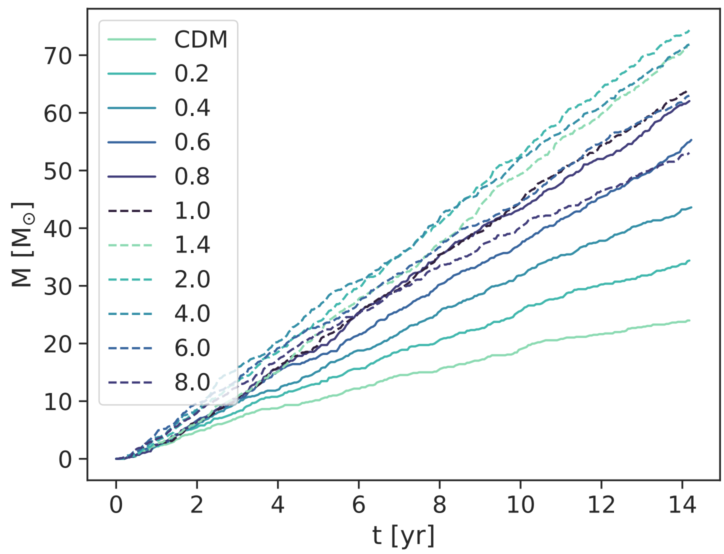

Figure 3.6.3: Accreted mass vs. time for varying cross-sections. The labels indicate the cross-section in units of $\mathrm{cm^2\,g^{-1}}$. Solid lines correspond to $\sigma_m < 1.0\,\mathrm{cm^2\,g^{-1}}$ and dashed lines to $\sigma_m \geq 1.0\,\mathrm{cm^2\,g^{-1}}$.

In **Fig. 3.6.2** we show the evolution for initial values $\gamma = 7/4$ and $\gamma = 1/2$, respectively. We immediately see that for both cases the system transitions quickly towards the steady-state solution, $\gamma = 3/4$. This result is expected because, for $\gamma \neq 3/4$ and for velocity-independent scatterings, the luminosity is not constant in space nor time. Effectively, this leads to accretion rates that vary with time until the system settles into the static profile. We also see that the spike radius of the newly forming profile is growing with time. Note that we have used different cross-sections in the simulations owing to the different densities reached in the inner regions (cf. **Tab. 3.2**). We expect that also for larger radii and on larger timescales the mass that the DM spike loses to the BH gets replenished. It will be interesting to test this in simulations in a cosmological setting.

The steady-state spike solutions introduced in Shapiro et al. (2014) are valid in the LMFP regime. In the other extreme, we have the hydrodynamic limit, where the static solution requires a spike index of 3/2 (Shapiro et al. 2014). In our simulations we however concentrate on the LMFP and IMFP regimes. In **Fig. 3.6.3** we plot the accreted mass versus time for a range of cross-sections including the collisionless case for comparison. As expected, the SIDM accretion rates are larger than the CDM accretion rates for the same initial conditions. We indicate cross-sections $\sigma_m < 1\,\mathrm{cm^2\,g^{-1}}$ by solid lines, and $\sigma_m \geq 1\,\mathrm{cm^2\,g^{-1}}$ by dashed lines, observing that the kernel-size to mean-free-path ratio becomes greater than 1 for cross-sections $\gtrsim 1\,\mathrm{cm^2\,g^{-1}}$. In **Fig. 3.6.4** we show the simulated accretion rates as a function of the self-interaction cross-section. We observe that within the LMFP regime the accretion rate increases linearly to an excellent approximation. However, for cross-sections $\sigma_m \gtrsim 1.0\,\mathrm{cm^2\,g^{-1}}$, the mass accretion rate does no longer grow linearly but increases more slowly and for even larger cross-section starts to decrease. This qualitative trend can be understood as being due to the transition from the LMFP regime to the SMFP regime for increasing cross-sections. The fact that cross-sections of the order $1\,\mathrm{cm}^2\,\mathrm{g}^{-1}$ correspond to the transition regime can also be inferred from **Fig. 3.6.1**.

In the following let us try to obtain an analytical understanding of the observed accretion rates. We have already established that the accretion rates are proportional to the luminosity L in the gravothermal fluid equations and the different scaling in the LMFP and SMFP regimes, cf. **Eq. (3.25)** and **Eq. (3.26)**. We therefore make the following ansatz for the fitting function,

$$\dot{M} = C + \left(A\sigma_m + \frac{B}{\sigma_m}\right)^{-1}. \tag{3.27}$$

The RHS of the above equation is also motivated by the standard expression for thermal conductivity in the intermediate-mean-free-path (IMFP) regime (Koda et al. 2011, D. Yang et al. 2022). The expression is a simple smooth interpolation from the LMFP regime that has $\kappa_{\mathrm{lmfp}} \propto \sigma_m$ to the SMFP regime with $\kappa_{\mathrm{smfp}} \propto (\sigma_m)^{-1}$. Alternate interpolating functions have also been discussed in the literature (Nishikawa et al. 2020, Mace et al. 2025). In **Fig. 3.6.4**, we show accretion rates extracted from the simulation, along with **Eq. (3.27)** fitted with the simulation data. The fitted values are: $A \approx 0.056\,\mathrm{M}_\odot^{-1}\,\mathrm{yr\,cm^{-2}\,g} \approx 585 r_{\mathrm{sp}}^{-3/2}\rho_{\mathrm{sp}}^{-1}(\mathrm{G}M_{\mathrm{BH}})^{-1/2}\mathrm{cm^{-2}\,g}$, $B \approx 0.27\,\mathrm{M}_\odot^{-1}\,\mathrm{yr\,cm^2\,g^{-1}} \approx 2823 r_{\mathrm{sp}}^{-3/2}\rho_{\mathrm{sp}}^{-1}(\mathrm{G}M_{\mathrm{BH}})^{-1/2}\mathrm{cm^2\,g^{-1}}$ and $C \approx 3.67\,\mathrm{M}_\odot\,\mathrm{yr^{-1}\,cm^{-2}\,g} \approx 1.6\times10^{-4} r_{\mathrm{sp}}^{3/2}\rho_{\mathrm{sp}}(\mathrm{G}M_{\mathrm{BH}})^{1/2}$, where in the second step we expressed the constants in units comprised of the parameters of the system. To extract the LMPF limit from the above, we expand the RHS around zero and retain only the lowest-order contribution. Thus, we get, $\dot{M} \approx C + B^{-1}\sigma_m$. The constant factor C captures the CDM limit, that is it captures the contribution to the accretion rate coming from the particles that have $J < J_{\mathrm{min}}$. The second term directly captures the contribution to the accretion rate coming from the self-interactions. In **App. 3.C** we provide an analytical evaluation of this coefficient. Similarly, for the SMFP limit, we expand the RHS around ∞, and we obtain $\dot{M} \approx C + A(\sigma_m)^{-1}$. We show these fits along with the data points in **Fig. 3.6.4**, observing an excellent agreement with our numerical results.

3.6.2 Maximum accretion rate

In this subsection we extend the validated model to DM spikes with different spike parameters and SMBH masses and calculate the corresponding accretion rates. Then, we compare it to the Eddington accretion rate $\dot{M}_{\mathrm{Edd}}$. The Eddington accretion rate, $\dot{M}_{\mathrm{Edd}}$, depends linearly on M_{BH}, i.e. $\dot{M}_{\mathrm{Edd}} = L_{\mathrm{Edd}}(0.1c^2)^{-1} \approx (2.3\times10^{-8}\mathrm{M}_\odot\,\mathrm{yr}^{-1})M_{\mathrm{BH}}/\mathrm{M}_\odot$ (Inayoshi et al. 2020). In the simulations we have run, we see in **Fig. 3.6.4** that the accretion rate maxes out around $2.0\,\mathrm{cm}^2\,\mathrm{g}^{-1}$ in the IMFP regime. This regime can be identified with $\mathrm{Kn}(\mathrm{r_{ISCO}}) \sim 1$. Therefore, we approximate the maximum accretion rate as the accretion rate corresponding to $\mathrm{Kn}(\mathrm{r_{ISCO}}) = 1$. For a SMBH-spike system characterized by the parameters $\{r_{\mathrm{sp}}, \rho_{\mathrm{sp}}, M_{\mathrm{BH}}\}$, this condition leads to (cf. **Eq. (3.24)**)

$$\sigma_m = \frac{\sqrt{c}}{\left(6\mathrm{G}M_{\mathrm{BH}}r_{\mathrm{sp}}^3\right)^{1/4}\rho_{\mathrm{sp}}}. \tag{3.28}$$

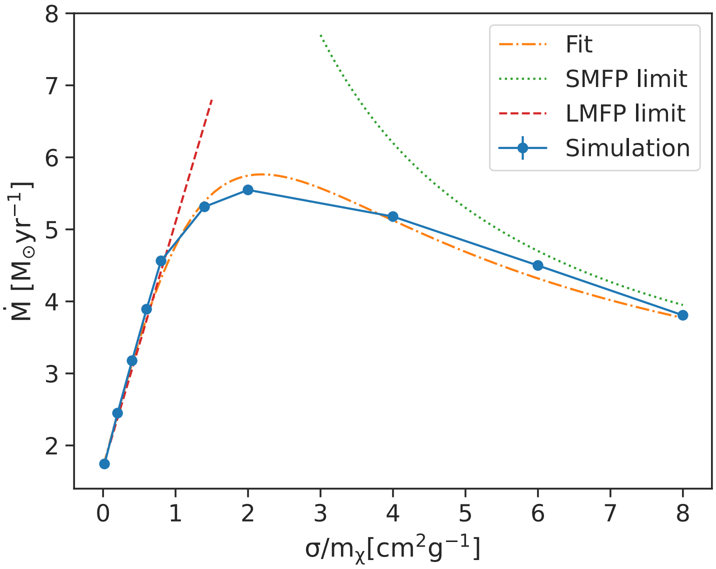

Figure 3.6.4: Initial accretion rate vs. σ_m for all simulated cross-sections. The solid line corresponds to the accretion rate inferred from the simulation, dashed-dotted line to the full fit, dashed line to the LMFP limit of **Eq. (3.27)**, dotted line to the SMFP limit of **Eq. (3.27)**.

The maximum accretion rate $\dot{M}_{\rm max}$ in terms of the Eddington accretion rate then can be approximated from **Eq. (3.40)** to be[1],

$$\frac{\dot{M}_{\rm max}}{\dot{M}_{\rm Edd}} \sim 3\times 10^{-15}\beta\left(\frac{M_{\rm BH}}{\rm M_\odot}\right)^{1/4}\left(\frac{\rho_{\rm sp}}{\rm M_\odot\,kpc^{-3}}\right)\left(\frac{r_{\rm sp}}{\rm kpc}\right)^{3/4}. \tag{3.29}$$

Here, β is a free parameter of the gravothermal fluid model arising from the definition of thermal conductivity in LMFP. See **App. 3.C** for more details. This suggests that for high-density spikes, such as in the system J1205−0000 (W.-X. Feng et al. 2022), where at the time of the formation of the seed the central density is $\rho_0 \sim 10^{19}\,\rm M_\odot\,kpc^{-3}$, the accretion can be super-Eddington. However, in that particular scenario the high-density spikes will be in the SMFP regime, such that **Eq. (3.29)** does not directly apply. Therefore, a quantitative analysis in this case would require a self-consistent formation simulation of DM spikes, which we defer to future work.

[1]For simplicity, we extrapolate the simple linear behaviour valid within the LMFP regime, which slightly overestimates the actual accretion rate, but is sufficient for the precision we aim for.

3.7 Discussion and Conclusion

In this paper, we investigated the evolution of the DM profile as well as the accretion rates of DM spikes around SMBHs. We found that the spike profile quickly reaches a quasi-steady state consistent with expectations from analytical arguments. We also found that for small self-interaction cross-sections (corresponding to the LMFP regime), the accretion rate increases linearly with the same, reaches a maximum in the IMFP regime and then drops again towards very large cross-sections.

The maximum accretion rate possible in a DM spike depends on spike profile parameters, which in turn depend on σ_m. In addition, if we assume that a CDM spike precedes an SIDM spike during the formation phase, then during the phase of transitioning from a CDM to SIDM spike, the accretion rates can be Super-Eddington for large spike densities.

There are a few caveats that come with our modelling approach: Firstly and most obviously, we assumed Newtonian dynamics, even in regions close to the SMBH. It would not be too hard to include general relativistic corrections in a post-Newtonian treatment. In the appendix, we have estimated the magnitudes of the first post-Newtonian terms. However, in this work, we wanted to understand the behaviour of accretion rates as a function of σ_m, given the Newtonian SIDM spike model (Shapiro et al. 2014). To also take into account relativistic effects, a next step would be to implement DM self-interactions in an SPH-based numerical relativity code (Rosswog et al. 2021).

In this work we simulate SIDM with a velocity-independent isotropic cross-section. In contrast, often a velocity-dependent cross-section is assumed to address the ΛCDM small scale structure problems while at the same time avoiding strong constraints at high velocities. However, in the context of the DM spike we find that also significantly smaller and therefore unconstrained cross-sections can be relevant. In fact velocity-independent scatterings are generally even much less constrained in the current context as the velocity dispersion in the DM spike is typically very large compared to other astrophysical systems. Also, note that simple light mediator models which would result in a velocity dependent cross-section are severely constrained by complementary probes (Bringmann et al. 2017, Kahlhoefer et al. 2017). On the other hand it is very easy to realise a well-motivated velocity independent scenario from a particle physics perspective, see e.g. Bringmann et al. (2023).

In summary, we have performed the first *N*-body simulations of SIDM spikes around SMBHs and studied the dependence of the accretion rates on the velocity-independent self-interaction cross-section.

- The density profile of the DM spike always converges to a profile with a spike index $\gamma \approx 3/4$ regardless of the spike index of the initial power-law profile.

- We find that the accretion rate grows linearly with the self-interaction cross-section in the LMFP regime, which can be explained by a simple analytical model. A calibration of the free parameter, β, in the gravothermal fluid model for DM spikes, can be found in **App. 3.C**.

In addition, we also observe that the accretion rates scale non-linearly with the cross-section in the IMFP regime. In both regimes, our simulations match analytic expectations given the nature of conductivity of SIDM. The accretion rates can also be super-Eddington for reasonable spike parameters.

- These increased accretion rates could be incorporated in the subgrid models of BHs in N-body codes with which cosmological simulations of SIDM are performed.

Acknowledgements

SVM and MB thank Stephan Rosswog for helpful discussions on numerical relativity. SVM thanks Sowmiya Balan and Felix Kahlhoefer for discussions. MSF is delighted to thank Rainer Spurzem for a helpful discussion on the gravothermal fluid model. All authors thank members of Darkium SIDM Journal Club for discussions. We acknowledge funding by the Deutsche Forschungsgemeinschaft (DFG, German Research Foundation) under Germany's Excellence Strategy – EXC 2121 "Quantum Universe" – 390833306. MSF acknowledges support by the COMPLEX project from the European Research Council (ERC) under the European Union's Horizon 2020 research and innovation program grant agreement ERC-2019-AdG 882679. The simulations have been carried out on the computing facility Hummel (HPC-Cluster 2015) of the University of Hamburg. Preprint numbers: DESY-25-076.

Appendix

3.A Post-Newtonian corrections

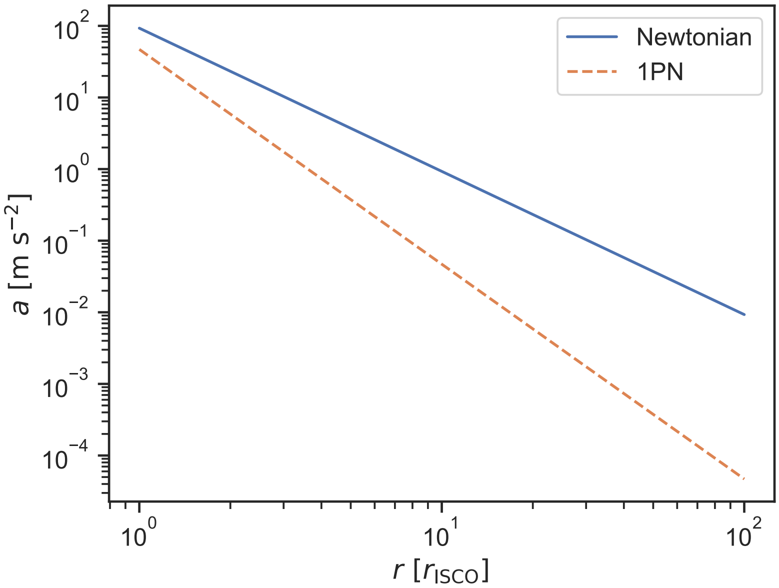

Figure 3.A1: Newtonian acceleration, and 1PN contribution to the acceleration, plotted against distance of the test particle from the SMBH. The solid line and dashed line corresponds to the Newtonian and 1PN term, respectively.

Post-Newtonian corrections to the orbital evolution are neglected in our simulations. We compare the magnitude of the correction to the Newtonian acceleration Fig. 3.A1. The relative acceleration of a binary at 1PN is given by Poisson et al. (2014),

$$\begin{aligned}\mathbf{a} = &-\frac{\mathrm{G}M}{r^2}\hat{\mathbf{r}} - \frac{\mathrm{G}M}{c^2r^2}\left[(1+3\mu)v^2 - 3/2\mu\dot{r}^2 - 2(2+\mu)\frac{\mathrm{G}M}{r}\right]\hat{\mathbf{r}} \\ &- \frac{\mathrm{G}M}{c^2r^2}\left[2(\mu+2)\dot{r}v\right]\hat{\mathbf{v}}. \end{aligned} \tag{3.30}$$

Here, $M = M_{\rm BH} + m$, $\mu = M_{\rm BH}m/M^2$ with m being the mass of the orbiting particle. The above expression is weakly dependent on m for any $m \lll M_{\rm BH}$, in other words $M \approx M_{\rm BH}$ and $\mu \approx 0$. The variables r, and $\dot{r}$ can be expressed in terms of the orbital elements namely, semi-major axis a, eccentricity e and true anomaly f as, $r = a(1-e^2)/(1+e\cos(f))$ and $\dot{r} = \sqrt{\mathrm{G}M/(a(1-e^2))}e\sin(f)$. We compare the magnitude of the Newtonian acceleration to the magnitude of the 1PN contribution in **Fig. 3.A1**. Since we are only interested in order of magnitude estimate, we choose $e = 0$ for convenience. Therefore, the tangential 1PN correction is initially zero. The x-axis denotes the initial separation distance in units of $r_{\rm ISCO}$ of the primary and the y-axis the acceleration. For

$r \sim r_{\rm ISCO}$, the 1PN correction is subleading but nevertheless numerically relevant compared to the Newtonian force. Nevertheless, to obtain a first estimate and also facilitate a comparison with results in the literature, we neglect these relativistic corrections and only study the Newtonian SIDM spike model in this paper.

3.B Eddington-Inversion

Given a density profile, $\rho(r)$, the corresponding velocity distribution can be obtained by inverting the following equation,

$$\rho(r) = 4\pi\sqrt{2}\int_0^{\Psi(r)} f(\mathcal{E})\sqrt{\Psi(r)-\mathcal{E}}\,\mathrm{d}\mathcal{E}. \tag{3.31}$$

Here, Ψ is the negative of the gravitational potential, $\mathcal{E} = \Psi(r) - v^2/2$ is the negative of the relative specific energy. **Eq. (3.31)** is recast from of $\rho(r) \propto \int f(r, v)\mathrm{d}^3\mathbf{v}$. Inverting **Eq. (3.31)**, we obtain

$$f(\mathcal{E}) = \frac{1}{\sqrt{8}\pi^2}\frac{\mathrm{d}}{\mathrm{d}\mathcal{E}}\int_0^{\mathcal{E}}\frac{\mathrm{d}\Psi}{\mathcal{E}-\Psi}\frac{\mathrm{d}\rho}{\mathrm{d}\Psi}. \tag{3.32}$$

In our case, $\Psi(r) = \mathrm{G}M_{\rm BH}/r$. Therefore, the truncated density profile given in **Eq. (3.11)** can be written as,

$$\rho(\Psi) = \rho_{\rm sp}\left(\frac{\Psi}{\mathrm{G}M_{\rm BH}r_{\rm sp}}\right)^{-\gamma}\left(1+\left(\frac{\Psi}{\mathrm{G}M_{\rm BH}r_t}\right)^{\eta}\right)^{-\alpha}. \tag{3.33}$$

Using **Eq. (3.33)** in **Eq. (3.32)**, and after some algebra, we compute the integral analytically using Mathematica for a fixed η. Then, given the $f(\mathcal{E})$, we compute the $f(v)$ as follows,

$$f(v, r) = 4\pi v^2\frac{f(\mathcal{E}(v, r))}{\rho(r)}, \tag{3.34}$$

here $f(v)$ is evaluated for every sampled particle. Let us suppose that particle i located at r_i has a velocity of magnitude v_i. To compute v_i, we first find the cumulative distribution function $F(v)$ from the distribution function $f(v, r_i)$. Then we employ the inverse transform sampling method to find v_i. That is, we draw a uniform random variable u in the interval $[0, 1]$, and then we set $v_i = F^{-1}(u)$.

3.C Accretion rate

In this appendix we provide additional details on the analytical treatment of the accretion rate. We start by reviewing the relation between the luminosity L and the accretion $\dot{M}$. The total energy of a particle in the gravitational potential of a SMBH is given by $E = -\mathrm{G}M_{\rm BH}m/r$. Therefore, the differential energy change across a small distance $\mathrm{d}r$ is $\mathrm{d}E = \mathrm{d}r\mathrm{G}M_{\rm BH}m/2r^2$. In SIDM spike, the DM particles transport energy from the centre. Therefore, as the mass m loses an energy of $\mathrm{d}E$, it moves in towards the centre by dr. If $m = \dot{M}\mathrm{d}t$ is the small amount of mass that falls in, then $\mathrm{d}E = \mathrm{d}r\mathrm{G}M_{\mathrm{BH}}\dot{M}\mathrm{d}t/2r^2$. Here, the luminosity represents this radial transfer of energy, meaning $\mathrm{d}E/\mathrm{d}t = \mathrm{d}r\mathrm{G}M_{\mathrm{BH}}\dot{M}/2r^2$. Integrating from $r = r_{\mathrm{ISCO}}$ to ∞, we get

$$L = \frac{\mathrm{G}M_{\mathrm{BH}}\dot{M}_{\mathrm{BH}}}{2r_{\mathrm{ISCO}}}. \tag{3.35}$$

This relation has also been established in Pringle (1981), Frank et al. (2002), Carroll et al. (2017).

In the following we will estimate the accretion rate within the LMFP regime analytically. From **Eq. (3.35)**, we have

$$\dot{M} = \frac{2L_{\mathrm{emp}}r_{\mathrm{ISCO}}}{\mathrm{G}M_{\mathrm{BH}}}, \tag{3.36}$$

where we have used L_{emp} to indicate that we are modelling luminosity using empirical relations. The empirical relation for the conductivity κ_{lmfp} in the LMFP regime is (Koda et al. 2011, S. Yang et al. 2023a),

$$\kappa_{\mathrm{lmfp}} = \frac{3}{2}\beta\rho(r)\frac{H^2(r)}{t_{\mathrm{SIDM}}}, \tag{3.37}$$

where β is a free parameter that is calibrated against N-body simulations. It is expected that β is of order unity in the range 0.5 to 1.5 (Essig et al. 2019, S. Yang et al. 2023a). The above expression is the same as **Eq. (3.25)** but with the appropriate empirical coefficient. Substituting the above expression in **Eq. (3.23)**, we get

$$L_{\mathrm{emp}} = -m_\chi\frac{3}{2}\beta\rho(r)\frac{H^2(r)}{t_{\mathrm{SIDM}}}\frac{\partial\sigma_{1D}^2}{\partial r}. \tag{3.38}$$

In the innermost regions for $r \ll r_t$, the truncated density profile given in **Eq. (3.11)** can effectively be replaced by the spike profile given in **Eq. (3.1)**. Substituting Eqs. (3.1), (3.2) and (3.13) and $H \approx r$ (Shapiro et al. 2014) in the above equation, we get,

$$L_{\mathrm{emp}} = 6\pi\beta\rho_{\mathrm{sp}}^2\sigma_m\left(\frac{r}{r_{\mathrm{sp}}}\right)^{-2\gamma}\left(\frac{\mathrm{G}M_{\mathrm{BH}}r}{\gamma+1}\right)^{3/2}. \tag{3.39}$$

For $\gamma = 3/4$, we see that L_{emp} no longer depends on r. Correspondingly, the accretion rate from **Eq. (3.36)** becomes,

$$\dot{M} = \frac{576\pi\beta\rho_{\mathrm{sp}}^2\sigma_m\left(\mathrm{G}M_{\mathrm{BH}}r_{\mathrm{sp}}\right)^{3/2}}{7\sqrt{7}c^2}, \tag{3.40}$$

where c is the speed of light. Substituting the parameters from **Tab. 3.2**, we get

$$\dot{M} = \beta\, 3.8\,\mathrm{M}_\odot\,\mathrm{yr}^{-1}\frac{\sigma_m}{\mathrm{cm}^2\,\mathrm{g}^{-1}}. \tag{3.41}$$

The above equation has a form identical to the LMFP limit of **Eq. (3.27)**. Thus, we recover our fitted value $B^{-1} \approx 3.7\,\mathrm{M}_\odot\,\mathrm{yr}^{-1}\,\mathrm{cm}^{-2}\,\mathrm{g}$ using $\beta = 0.97$.

3.D Energy conservation

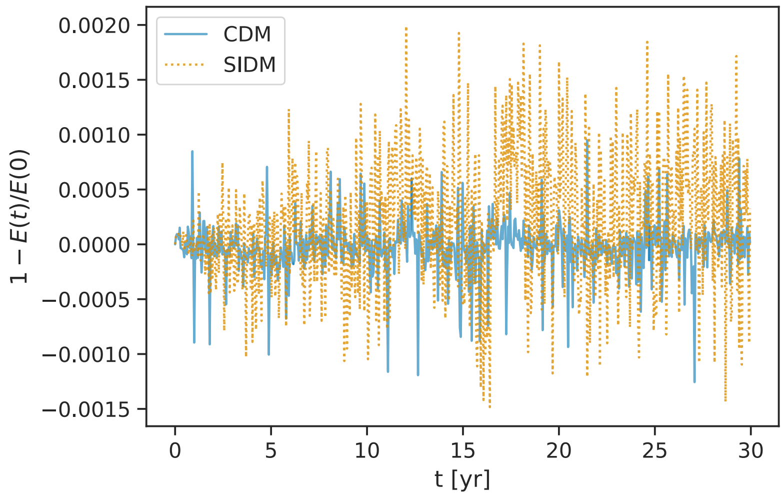

Figure 3.D1: Fractional energy change over time is plotted. Solid line corresponds to CDM, and dotted line corresponds to a SIDM simulation with $\sigma_m = 2.0\,\mathrm{cm}^2\,\mathrm{g}^{-1}$.

We verify our choice for the precision parameters by measuring how well the total energy is conserved in the simulations. For this test, we run a CDM and an SIDM simulation with $\sigma_m = 2.0\,\mathrm{cm}^2\,\mathrm{g}^{-1}$, and we do not remove particles that cross the r_{ISCO} of the SMBH. The parameters of the profile used in the simulation are given in **Tab. 3.2**, and the precision parameters in **Tab. 3.1**. We present the results in **Fig. 3.D1**, and we see that total energy is conserved to within 0.1% and 0.2% in the CDM and SIDM simulations respectively.

4 Dark matter spikes in the SMFP

This chapter is going to be submitted for publication.

4.1 Introduction

In the earlier chapter (**chapter 3**) it was shown that DM spikes are steady-state solutions using N-body simulations in the LMFP and IMFP regimes. Therefore, it is natural to wonder whether such solutions are possible in the SMFP. Shapiro et al. (2014) argue that in the SMFP, SIDM would behave like a Bondi gas with a steady-state density profile that scales like $r^{-3/2}$. The argument behind is that in the strong collisional limit, i.e. $\sigma_m \rightarrow \infty$, the collisional relaxation time $t_r \rightarrow 0$ mimics the Bondi gas limit. However, this still needs to be verified in simulations, since in the SMFP there is still some non-zero thermal conductivity. It is known that conducting Bondi gas, will lead deviations in the profiles and the accretion rate. In fact the accretion rate is suppressed due to conductivity (Gruzinov 1998, Johnson et al. 2007). To this end, the problem of SIDM spikes in SMFP needs to be setup with the appropriate conductivity.

4.2 Canonical Bondi accretion

The canonical Bondi problem (Bondi 1952) considers a spherically symmetric setup with non-conducting gas with zero angular momentum in a steady-state around a BH. The physical parameters of the setup are $(\rho_\infty, c_{\mathrm{s},\infty}, v_\infty, M_{\mathrm{BH}})$, i.e. density, sound speed, and radial velocity at infinity and the mass of the black hole. The density and sound speed are typically set to the properties of the interstellar medium (ISM) for a stellar BH, and v_∞ is assumed to be zero. The gas is also assumed to be a polytropic gas with the equation of state (EoS) $P = k\rho^\Gamma$. Here k is the polytropic constant that is set by the boundary conditions. $\Gamma = 1$ and $\Gamma = 5/3$ correspond to the isothermal and adiabatic-monatomic gas. Therefore, Bondi gas is a polytropic fluid that evolves under Euler equation and mass-continuity equation,

$$P = k\rho^\Gamma, \tag{4.1}$$

$$\frac{\partial \rho}{\partial t} + \nabla \cdot (\rho \boldsymbol{v}) = 0, \tag{4.2}$$

$$\frac{\partial \rho \boldsymbol{v}}{\partial t} + \nabla \cdot (\rho \boldsymbol{v}\boldsymbol{v} + P) = \rho \boldsymbol{g}. \tag{4.3}$$

here P is the pressure, $\boldsymbol{v}$ is the bulk velocity vector, $\boldsymbol{g}$ is the acceleration experienced by the fluid parcels. The time derivative terms are set to zero since steady-state solutions are sought. Since the problem is spherically symmetric, system of PDEs become the following ODEs.

$$P = k\rho^{\Gamma}, \tag{4.4}$$

$$\frac{\mathrm{d}(r^2\rho v_r)}{\mathrm{d}r} = 0, \tag{4.5}$$

$$v_r\frac{\mathrm{d}v_r}{\mathrm{d}r} + \frac{1}{\rho}\frac{\mathrm{d}P}{\mathrm{d}r} + \frac{GM_{\mathrm{BH}}}{r^2} = 0. \tag{4.6}$$

The Euler equation in this form can be integrated analytically to the Bernoulli equation. The problem with this approach is that it cannot be extended to accretion models which contains additional physics like angular momentum, conductivity, viscosity, radiation, magnetic fields etc. (Shakura et al. 1973, Lynden-Bell et al. 1974, Blandford et al. 1977, Narayan et al. 1994, Sharma et al. 2008, Yuan et al. 2014, Jiao et al. 2025, Ranjbar et al. 2025).

To understand the general characteristics of the ODE system, it is useful to recast it into the following form,

$$c_{\mathrm{s}}^2 = k\Gamma\rho^{\Gamma-1}, \tag{4.7}$$

$$r^2\rho v_r = \lambda, \tag{4.8}$$

$$\frac{1}{2}\left(\frac{v_r^2 - c_{\mathrm{s}}^2}{GM_{\mathrm{BH}} - 2c_{\mathrm{s}}^2 r}\right)\frac{1}{v_r^2}\frac{\mathrm{d}v_r^2}{\mathrm{d}r} + \frac{1}{r^2} = 0, \tag{4.9}$$

here λ is a constant proportional to the accretion rate $\dot{M}$, c_{s} is the speed of sound. Note that the quantities $v_r, c_{\mathrm{s}}, \rho, P$ are all functions of r. In the above equations there could potentially be a singularity at $r = GM_{\mathrm{BH}}/2c_{\mathrm{s}}^2$. To regularize the ODE it is required that also the numerator vanishes at the same r, i.e. $v_r^2 = c_{\mathrm{s}}^2$. This special radius is the sonic radius. Therefore, care must be taken when numerically integrating the ODE. Moreover, the location of the singularity depends on the solution c_s making it more complicated. There are four unknown variables $\lambda, \rho, v_r, c_{\mathrm{s}}$ and only three equations. Therefore, it is common to treat the parameter λ a free parameter. There are 6 family of solutions possible to the system of equations (Holzer et al. 1970, Shu 1992, Clarke et al. 2007, Ray et al. 2007). Thus depending on the choice for λ, the flow can be subsonic, supersonic at all r, or it can be transonic where the flow transitions from subsonic to supersonic at the sonic radius. The accretion is the largest for the transonic solutions, and it is also the solution that minimizes the total energy of the system (Bondi 1952). Furthermore, perturbative analysis showed that subsonic solutions are equally stable as the transonic ones (Garlick 1979, Keto 2020). However, as verified as a part of this thesis, the profiles tend to transonic solutions for a variety of initial conditions.

4.2.1 Bondi solutions

Since the accretion rate parameter λ can be chosen arbitrarily there infinitely many solutions. The transonic solution is only the solution that can be uniquely determined, and therefore this parameter could be thought of as an Eigen value of the problem. In the transonic regime, the accretion rate, along with the Eigen value λ_B can be shown to be (Aguayo-Ortiz et al. 2021),

$$\dot{M}_B = 4\pi\lambda_B(GM_{\rm BH})^2\rho_\infty c_{\rm s,\infty}^{-3}, \tag{4.10}$$

$$\lambda_B = \frac{1}{4}\left(\frac{2}{5-3\Gamma}\right)^{\frac{5-3\Gamma}{2(\Gamma-1)}}. \tag{4.11}$$

The full profile in the same regime can be obtained semi-analytically, and scaling in the innermost region is given as,

$$v \sim \sqrt{\frac{GM_{\rm BH}}{r}}, \quad r \ll r_B \tag{4.12}$$

$$\rho \sim r^{-3/2}, \quad r \ll r_B \tag{4.13}$$

The characteristic length scale r_B goes by the name Bondi radius, and is defined as $r_B := GM_{\rm BH}/c_{\rm s,\infty}^2$. The above profiles in these limits can be read from the fact that near the BH, the radial infall velocity must be the free-fall velocity. Therefore, from mass-continuity equation it can be deduced that the density profile should have such a scaling.

4.3 SIDM spike in SMFP

SIDM in SMFP has Kn $\ll 1$, therefore it will be in the hydrodynamic regime. It is possible to draw parallels between Bondi profiles and dark matter spike profile. The DM spike parameters $\sigma_0, \rho_{\rm sp}, r_{\rm sp}$ can be mapped to the Bondi profile parameters $c_{\rm s,\infty}$, ρ_∞, r_B respectively. In addition to the fluid equations given in **Eqs. (4.2)** to **(4.3)**, heat conductivity requires and additional corresponding to the energy conservation,

$$\frac{\partial E}{\partial t} + \nabla \cdot [(E+P)\boldsymbol{v} + \boldsymbol{q}] = \rho\boldsymbol{v}\cdot\boldsymbol{g}, \tag{4.14}$$

here $\boldsymbol{q}$ is the heat flux vector, E is the total energy density,

$$E = e + \frac{1}{2}\rho v^2, \tag{4.15}$$

where e is the internal energy density. Note that the RHS of the fluid equations contain the source terms due to gravity explicitly, and the geometric source terms are implicit here.

4.3.1 Simulation setup

To simulate the SMFP limit of SIDM we use the GRMHD code `athena++` (Stone et al. 2020), and SIDM's SMFP conductivity has been added to the code. As a test for the setup, we simulate first the canonical Bondi problem with no heat conduction. All the simulations performed can be classified into two categories, one based on the choice of BCs and the other based on the choice of initial conditions. There are two possible BCs, open BCs and fixed BC at r_∞. For the initial conditions there are two possibilities: *(i)* starting with a radially uniform density, temperature, and velocity profiles. The other being starting the analytical solutions of the canonical Bondi problem. Independent of the choice BC, or the IC the system tends towards the transonic analytical solution.

σ_m [$\mathrm{cm^2\,g^{-1}}$]	Kn	ρ_∞ [$\mathrm{g\,cm^{-3}}$]	$c_{s,\infty}$ [$\mathrm{km\,s^{-1}}$]	$M_{\rm BH}$ [$\mathrm{M_\odot}$]
$5 \cdot 10^{-6}$	0.04	10^{-10}	10	1
10^{-5}	0.02	10^{-10}	10	1
$3 \cdot 10^{-5}$	0.007	10^{-10}	10	1
10^{-4}	0.002	10^{-10}	10	1

Table 4.1: Physical parameters of the simulation. First two columns are the cross-section and the largest Knudsen number within the radial range simulated. Third, and fourth columns are the density and the sound speed of the ambient medium or core. Final column is the black hole mass.

In `athena++`the heat conduction is a part of the diffusion processes module, and heat fluxes are calculated as,

$$q_{\rm code} = -\kappa_{\rm code}\, \rho \frac{d}{dr}\left(\frac{P}{\rho}\right). \tag{4.16}$$

Physically, it is required that the fluxes be,

$$q_{\rm SMFP} = -\kappa_{\rm SMFP} \frac{d}{dr}\left(\frac{P}{\rho}\frac{m_\chi}{k_B}\right). \tag{4.17}$$

We know that in SMFP,

$$\kappa_{\rm SMFP} = \frac{2.1}{\sigma} k_B \sigma_{1D}. \tag{4.18}$$

Since DM behaves like a fluid, we assume it to be an adiabatic fluid with an adiabatic index $\gamma = 5/3$. For such a fluid the SMFP conductivity can be recast in terms of the primitive variables of athena++ as,

$$\kappa_{\text{SMFP}} = \frac{2.1}{\sigma} k_B \sqrt{\frac{P}{\rho}}. \tag{4.19}$$

Comparing **Eq. (4.16)** with **Eq. (4.17)**, we see that,

$$\kappa_{\text{code}} = \frac{2.1}{\sigma/m_\chi} \frac{P^{1/2}}{\rho^{3/2}}. \tag{4.20}$$

The simulations that are run in the radial range $10^{-2} r_B < r < 10^3 r_B$, use the units where $M_{\text{BH}} = 1, \rho_\infty = 1, c_{\text{s},\infty} = 1$. While the simulations that are run close to the BH, i.e. in the range $r_{\text{ISCO}} < r < 10^3 r_{\text{ISCO}}$, the units are $c = 1, R_s = 1, \rho_\infty = 1$. The time step criterion for the conduction module is, $\Delta t_{\text{cond}}(r) = C\Delta r^2/\kappa_{\text{code}}(r)$. Similarly, time step criterion corresponding to gravitational acceleration (g) is $\Delta t_{\text{gra}}(r) = C\Delta r/g(r)$. In both of these cases $C \in [0.1, 1.0]$.

4.4 Results

Numerical setup is first validated by reproducing the canonical Bondi solutions in athena++. In **Fig. 4.4.1**, the evolution of the density profile and radial velocity profile are shown. The radial range for the simulations covers both $r \ll r_B$ and $r \gg r_B$, and it can be seen that the profile on a timescale of $t_B := r_B/c_{\text{s},\infty}$ develops the right shape for the profile. It can also be seen that $r \ll r_B$, the density profile scaling is $r^{-3/2}$, while radial velocity scales like $r^{-1/2}$ matching the expectations from theory. Similarly, for $r \gg r_B$, $\rho \sim \rho_\infty$, and $v/c_{\text{s},\infty} \ll 1$. Further to verify the stability of the setup, a simulation is run with initial conditions that follows the numerical solutions, and the results are displayed in **Fig. 4.4.2**.

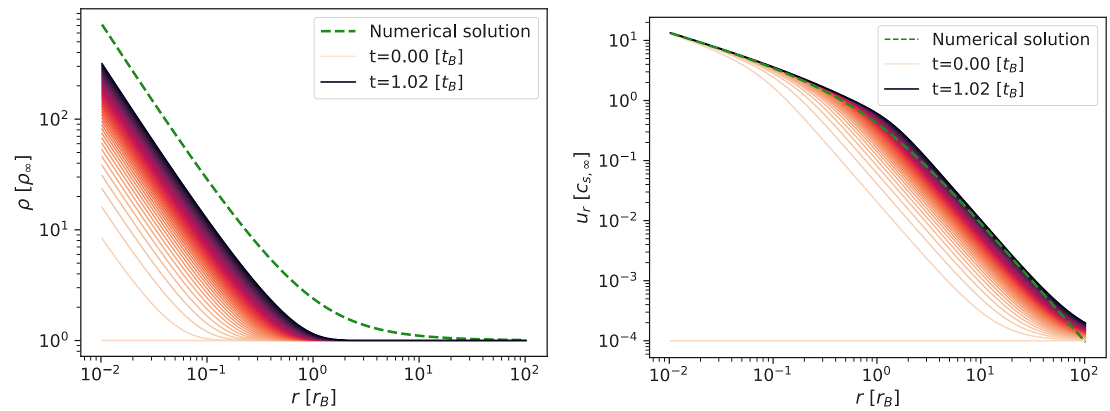

Figure 4.4.1: Evolution of $\rho(r)$, $v(r)$ starting from a uniform density, radial velocity, temperature profile. Simulation truncated before steady-state is reached.

In addition, the accretion rate from the simulations is computed from the simulation data as the mean of $r^2\rho v$ over different radial bins i,

$$\frac{\dot{M}(t)}{\dot{M}_B} = \frac{\sum_i r_i^2(t)\rho_i(t)v_i(t)}{\sum_i r_i^2(t=0)\rho_i(t=0)v_i(t=0)}. \tag{4.21}$$

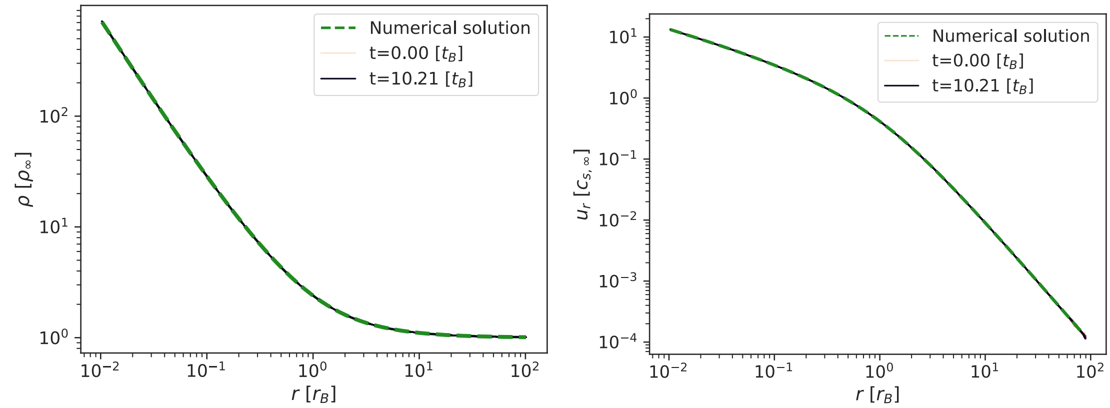

Figure 4.4.2: Evolution of $\rho(r)$, $v(r)$ starting from the numerical solutions for density, radial velocity, temperature profile. Since the initial conditions are that of the steady-state solutions, the profiles are observed to be stable.

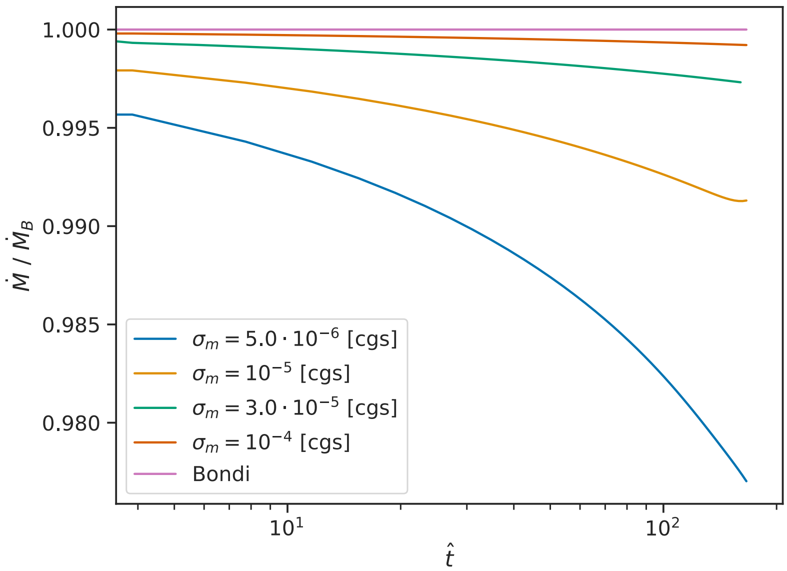

Figure 4.4.3: Dimensionless accretion rate normalized to Bondi rate vs. dimensionless time normalized to dynamical timescale at the middle of the fluid domain.

Since the denominator is evaluated at $t = 0$, it corresponds to the numerical solutions. In addition, as a final check, the standard deviation of the accretion rate across radial bins is computed and is at the most 1% in all the performed simulations. For the canonical Bondi profile, $\dot{M}(t) \approx \dot{M}_B$.

The results for the accretion-rate as function of cross-section is given in **Fig. 4.4.3**. The accretion rate is observed to decrease with decreasing cross-section or increasing conduction and this is in accordance with the findings in Gruzinov (1998), Tanaka et al. (2006), Faghei (2012). Physically this is due to the fact that with conductivity energy flows outwards and increasing the temperature. To understand this better consider the case for $\Gamma = 5/3$, in the canonical Bondi problem r_s is at the BH's surface. Increasing the temperature in the outer parts implies that the sonic radius will move inwards, therefore the accretion rate will become smaller in comparison at the surface of the BH. Similarly, density profile cores, leading to reduction in density at the surface of the BH. Cumulatively, this reduces the accretion rate.

4.5 Comparison of accretion rates

In this section accretion rates of different types of accretion onto the BH are compared. On one end there is the collisional limit corresponding to Bondi, and the other being collisionless particles like CDM.

4.5.1 Collisionless case

In **section 3.5**, the accretion rate was calculated numerically given the spike density profile. It was also argued that in realistic CDM spikes the loss-cone will be accreted during the formation of the spike. Therefore, in this subsection a conservative estimate for accretion rate for a generic collisionless particle that is in steady-state will be calculated. That is, a conservative estimate for the accretion rate after the formation of spike. Since there is only gravitational scattering responsible for repopulating the phase space, one obtains $t_{\rm rel} \gg t_{\rm dyn}$. Hence, the orbit-averaged phase space distribution is preferred (Binney et al. 2008, Merritt 2013). The mass in the interval $\mathrm{d}\mathcal{E}$, $\mathrm{d}J$ around the point $\mathcal{E}, J$ can be written as,

$$\mathrm{d}M_{\rm tot}(\mathcal{E}, J)\, \mathrm{d}\mathcal{E}\, \mathrm{d}J \ \sim J\, P(\mathcal{E})\, f(\mathcal{E})\, \mathrm{d}\mathcal{E}\, \mathrm{d}J. \tag{4.22}$$

In the above equation J is the magnitude of angular momentum and $\mathcal{E} = -E = GM_{\rm BH}/r - v^2/2$, $P(\mathcal{E})$ is orbital period, $f(\mathcal{E})$ is the phase space density. Therefore, the mass inside the loss-cone is,

$$M^- \sim \int \int_0^{J_{\rm min}} L\, P(\mathcal{E})\, f(\mathcal{E})\, \mathrm{d}\mathcal{E}\, \mathrm{d}J, \tag{4.23}$$

$$\sim \int J_{\rm min}^2\, P(\mathcal{E})\, f(\mathcal{E})\, \mathrm{d}\mathcal{E}. \tag{4.24}$$

The "-" superscript denotes the fact that the particles are in the loss-cone. The function $f(\mathcal{E})$ for a spike of the form $\rho(r) = \rho_\infty (r/r_B)^{-\gamma}$ can be calculated using Eddington inversion (see **App. 3.B** for method details). The result is,

$$f(\mathcal{E}) = \frac{\rho_\infty\, c_{s,\infty}^{-2\gamma}\, \mathcal{E}^{\gamma-\frac{3}{2}}\, \Gamma(\gamma+1)}{2\sqrt{2}\pi^{3/2}\Gamma\left(\gamma-\frac{1}{2}\right)}, \qquad \gamma > 1 \tag{4.25}$$

here $\Gamma(x)$ is the Euler Gamma function. The period as function of $\mathcal{E}$ is,

$$P(\mathcal{E}) \sim GM_{\rm BH}\mathcal{E}^{-3/2}. \tag{4.26}$$

Performing the integration in **Eq. (4.24)** using the above given $f(\mathcal{E})$ along with $P(\mathcal{E})$,

$$M^- \sim J_{\rm min}^2\, GM_{\rm BH}\, \rho_\infty\, c_{s,\infty}^{-2\gamma} \left[\mathcal{E}^{\gamma-2}\right]_\infty^{c_{s,\infty}^2}. \tag{4.27}$$

The limits on the integral follow from the following arguments. For a bound system, the largest possible energy for any particle should be zero. However, it will make the calculations significantly simpler by considering the marginally bound particle at r_B, that is $\mathcal{E} = GM_{\rm BH}/r_B = c_{s,\infty}^2$. Similarly, the lowest possible energy is $E = -\infty \implies \mathcal{E} = \infty$. The evaluated integral will converge only for $\gamma < 2$, to extend it to $\gamma > 2$ it is required that the lower limit needs to be truncated at a finite value. One possibility is to set it to the potential at the $r_{\rm ISCO}$. But, to estimate the accretion rate in units of $\dot{M}_B$, it will be useful to keep the limit at ∞. The loss-cone mass becomes,

$$M^- \sim J_{\rm min}^2\, GM_{\rm BH}\, \rho_\infty\, c_{s,\infty}^{-4}. \tag{4.28}$$

For conservative estimate, accretion rate can be approximated to be M^- over the orbital period for a particle at r_B,

$$t_{\rm orb}(r_B) \sim \left(\frac{r_B^3}{GM_{\rm BH}}\right)^{1/2} = c_{s,\infty}^{-1} r_B.$$

In addition, from **section 3.5**, $J_{\rm min}^2 \sim GM_{\rm BH} r_{\rm ISCO}$. Therefore, the accretion rate for collisionless particles can be written as,

$$\dot{M}_{\rm ColLess} = \frac{M^-}{t_{\rm orb}(r_B)} \sim (GM_{\rm BH})^2\, \rho_\infty\, c_{s,\infty}^{-3} \left(\frac{r_{\rm ISCO}}{r_B}\right) \tag{4.29}$$

$$\dot{M}_{\rm ColLess} \sim \dot{M}_B \left(\frac{r_{\rm ISCO}}{r_B}\right). \tag{4.30}$$

For the SMBH of $M_{\rm BH} \sim 10^{10}\,{\rm M}_\odot$, $r_B \sim 1\,{\rm kpc}$, $r_{\rm ISCO} \sim 10^{-6}\,{\rm kpc}$. Therefore, the accretion rate is the collisionless case is suppressed by several orders of magnitude. The suppression can also be understood in terms of radial infall velocity. For the reminder of this section, the calculations assume speed of light $c = 1$. If there is some steady state collisionless accretion, then $\dot{M} \sim r_{\rm ISCO}^2 \rho(r_{\rm ISCO}) v_r$, therefore,

$$r_{\rm ISCO}^2 \rho(r_{\rm ISCO}) v_r(r_{\rm ISCO}) \sim \dot{M}_B \frac{r_{\rm ISCO}}{r_B} \tag{4.31}$$

$$r_{\rm ISCO}^2 \rho_\infty (r_{\rm ISCO}/r_B)^{-\gamma} v_r(r_{\rm ISCO}) \sim (GM_{\rm BH})^2 \rho_\infty c_{s,\infty}^{-3} \frac{r_{\rm ISCO}}{r_B} \tag{4.32}$$

$$\implies v_r(r_{\rm ISCO}) \sim c_{s,\infty}^{-1+2\gamma}. \tag{4.33}$$

Since the analytic results are valid only for $\gamma > 1$, it is clear that $v_r(r_{\mathrm{ISCO}}) \ll 1$ for collisionless particles, while for Bondi gas from **Eq. (4.13)**, it is $v_r \lesssim 1$.

4.5.2 SIDM in LMFP

In **App. 3.C**, the expression for accretion rate of SIDM due to heat conductivity was calculated using the arguments that $\dot{M} \propto L$. Here L is the luminosity due to heat conduction. The scaling of the accretion rate with respect to the physical parameters of the problem can be written from **Eq. (3.40)** as,

$$\dot{M}_{\mathrm{LMFP}} \sim \rho_\infty^2 (G M_{\mathrm{BH}})^3 c_{\mathrm{s},\infty}^{-3} \sigma_m \tag{4.34}$$

$$\sim \dot{M}_B r_{\mathrm{ISCO}} \sigma_m \rho_\infty. \tag{4.35}$$

To make it comparable to the accretion rate in the collisionless case, further scaling relations in terms of other parameters can be written down from the above equation as,

$$\dot{M}_{\mathrm{LMFP}} \sim \dot{M}_B r_{\mathrm{ISCO}} \sigma_m \rho_\infty \tag{4.36}$$

$$\sim \dot{M}_B \left(\frac{r_{\mathrm{ISCO}}}{r_B} \right) \sigma_m \rho_\infty r_B \tag{4.37}$$

$$\sim \dot{M}_{\mathrm{ColLess}} \sigma_m \rho_\infty r_B. \tag{4.38}$$

Alternatively, it can also be written as in terms of the mean free path of SIDM at the spike radius ($\lambda_{\mathrm{SIDM,B}}$),

$$\dot{M}_{\mathrm{LMFP}} \sim \dot{M}_B \left(\frac{r_{\mathrm{ISCO}}}{\lambda_{\mathrm{SIDM,B}}} \right). \tag{4.39}$$

Therefore, for a typical SIDM spike around $M_{\mathrm{BH}} \sim 10^{10}\,\mathrm{M}_\odot$, $r_B \sim 1\,\mathrm{kpc}, \rho_\infty \sim 20\,\mathrm{M}_\odot\,\mathrm{pc}^{-3}$, the accretion rate for $\sigma_m \sim \mathrm{cm}^2\,\mathrm{g}^{-1}$ is $\dot{M}_{\mathrm{LMFP}} \sim \dot{M}_{\mathrm{ColLess}} \times 4$. This agrees with the findings from the earlier chapter.

4.6 Discussion

In this section, the findings of this chapter are summarized and important aspects of the problem are discussed.

- Accretion rate as a function of collisionality or Knudsen number is summarized in **Fig. 4.6.1**. The figure also shows a crude classification of the different regimes by highlighting them in different coloured blocks. In the collisionless limit the accretion rate purely stems from repopulation of the loss-cone due to gravitational relaxation, and a conservative estimate for the accretion rate was derived in **section 4.5.1**. This region is marked gray in the figure. In LMFP and IMFP the accretion rate gains an additional contribution from heat conduction. The LMFP regime is highlighted in red, while the IMFP where N-body simulations have been performed is highlighted in green. We find from simulations that conduction's contribution is at a maximum around Kn ~ 1.

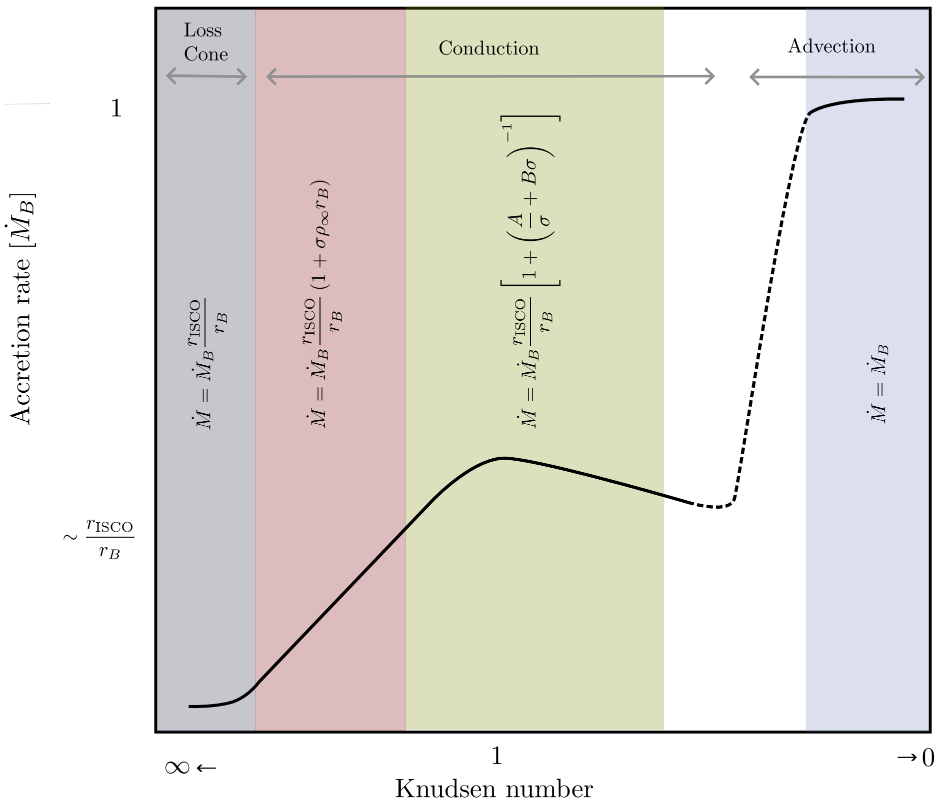

Figure 4.6.1: A schematic representation of the accretion rate in units of Bondi accretion rate as function of Knudsen number. Different coloured blocks correspond to different regimes where the leading contributor to the accretion rate stems from different physical mechanisms. The gray coloured region corresponds to the collisionless limit where accretion rates derives primarily from the loss-cone repopulation. Red corresponds to LMFP accretion where heat conductivity is the leading order effect followed by loss-cone repopulation from gravitational relaxation. Green corresponds to the region of IMFP where conduction is the leading order effect, and represents the region of IMFP that has been simulated in N-body simulations. Finally, in the collisional limit, advection is the main driver of accretion. The dashed line denotes the region where neither fluid nor N-body simulations have been performed.

Eventually, for decreasing Kn number, bulk flow and advection starts contributing, and we expect that the accretion rate reaches the Bondi rate for $\mathrm{Kn}(r_B) \ll 1$. This transition value for the Knudsen number can be estimated from the ratio of fluxes of energy due to advection and conduction at the

Bondi radius,

$$L_{\text{adv}} \sim \rho_\infty c_{\text{s},\infty} \frac{GM}{r_B} \tag{4.40}$$

$$L_{\text{cond}} \sim \kappa_{\text{SMFP}} \nabla T \sim \kappa \frac{c_{\text{s},\infty}^2}{r_B} \sim \frac{c_{\text{s},\infty}^3}{\sigma_m r_B} \tag{4.41}$$

Note that in the estimation of L_{adv}, we have assumed that $v_r(r_B) \sim c_{\text{s},\infty}$. Therefore, the ratio of these fluxes becomes,

$$\frac{L_{\text{adv}}}{L_{\text{cond}}} \sim \rho_\infty r_B \sigma_m = \frac{r_B}{\lambda_{\text{SIDM,B}}} = \frac{1}{\text{Kn}(r_B)}. \tag{4.42}$$

Therefore, $L_{\text{adv}} \gg L_{\text{cond}}$ requires that $\text{Kn}(r_B) \ll 1$. The above claim can be made more robust by letting $v_r(r_B) = \alpha c_{\text{s},\infty}$ for some constant $\alpha \in [r_{\text{ISCO}}/r_B, 1]$. The scaling of the fluxes still remains to be inversely proportional to Kn. This transitional region cannot be simulated using N-body since the required mass-resolution would make it computationally impossible, and at the same time hydro simulations cannot be used since it inherently assumes that $\text{Kn} \ll 1$. Therefore, alternative methods like Direct Simulation Monte Carlo (DSMC) or lattice-Boltzmann method need to used.

- In the collisionless limit, the Boltzmann equation cannot be truncated to fluid equations without making strong assumptions about the profile. Therefore, no unique analytic solutions exist for the steady state profile. In addition, due to the lack of collisions, there is no local equilibrium distribution. However, from Jeans theorem (Jeans 1915) a global $f(\mathcal{E})$ that describes the phase-space can be written down for spherically symmetric system with isotropic velocity distribution. Therefore, accretion can only happen due to loss-cone accretion which can be determined from this global $f(\mathcal{E})$.

- In the collisional limit, the gas tends towards local Maxwellian distribution. Thus it is possible to attribute a local temperature $T(\boldsymbol{x})$, this allows us to close the Boltzmann hierarchy. Therefore as shown in **Eqs. (4.7)** to **(4.9)**, there are equal numbers of unknown and knowns leading to a unique transonic analytic solution. The thermalization over small scales in the strong collisional limit, can be seen immediately from the relaxation time approximation, where the collision operator is approximated to,

$$C[f] \approx \frac{f - f_{\text{eq}}}{t_{\text{col}}}. \tag{4.43}$$

Here, f is the local phase-space distribution, and f_{eq} is the local Maxwellian phase-space distribution characterized by the kinetic temperature $T \sim c_\text{s}^2$, t_{col} is the collisional timescale set by the scattering cross-section. This approximation is originally due to Bhatnagar et al. (1954). Therefore, in this Bondi limit, SIDM effectively thermalizes over small scales leading to an identical behaviour to gases, and thus displays attributes such as bulk flow.

- A setup for CDM, where all the particles are radially shot to the centre, can in fact be a solution to $\mathrm{d}f/\mathrm{d}t = 0$, and have accretion rates as large as $\dot{M}_B$. However such a setup is artificial for a realistic CDM spike. The conflict is the following, if CDM spike forms via adiabatic contraction, then the initial distribution $f_i(\mathcal{E}_i)$ of the host halo that undergoes contraction must be related to the final $f_f(\mathcal{E}_f)$ of the spike via adiabatic invariants. Therefore, f is always a function only of $\mathcal{E}$ as adiabatic contraction does not introduce additional dependencies. Hence, the radial bulk flow can be calculated for any $f(\mathcal{E})$ as,

$$\langle v_r \rangle = \int \mathrm{d}^3\boldsymbol{x}\, \mathrm{d}^3\boldsymbol{v}\; v_r\; f(\mathcal{E}) = 0. \tag{4.44}$$

The above integral is exactly zero since $\mathcal{E}$ is an even function of v_r. This clearly demonstrates that for CDM be it spike or host NFW profile, the only possible bulk flow arises due to repopulating of the loss-cone, and it has been shown to be negligible in **section 4.5.1**.

- Gravothermal collapse can lead to the formation of a seed BH as predicted by W.-X. Feng et al. (2022), Gu et al. (2026). The initial SMFP core formed via gravothermal collapse typically has negligible angular momentum, as a typical host is assumed to have zero total angular momentum. The BH seed will then be surrounded by a SMFP core without angular momentum. Hence, the accretion will happen approximately at $\dot{M}_B$. Therefore, the SMFP core will be depleted on a timescale $t_{\mathrm{depl}} := M(r < r_B)/\dot{M}_B \sim r_B/c_{\mathrm{s},\infty}$. Note that for a Bondi gas a spike inside r_B forms from a uniform core on the same timescale. In this physical setup, if the seed mass is small, the t_{depl} can be very large and accretion proceeds slowly.. Slow accretion is due to the fact that the Bondi accretion rate scales quadratically with the M_{BH}, and for small M_{BH} this can be small. On the other hand if SIDM spikes in SMFP were to exist in the centres of galaxies, then the spike will be depleted on timescale that is much smaller than the Hubble timescale. For example, for a SMBH of $M_{\mathrm{BH}} \sim 10^{10}\,\mathrm{M}_\odot$ as considered in the earlier chapter (see **Tab. 3.2**), $t_{\mathrm{depl}} \approx 10^{-4} t_{\mathrm{Hubble}}$.
- An alternative approach that is worth highlighting to understand the effects of relaxation and scattering is to use the Fokker-Planck operator to approximate the collision operator. This approach is common in understanding the loss-cone dynamics of stars (Lightman et al. 1977, Magorrian et al. 1999, Alexander 2005, Merritt 2013). It is well known that there are two regimes in loss-cone dynamics characterized by $q \sim t_{\mathrm{rel}}/t_{\mathrm{orb}}$. The $q \gg 1$ is called the pin-hole regime, while $q \ll 1$ is called the diffusive regime. The flux of particles into the loss-cone in pin-hole regime is typically several orders of magnitude larger than the one from diffusive regime. In case of stars, the t_{rel} is due to gravitational scattering. However, the result should hold independent of the nature of the relaxation process. Therefore, it is only natural that DM particles undergoing SIDM scattering exhibit a similar limiting behaviour.

4.7 Conclusions

In this chapter, the effects of thermal conduction on SIDM spikes in the SMFP regime have been investigated. There are some caveats in the modelling, the first and foremost is that all general relativistic effects are neglected. This part can be easily achieved by letting the particles travel on geodesics of the metric of the BH in athena++, or by using SPH based codes like (Rosswog et al. 2024). The effects of viscosity are neglected in our analysis, however since Bondi like flow has non-negligible bulk-flow, bulk viscosity needs to be accounted for. Simulations have been run only for a total duration such that the numerical integration errors remain small. To determine the exact final steady-state profiles, the system of 1D ODE equations needs to be integrated numerically using relaxation methods (Press et al. 2002). Therefore, an exact scaling relation for the final steady-state density and velocity profiles as a function of cross-section is not provided. Moreover, the conductivity that was simulated corresponds to the velocity-independent cross-section. On the other hand, due to observations, velocity-dependent cross-sections are better motivated. This is not too hard to implement as an extension to our current setup in athena++. In summary,

- The first non-relativistic fluid simulations of SIDM spike profile in the SMFP regime including the effects of heat conduction have been performed.
- It is found from the simulations that for $\mathrm{Kn}(r_B) \ll 1$, the system is effectively Bondi-like with slightly lowered accretion rates. The true final steady-state can be determined only with numerical integration and is left for future work. In the intermediate regime where both N-body and hydro limits fail, either DSMC or Lattice Boltzmann methods can be employed to faithfully represent the microphysics on macro scales.
- Quantitative arguments have been used to show that the effects of advection start to dominate over conduction in the regime $\mathrm{Kn}(r_B) \ll 1$.
- Scaling relations that relate the accretion rate in the collisionless, LMFP, IMFP regimes with the Bondi accretion rate have been derived. The accretion rates in the collisionless, LMFP and IMFP are suppressed by the ratio r_{ISCO}/r_B when compared to the Bondi accretion rate. Numerically, this is typically several orders of magnitude. In addition, using Knudsen number, SIDM regimes have been schematically categorized into regions where different physical effects dominate the accretion rate.

Appendix

4.A Energy Equation

In this appendix, the gravothermal energy equation of SIDM is derived from the general energy conservation equation for fluids. The total energy equation for a conducting fluid is,

$$\frac{\partial E}{\partial t} + \nabla \cdot [(E + P)\boldsymbol{v}] = -\nabla \cdot \boldsymbol{q}. \tag{4.45}$$

where $E = \rho\left(\frac{1}{2}v^2 + e\right)$ is total energy density, e is specific internal energy, P is pressure, and $\boldsymbol{q}$ is heat flux. Taking the dot product of the momentum equation **Eq. (4.3)** with $\boldsymbol{v}$ results in the kinetic energy equation, i.e. ,

$$\frac{\partial}{\partial t}\left(\rho\frac{1}{2}v^2\right) + \nabla\cdot\left[\left(\rho\frac{1}{2}v^2 + P\right)\boldsymbol{v}\right] = \rho\boldsymbol{v}\cdot\boldsymbol{g}. \tag{4.46}$$

Taking the difference between the total energy equation and the kinetic energy equation, we get,

$$e\left(\frac{\partial\rho}{\partial t} + \boldsymbol{v}\cdot\nabla\rho + \rho\nabla\cdot\boldsymbol{v}\right) + \rho\left(\frac{\partial e}{\partial t} + \boldsymbol{v}\cdot\nabla e\right) + P\nabla\cdot\boldsymbol{v} \quad = \quad -\nabla\cdot\boldsymbol{q}.$$

Due to continuity equation the sum inside the first bracket is zero, and using the definition of material derivative, we get,

$$\rho\frac{De}{Dt} + P\nabla\cdot\boldsymbol{v} = -\nabla\cdot\boldsymbol{q}. \tag{4.47}$$

To proceed further consider the following derivative,

$$\frac{D}{Dt}\left(\frac{1}{\rho}\right) = -\frac{1}{\rho^2}\frac{D\rho}{Dt} = \frac{1}{\rho}\nabla\cdot\boldsymbol{v},$$

where we have use continuity equation in the final equality. Using this, the energy equation can be written as,

$$\rho\frac{De}{Dt} + P\rho\frac{D}{Dt}\left(\frac{1}{\rho}\right) = -\nabla\cdot\boldsymbol{q}. \tag{4.48}$$

For SIDM halo with isotropic velocity dispersion, we have $e = \frac{3}{2}\sigma_{\mathrm{1D}}^2$, $P = \rho\sigma_{\mathrm{1D}}^2$. Thus, the energy equation in spherical coordinates become,

$$\frac{D}{Dt}\left(\frac{3}{2}\sigma_{\mathrm{1D}}^2\right) + P\frac{D}{Dt}\left(\frac{1}{\rho}\right) = -\frac{1}{\rho r^2}\frac{\partial}{\partial r}(r^2 q). \tag{4.49}$$

The above equation can be cast into the standard form with the definition, $L := -4\pi r^2\boldsymbol{q} = 4\pi r^2\kappa\frac{\mathrm{d}T}{\mathrm{d}r}$

$$4\pi\rho r^2\left[\frac{D}{Dt}\left(\frac{3}{2}\sigma_{\mathrm{1D}}^2\right) + P\frac{D}{Dt}\left(\frac{1}{\rho}\right)\right] = \frac{\partial L}{\partial r}. \tag{4.50}$$

5 Conclusion and Outlook

In this final chapter the main results of this thesis are summarized, and then an outlook on possible follow-up research related to the physics of SIDM is presented.

Astrophysical phenomenology of DM has become ever more interesting for the community for different reasons : *(i)* the missing evidence for DM from laboratory searches, and that the allowed parameter space for classical WIMPs is narrowed down at phenomenal pace. *(ii)* the surge of challenges for ΛCDM both at high redshifts and low redshifts at small scales demands investigations beyond ΛCDM. For the first mentioned problem a natural solution has been to consider models of DM beyond the standard WIMPs, and many of these extensions exhibit self-interactions. For the second problem, SIDM have been also shown to be promising candidates. Thus, the last decade has seen substantial progress in understanding the astrophysical phenomenology of SIDM through both observations, and novel modelling techniques. In this thesis, we contribute to this effort by studying merging of galaxy clusters with self-interactions, and perform the first N-body and fluid simulations of SIDM around black holes.

In the first publication presented in **chapter 2**, we chose to study the effects of frequent and rare-isotropic self-interactions with a v^{-4} velocity dependence. We find that the degeneracy in the evolution of isolated haloes for models of self-interactions is broken in galaxy cluster mergers. This was demonstrated by matching the cross-section parameters of frequent and rare-isotropic by simulating isolated DM haloes. We further prove that the ratio of matched momentum transfer cross-sections for these limiting cases of self-interactions is 2/3. We also successfully extended the constraints on velocity independent cross-section to the parameter space of velocity dependent cross-section, and performed merger simulations at the upper limits. Our merger simulations indicate that the offsets are approximately $\mathcal{O}(1)$ kpc at the first pericentre passage. Moreover, the offsets have been observed to grow with time, and they become approximately $\mathcal{O}(10)$ kpc after the third pericentre passage. The late stage offset is also seen to be sensitive the cross-section parameters. Thus, in contrary to common expectations this shows that later stages of mergers are more constraining than early stages. To further the interest in this finding observations find a median offset of 10 kpc in relaxed galaxy clusters. We report that this finding hints at investigating this further in the context of cosmological simulations with star formation, AGN feedback, and other subgrid physics.

In the second publication presented in **chapter 3**, we present the results of the first ever N-body simulations of DM spikes around SMBHs in the LMFP and IMFP regime. The simulations are performed only up to a cross-section that can be faithfully simulated at reasonable mass resolution. We show that the spike density profile converges to a spike index of $\gamma = 3/4$ independent of the choice of the initial slope of the profile highlighting that steady-state profiles do exist for SIDM in these regimes. In addition, this demonstrates that DM spike formation is a more robust prediction in SIDM than in CDM. The accretion rate in addition to the loss-cone accretion has an additional contribution due to conduction. We observe that in IMFP, the accretion rates max out at a Kn ~ 1, and conduction is suppressed for smaller and larger Kn. In addition, we also provided the first ever calibration of the empirical heat conduction parameter β in these scales. Finally, we delineate a region in the parameter space of the spike profile parameters where super-Eddington accretion is possible.

In **chapter 4**, we ran simulations of SIDM spike in the SMFP limit using hydrodynamic simulations. This chapter will be submitted for publication. We present the results of the first ever 1D hydro simulation of fluid with heat conductivity following the SMFP prescription. We find a mild but consistent reduction in the accretion rates of SIDM in this limit. Furthermore, we derive scaling relations for accretion rate across different regimes in collisionality in terms of the Bondi accretion rate. We show that accretion is suppressed by $r_{\rm ISCO}/r_B$ for accretion in LMFP and at the beginning of IMFP. The variation of accretion rate with Kn is sketched, and quantitatively we show that in the limit Kn $\ll 1$, advection starts to become the leading order contributor to accretion. With these findings, we speculate that a SMBH within a SMFP core, will deplete the core inside the Bondi radius on a timescale that is much smaller the Hubble time for a typical galaxy.

The future of astrophysical phenomenology of SIDM looks exciting as we are making progress on multiple fronts as a community, and there's a lot of left to be done. On the theory side, it will be very useful to come up with a simulation method that can work with a halo which is partly in SMFP, and partly in LMFP. Such a tool could be very useful in simulating both the formation and evolution of DM spikes, at the same time useful in simulating gravothermally collapsing DM haloes. In addition, as highlighted in Hamilton et al. (2024), there are lots of parallels between the kinetic theory of plasmas and kinetic theory of gravitating systems. Becoming fluent in both of these fields could come in handy in solving problems in the astrophysics of SIDM. N-body codes for ΛCDM cosmology have been calibrated well against each other over the years therefore a similar code comparison for different SIDM implementations could be very rewarding. On side of baryonic physics, Rodríguez-Cardoso et al. (2025) reported the findings of the AGORA (J.-h. Kim et al. 2014) suite of simulations which compares the results of cosmological hydro simulation across different codes like Gadget-2 (Springel 2005), ENZO (Bryan et al. 2014), AREPO (Springel 2010), ART-1 (Kravtsov et al. 1997), GEAR (Revaz et al. 2012) for identical initial conditions. They find significant discrepancies in stellar mass formed by satellite galaxies amongst different codes. Addressing such discrepancies and fine-tuning the baryonic physics is of crucial importance to make robust predictions at small scales.

On the side of observations, a lot of progress is expected in the coming years due to new instruments and their surveys. Upcoming survey like LSST (Ivezić et al. 2019) and ongoing surveys like SAGA (Geha et al. 2017), ELVES (Carlsten et al. 2022) can identify more satellite galaxies around Milky-Way and/or Milky-Way like hosts in the local volume. This could potentially improve constraints on SIDM via satellite abundances, and core sizes. In addition, objects identified by the above-mentioned can be followed up spectroscopically to measure the line-of-sight velocity dispersion with Keck (Oke et al. 1995) and other upcoming telescopes like Thirty metre telescope (Skidmore et al. 2015), Maunakea Spectroscopic Explorer (The MSE Science Team et al. 2019). Finally, with the GAIA (Gaia Collaboration et al. 2023) DR4 and DR5 the proper motions of Milky-Way satellites can be determined to higher precision enabling better kinematical understanding.

In addition to LSST, upcoming survey like Roman space telescope (D. Spergel et al. 2015), ongoing surveys like Euclid (Laureijs et al. 2011), finished surveys like DES (The Dark Energy Survey Collaboration 2005) will cumulatively observe significantly much more galaxy clusters. All of this would reduce the uncertainties, leading to better constraints on the SIDM cross-section. In particular, it is expected that the constraints will get at least better by a factor 2 (Harvey et al. 2019).

Square Kilometre Array (SKA) (de Blok et al. 2015), will observe and measure not only the gas kinematics of nearby galaxies and dwarf galaxies, but also measure the gas distribution until the redshift of reionization measuring the small scale power spectrum (Dewdney et al. 2009). WEAVE-QSO (Pieri et al. 2016) in addition X-shooter (Vernet et al. 2011), will constrain the non-linear scales of power spectrum due to improved Lyman-α datasets, and this could effectively better constrain SIWDM.

To conclude, in this thesis the current status and our contributions to astrophysical phenomenology of SIDM are presented. We extended the existing constraints by studying the effects of anisotropic and isotropic DM self-interactions with velocity dependence at the scale of galaxy clusters. Using N-body and hydro simulations, we verify for the first time that steady-state solutions of SIDM spikes are viable in the LMFP regime. In the SMFP regime we find that the accretion rates are mildly suppressed with respect to Bondi accretion rate. Furthermore, we derive expressions for the accretion rate from collisionless limit to hydrodynamic limit, which can possibly contribute to explaining the observations of SMBHs at high redshifts. Thus, we see that the study of the kinetic theory of gravitating systems, along with astrophysical and cosmological observations are crucial in our quest to uncover the true nature of DM.

Acknowledgments

This thesis owes much to the support of many people in both my personal and professional life. First, I would like to thank my supervisor Marcus Brüggen who has been very supportive throughout my PhD and for giving me the privilege to walk into his office whenever I wanted to have a chat with him, be it academic or not. I would also like to thank my co-supervisor Kai Schmidt-Hoberg for all the useful scientific discussions on topics not only limited to my thesis.

I further would like to thank Moritz Fischer and Lenard Kasselmann, with whom I discussed the most about SIDM physics. Thanks to Felix Kahlhöfer and his group for fun scientific discussions, hospitality and treating me as if I were a part of their group every time I visited them.

Life at the institute was thoroughly enjoyable thanks to all of my colleagues. Special thanks to Volker Heesen, Philip Grete, and Jörg Knoche for organizing most of the social events at the institute. Philip, thank you for offering help with hydro simulations despite your busy schedule. I thank Stephan Rosswog, and his group members for being welcoming of me and my naive questions during their group meetings. Thanks to Sören Witte, for invaluable IT assistance and for sharing fascinating palaeontology facts. I would like to specially thank Raghav, Angelina and Radha for their company, interesting conversations, walks and tea.

Thanks to Ajith and Bala for all the amazing gaming sessions, and workathons. I cannot emphasize enough as to how much I looked forward to our weekly Zoom meetings. Thanks to Sharif for proofreading my thesis, and for joining me in Neovim/terminal/Linux flex sessions. I would like to thank Arnold for being there during both tough and great times. Thanks to Lea for giving me a home away from home.

I thank Sowmiya for being all ears to endless scientific discussions, debates about anything within the horizon and for everything else you have given me over the years. I finally thank my family for their unwavering moral support, for nurturing my passion for physics and for managing everything at home while believing in me, my decisions and my dreams.

6 Bibliography

Aarseth S. J. (1963), Monthly Notices of the Royal Astronomical Society, 126 : 223

Abdalla E., Abellán G. F., Aboubrahim A., et al. (2022), JHEAp, 34 : 49–211

Ackerman L., Buckley M. R., Carroll S. M., and Kamionkowski M. (2009), PhRvD, 79 : 023519

Adhikari S., Banerjee A., Boddy K. K., et al. (2022), RvMP, 97 : 045004

Afzal A., Agazie G., Anumarlapudi A., et al. (2023), The Astrophysical Journal, 951 : L11

Agazie G., Anumarlapudi A., Archibald A. M., et al. (2023), ApJL, 951 :

Aguayo-Ortiz A., Tejeda E., Sarbach O., and López-Cámara D. (2021), MNRAS, 504 : 5039–5053

Ahn K. and Shapiro P. R. (2005), MNRAS, 363 : 1092–1110

Alachkar A., Ellis J., and Fairbairn M. (2023), PhRvD, 107 : 103033

Alexander T. (2005), Physics Reports, 419 : 65–142

Alonso-Álvarez G., Cline J. M., and Dewar C. (2024), PhRvL, 133 : 021401

Alpher R. A., Bethe H., and Gamow G. (1948), PhRv, 73 : 803–804

Amin M. A. and Mirbabayi M. (2024), Physical Review Letters, 132 : 221004

Andrade K. E., Fuson J., Gad-Nasr S., et al. (2021), MNRAS, 510 : 54–81

Angus G. W., Famaey B., and Diaferio A. (2010), MNRAS, 402 : 395–408

Angus G. W., Shan H. Y., Zhao H. S., and Famaey B. (2007), ApJL, 654 : L13–L16

Archidiacono M., Bohr S., Hannestad S., Helboe JØrgensen J., and Lesgourgues J. (2017), JCAP, 2017 : 010

Arido C., Fischer M. S., and Garny M. (2025), A&A, 694 : A297

Arkani-Hamed N., Finkbeiner D. P., Slatyer T. R., and Weiner N. (2009), Physical Review D, 79 : 015014

Bahcall J. N. and Wolf R. A. (1976), ApJ, 209 : 214–232

Bahcall N. A., Lubin L. M., and Dorman V. (1995), ApJL, 447 : L81

Bahé Y. M., Schaye J., Schaller M., et al. (2022), Monthly Notices of the Royal Astronomical Society, 516 : 167–184

Balan S., Balázs C., Bringmann T., et al. (2025), Journal of Cosmology and Astroparticle Physics, 2025 : 053

Balberg S. and Shapiro S. L. (2002a), Physical Review Letters, 88 : 101301

Balberg S., Shapiro S. L., and Inagaki S. (2002b), ApJ, 568 : 475–487

Bandara K., Crampton D., and Simard L. (2009), ApJ, 704 : 1135–1145

Barnes J. and Hut P. (1986), Natur, 324 : 446–449

Baumann D. (2022), Cosmology

Becker N., Sagunski L., Prinz L., and Rastgoo S. (2022), PhRvD, 105 : 063029

Bento M. C., Bertolami O., Rosenfeld R., and Teodoro L. (2000), PhRvD, 62 : 041302

Bertone G., Wierda A. R. A. C., Gaggero D., et al. (2024), PhRvD, 112 : 043537

Bethe H. A. (1949), Physical Review, 76 : 38–50

Bhatnagar P. L., Gross E. P., and Krook M. (1954), Physical Review, 94 : 511–525

Binney J. and Tremaine S. (2008), Galactic Dynamics

Bittencourt J. A. (2013), Fundamentals of Plasma Physics

Blandford R. D. and Znajek R. L. (1977), Monthly Notices of the Royal Astronomical Society, 179 : 433–456

Blennow M., Clementz S., and Herrero-Garcia J. (2017), Journal of Cosmology and Astroparticle Physics, 2017 : 048

Blumenthal G. R., Faber S. M., Flores R., and Primack J. R. (1986), The Astrophysical Journal, 301 : 27

Boddy K. K., Feng J. L., Kaplinghat M., and Tait T. M. P. (2014), PhRvD, 89 : 115017

Bode P., Ostriker J. P., and Turok N. (2001), ApJ, 556 : 93–107

Bœhm C., Fayet P., and Schaeffer R. (2001), Physics Letters B, 518 : 8–14

Bœhm C., Riazuelo A., Hansen S. H., and Schaeffer R. (2002), PhRvD, 66 : 083505

Boehm C., Schewtschenko J. A., Wilkinson R. J., Baugh C. M., and Pascoli S. (2014), MNRAS, 445 : L31–L35

Bogoliubov N. N. (1946), Journal of Physics, 10 : 265–274

Bohr S., Zavala J., Cyr-Racine F.-Y., et al. (2020), Monthly Notices of the Royal Astronomical Society, 498 : 3403–3419

Bondi H. (1952), MNRAS, 112 : 195

Born M. and Green H. S. (1946), Proceedings of the Royal Society of London. Series A, Mathematical and Physical Sciences, 188 : 10–18

Borrow J., Schaller M., Bahé Y. M., et al. (2023), Monthly Notices of the Royal Astronomical Society, 526 : 2441–2457

Bose S., Vogelsberger M., Zavala J., et al. (2019), Monthly Notices of the Royal Astronomical Society, 487 : 522–536

Boylan-Kolchin M., Bullock J. S., and Kaplinghat M. (2011), Monthly Notices of the Royal Astronomical Society, 415 : L40–L44

Boylan-Kolchin M., Bullock J. S., and Kaplinghat M. (2012), Monthly Notices of the Royal Astronomical Society, 422 : 1203–1218

Bradač M., Allen S. W., Treu T., et al. (2008), ApJ, 687 : 959–967

Bringmann T., Depta P. F., Hufnagel M., et al. (2023), Physical Review D, 107 : L071702

Bringmann T., Hasenkamp J., and Kersten J. (2014), Journal of Cosmology and Astroparticle Physics, 2014 : 042

Bringmann T., Kahlhoefer F., Schmidt-Hoberg K., and Walia P. (2017), Physical Review Letters, 118 : 141802

Bryan G. L., Norman M. L., O'Shea B. W., et al. (2014), The Astrophysical Journal Supplement Series, 211 : 19

Buckley M. R. and Fox P. J. (2010), Physical Review D, 81 : 083522

Bullock J. S. and Boylan-Kolchin M. (2017), ARA&A, 55 : 343–387

Burke-Spolaor S., Taylor S. R., Charisi M., et al. (2019), A&ARv, 27 : 5

Burkert A. (2000), The Astrophysical Journal, 534 : L143–L146

Caldwell N., Walker M. G., Mateo M., et al. (2017), The Astrophysical Journal, 839 : 20

Carignan C. and Freeman K. C. (1988), The Astrophysical Journal, 332 : L33

Carlberg R. G., Yee H. K. C., Ellingson E., et al. (1996), ApJ, 462 : 32

Carlsten S. G., Greene J. E., Beaton R. L., Danieli S., and Greco J. P. (2022), The Astrophysical Journal, 933 : 47

Carroll B. W. and Ostlie D. A. (2017), An Introduction to Modern Astrophysics, Second Edition

Cassel S. (2010), Journal of Physics G Nuclear Physics, 37 : 105009

Cautun M., Frenk C. S., van de Weygaert R., Hellwing W. A., and Jones B. J. T. (2014), Monthly Notices of the Royal Astronomical Society, 445 : 2049–2060

Cercignani C., Illner R., and Pulvirenti M. (1994), *The mathematical theory of dilute gases*

Cha S., Cho B. Y., Joo H., et al. (2025), The Astrophysical Journal, 987 : L15

Chan M. H. and Lee C. M. (2024), ApJL, 962 : L40

Chandrasekhar S. (1941), The Astrophysical Journal, 93 : 285

Chandrasekhar S. (1960), Principles of Stellar Dynamics

Chapman S. (1912), Philosophical Transactions of the Royal Society of London Series A, 211 : 433–483

Chapman S. (1916), Proceedings of the Royal Society of London Series A, 93 : 1–20

Chapman S. and Cowling T. G. (1970), The Mathematical Theory of Non-uniform Gases

Chen M.-C. and Tang Y. (2025), Physical Review D, 112 : 043033

Chen S.-R., Schive H.-Y., and Chiueh T. (2017), MNRAS, 468 : 1338–1348

Choquette J., Cline J. M., and Cornell J. M. (2019), JCAP, 2019 : 036

Chu X., Garcia-Cely C., and Murayama H. (2019), Physical Review Letters, 122 : 071103

Chu X., Garcia-Cely C., and Murayama H. (2020a), Journal of Cosmology and Astroparticle Physics, 2020 : 043

Chu X., Garcia-Cely C., and Murayama H. (2020b), Physical Review Letters, 124 : 041101

Clarke C. and Carswell B. (2007), Principles of Astrophysical Fluid Dynamics

Cline J. M., Liu Z., Moore G. D., and Xue W. (2014a), Physical Review D, 90 : 015023

Cline J. M., Liu Z., Moore G. D., and Xue W. (2014b), PhRvD, 89 : 043514

Clowe D., Gonzalez A., and Markevitch M. (2004), The Astrophysical Journal, 604 : 596–603

Colín P., Avila-Reese V., Valenzuela O., and Firmani C. (2002), The Astrophysical Journal, 581 : 777–793

Colquhoun B., Heeba S., Kahlhoefer F., Sagunski L., and Tulin S. (2021), Phys. Rev. D, 103 : 035006

Cooke R. J., Pettini M., and Steidel C. C. (2018), ApJ, 855 : 102

Correa C. A. (2021), MNRAS, 503 : 920–937

Correa C. A., Schaller M., Ploeckinger S., et al. (2022), MNRAS, 517 : 3045–3063

Correa C. A., Schaller M., Schaye J., et al. (2025), Monthly Notices of the Royal Astronomical Society, 536 : 3338–3356

Craig M. W. and Davis M. (2001), New Astronomy, 6 : 425–436

Crain R. A., Schaye J., Bower R. G., et al. (2015), Monthly Notices of the Royal Astronomical Society, 450 : 1937–1961

Cross D., Thoron G., Jeltema T., et al. (2023), MNRAS, 529 : 52

Cyr-Racine F.-Y. and Sigurdson K. (2013), Physical Review D, 87 : 103515

Cyr-Racine F.-Y., Sigurdson K., Zavala J., et al. (2016), PhRvD, 93 : 123527

D'Onghia E., Firmani C., and Chincarini G. (2003), Monthly Notices of the Royal Astronomical Society, 338 : 156–164

Davé R., Spergel D. N., Steinhardt P. J., and Wandelt B. D. (2001), The Astrophysical Journal, 547 : 574–589

Dawson W. A., Wittman D., Jee M. J., et al. (2012), ApJL, 747 : L42

Dawson W. A. (2013), PhD thesis, University of California, Davis

De Blok W. J. G. (2010), Advances in Astronomy, 2010 : 789293

De Blok W. J. G., Fraternali F., Heald G. H., et al. (2015), arXiv: 1501.01211

Dehnen W. and Read J. I. (2011), European Physical Journal Plus, 126 : 55

Dehnen W. (2001), Monthly Notices of the Royal Astronomical Society, 324 : 273–291

Despali G., Moscardini L., Nelson D., et al. (2025), A&A, 697 : A213

Dewdney P. E., Hall P. J., Schilizzi R. T., and Lazio T. J. L. W. (2009), IEEE Proceedings, 97 : 1482–1496

Dey L., Valtonen M. J., Gopakumar A., et al. (2018), ApJ, 866 : 11

Di Cintio A., Brook C. B., Dutton A. A., et al. (2014), Monthly Notices of the Royal Astronomical Society, 441 : 2986–2995

Dodelson S. and Schmidt F. (2020), *Modern Cosmology*

Dosopoulou F. and Antonini F. (2017), ApJ, 840 : 31

Duerr M., Schmidt-Hoberg K., and Wild S. (2018), Journal of Cosmology and Astroparticle Physics, 2018 : 033

Dutton A. A. and Macciò A. V. (2014), MNRAS, 441 : 3359–3374

Dutton A. A., Macciò A. V., Frings J., et al. (2016), Monthly Notices of the Royal Astronomical Society, 457 : L74–L78

Eckert D., Ettori S., Pointecouteau E., et al. (2017), Astronomische Nachrichten, 338 : 293–298

Eckert D., Ettori S., Robertson A., et al. (2022), A&A, 666 : A41

Egana-Ugrinovic D., Essig R., Gift D., and LoVerde M. (2021), JCAP, 2021 : 013

Elbert O. D., Bullock J. S., Garrison-Kimmel S., et al. (2015), MNRAS, 453 : 29–37

Ellis J., Fairbairn M., Franciolini G., et al. (2024), PhRvD, 109 :

Enskog D. (1917), Kinetische Theorie Der Vorgaenge in Maessig Verduennten Gasen. I. Allgemeiner Teil

Essig R., McDermott S. D., Yu H.-B., and Zhong Y.-M. (2019), Phys. Rev. Lett. 123 : 121102

Faghei K. (2012), MNRAS, 420 : 118–125

Fan X., Bañados E., and Simcoe R. A. (2023), ARA&A, 61 : 373–426

Feng C., Tang Y., and Wu Y.-L. (2026), Physical Review D, 113 : 023016

Feng J. L., Kaplinghat M., Tu H., and Yu H.-B. (2009), JCAP, 2009 : 004

Feng W.-X., Yu H.-B., and Zhong Y.-M. (2021), ApJL, 914 : L26

Feng W.-X., Yu H.-B., and Zhong Y.-M. (2022), JCAP, 2022 : 036

Feng W.-X., Yu H.-B., and Zhong Y.-M. (2025), arXiv: 2506.17641

Finkbeiner D. P. and Weiner N. (2007), Physical Review D, 76 : 083519

Fischer M. S., Brüggen M., Schmidt-Hoberg K., et al. (2021), MNRAS, 505 : 851–868

Fischer M. S., Brüggen M., Schmidt-Hoberg K., et al. (2022a), Mon. Not. Roy. Astron. Soc. 516 : 1923–1940

Fischer M. S., Brüggen M., Schmidt-Hoberg K., et al. (2022b), MNRAS, 510 : 4080–4099

Fischer M. S., Dolag K., and Yu H.-B. (2024a), A&A, 689 : A300

Fischer M. S., Durke N.-H., Hollingshausen K., et al. (2023), MNRAS, 523 : 5915–5933

Fischer M. S., Kasselmann L., Brüggen M., et al. (2024b), MNRAS, 529 : 2327–2348

Fischer M. S. and Sagunski L. (2024c), A&A, 690 : A299

Flores R. A. and Primack J. R. (1994), The Astrophysical Journal, 427 : L1

Forestell L., Morrissey D. E., and White G. (2019), Journal of High Energy Physics, 2019 : 74

Fortov V. E., Ivlev A. V., Khrapak S. A., Khrapak A. G., and Morfill G. E. (2005), Physics Reports, 421 : 1–103

Frank J., King A., and Raine D. J. (2002), Accretion Power in Astrophysics

Freedman W. L., Madore B. F., Hoyt T. J., et al. (2025), ApJ, 985 : 203

Friedmann A. (1922), ZPhy, 10 : 377–386

Fritz T. K., Battaglia G., Pawlowski M. S., et al. (2018), Astronomy and Astrophysics, 619 : A103

Gaia Collaboration, Vallenari A., Brown A. G. A., et al. (2023), Astronomy and Astrophysics, 674 : A1

Gamow G. (1946), PhRv, 70 : 572–573

Garani R., Redi M., and Tesi A. (2022), JCAP, 2022 : 012

Garlick A. R. (1979), A&A, 73 : 171–173

Garzó V. and Dufty J. W. (1999), Physical Review E, 59 : 5895–5911

Gastaldello F., Buote D. A., Humphrey P. J., et al. (2007), The Astrophysical Journal, 669 : 158–183

Geha M., Wechsler R. H., Mao Y.-Y., et al. (2017), The Astrophysical Journal, 847 : 4

Genel S., Vogelsberger M., Springel V., et al. (2014), MNRAS, 445 : 175–200

Gilman D., Bovy J., Treu T., et al. (2021), MNRAS, 507 : 2432–2447

Gilman D., Zhong Y.-M., and Bovy J. (2023), Phys. Rev. D, 107 : 103008

Girmohanta S. and Shrock R. (2022), PhRvD, 106 : 063013

Gnedin O. Y., Ceverino D., Gnedin N. Y., et al. (2011), arXiv: 1108.5736

Gnedin O. Y., Kravtsov A. V., Klypin A. A., and Nagai D. (2004), ApJ, 616 : 16–26

Gnedin O. Y. and Ostriker J. P. (2001), The Astrophysical Journal, 561 : 61–68

Gondolo P. and Silk J. (1999), Phys. Rev. Lett. 83 : 1719–1722

Gopika K. and Desai S. (2023), PDU, 42 : 101291

Gorchtein M., Profumo S., and Ubaldi L. (2010), PhRvD, 82 : 083514

Grad H. (1949), Pure and Applied Mathematics, 2 : 331–407

Green H. S. (1952), Transactions of the Faraday Society, 48 : 11–27

Groth F., Steinwandel U. P., Valentini M., and Dolag K. (2023), MNRAS, 526 : 616–644

Gruzinov A. (1998), arXiv: astro-ph/9809265

Gu H.-P., Jiang F., Chen X., and Li R. (2026), arXiv: 2601.17117

Hamann J., Hannestad S., Raffelt G. G., Tamborra I., and Wong Y. Y. Y. (2010), PhRvL, 105 : 181301

Hambye T. and Vanderheyden L. (2020), Journal of Cosmology and Astroparticle Physics, 2020 : 001

Hamilton C. and Fouvry J.-B. (2024), PhPl, 31 : 120901

Harvey D., Massey R., Kitching T., Taylor A., and Tittley E. (2015), Sci, 347 : 1462–1465

Harvey D., Robertson A., Massey R., and McCarthy I. G. (2019), MNRAS, 488 : 1572–1579

Hernquist L. (1990), ApJ, 356 : 359

Hochberg Y., Kuflik E., Murayama H., Volansky T., and Wacker J. G. (2015), Physical Review Letters, 115 : 021301

Hockney R. W. and Eastwood J. W. (1988), Computer Simulation Using Particles

Holdom B. (1986), Physics Letters B, 166 : 196–198

Holzer T. E. and Axford W. I. (1970), ARA&A, 8 : 31

Hu W., Barkana R., and Gruzinov A. (2000), PhRvL, 85 : 1158–1161

Hubble E. (1929), PNAS, 15 : 168–173

Hufnagel M., Schmidt-Hoberg K., and Wild S. (2018), Journal of Cosmology and Astroparticle Physics, 2018 : 032

Hui L. (2021), ARA&A, 59 : 247–289

Inayoshi K. and Ho L. C. (2025), arXiv: 2512.03130

Inayoshi K., Visbal E., and Haiman Z. (2020), ARA&A, 58 : 27–97

Ivezić Ž., Kahn S. M., Tyson J. A., et al. (2019), The Astrophysical Journal, 873 : 111

Jackson R. A., Navarro J. F., Santos-Santos I. M. E., et al. (2025), Monthly Notices of the Royal Astronomical Society, 539 : 3797–3807

Jeans J. H. (1915), Monthly Notices of the Royal Astronomical Society, 76 : 70–84

Jeans J. H. (1922), MNRAS, 82 : 122–132

Jee M. J., Hughes J. P., Menanteau F., et al. (2014), ApJ, 785 : 20

Jee M. J., Stroe A., Dawson W., et al. (2015), ApJ, 802 : 46

Ji A. P., Koposov S. E., Li T. S., et al. (2021), The Astrophysical Journal, 921 : 32

Jiang F., Benson A., Hopkins P. F., et al. (2023), MNRAS, 521 : 4630–4644

Jiang F., Jia Z., Zheng H., et al. (2025), ApJL, 996 : L19

Jiang F. and van den Bosch F. C. (2015), Monthly Notices of the Royal Astronomical Society, 453 : 3575–3592

Jiao C.-L., Zhao E.-g., Zhu L., and Shi X.-d. (2025), ApJ, 989 : 94

Johnson B. M. and Quataert E. (2007), ApJ, 660 : 1273–1281

Kahlhoefer F., Schmidt-Hoberg K., Frandsen M. T., and Sarkar S. (2014), MNRAS, 437 : 2865–2881

Kahlhoefer F., Schmidt-Hoberg K., and Wild S. (2017), J. Cosmol. Astropart. Phys. 2017 : 003–003

Kamada A., Kaplinghat M., Pace A. B., and Yu H.-B. (2017), Phys. Rev. Lett. 119 : 111102

Kaplinghat M., Keeley R. E., Linden T., and Yu H.-B. (2014), Physical Review Letters, 113 : 021302

Kaplinghat M., Tulin S., and Yu H.-B. (2016), PhRvL, 116 : 041302

Kapteyn J. C. (1922), ApJ, 55 : 302

Katrin Collaboration, Aker M., Batzler D., et al. (2025), Science, 388 : 180–185

Kavanagh B. J., Karydas T. K., Bertone G., Di Cintio P., and Pasquato M. (2024), PhRvD, 111 : 063071

Kavanagh B. J., Nichols D. A., Bertone G., and Gaggero D. (2020), PhRvD, 102 : 083006

Keto E. (2020), MNRAS, 493 : 2834–2840

Khlopov M. Yu. (2006), Soviet Journal of Experimental and Theoretical Physics Letters, 83 : 1–4

Khrapak S. A., Ivlev A. V., Morfill G. E., and Zhdanov S. K. (2003), Physical Review Letters, 90 : 225002

Khrapak S. A., Ivlev A. V., and Morfill G. E. (2004), Physical Review E, 70 : 056405

Kim D., Jerjen H., Mackey D., Da Costa G. S., and Milone A. P. (2015), The Astrophysical Journal, 804 : L44

Kim J.-h., Abel T., Agertz O., et al. (2014), The Astrophysical Journal Supplement Series, 210 : 14

Kim S. Y., Peter A. H. G., and Hargis J. R. (2018), Physical Review Letters, 121 : 211302

Kim S. Y., Peter A. H. G., and Wittman D. (2017), MNRAS, 469 : 1414–1444

Kirkwood J. G. (1946), The Journal of Chemical Physics, 14 : 180–201

Klypin A., Kravtsov A. V., Valenzuela O., and Prada F. (1999), The Astrophysical Journal, 522 : 82–92

Knudsen M. (1909), Annalen der Physik, 333 : 75–130

Kocevski D. D., Onoue M., Inayoshi K., et al. (2023), The Astrophysical Journal, 954 : L4

Kochanek C. S. and White M. (2000), ApJ, 543 : 514–520

Koda J. and Shapiro P. R. (2011), MNRAS, 415 : 1125–1137

Kong D., Yang D., and Yu H.-B. (2024), The Astrophysical Journal, 965 : L19

Kravtsov A. V., Klypin A. A., and Khokhlov A. M. (1997), The Astrophysical Journal Supplement Series, 111 : 73–94

Kribs G. D. and Neil E. T. (2016), International Journal of Modern Physics A, 31 : 1643004–764

Kroupa P., Pawlowski M., and Milgrom M. (2012), International Journal of Modern Physics D, 21 : 1230003

Kummer J., Brüggen M., Dolag K., Kahlhoefer F., and Schmidt-Hoberg K. (2019), MNRAS, 487 : 354–363

Kummer J., Kahlhoefer F., and Schmidt-Hoberg K. (2018), MNRAS, 474 : 388–399

Lacroix T., Karami M., Broderick A. E., Silk J., and Bœhm C. (2017), PhRvD, 96 : 063008

Lacroix T., Stref M., and Lavalle J. (2018), JCAP, 2018 : 040

Lanford O. E. (1975). "Time Evolution of Large Classical Systems". *Dynamical Systems, Theory and Applications*. Vol. 38, 1–111

Lauer T. R., Postman M., Strauss M. A., Graves G. J., and Chisari N. E. (2014), ApJ, 797 : 82

Laureijs R., Amiaux J., Arduini S., et al. (2011), arXiv: 1110.3193

Lelli F., McGaugh S. S., and Schombert J. M. (2016), AJ, 152 : 157

Lelli F., McGaugh S. S., Schombert J. M., and Pawlowski M. S. (2017), The Astrophysical Journal, 836 : 152

Lemaître G. (1931), MNRAS, 91 : 490–501

Li X., Hui L., and Yavetz T. D. (2021), Physical Review D, 103 : 023508

Lightman A. P. and Shapiro S. L. (1977), The Astrophysical Journal, 211 : 244–262

Liu R., Hu W., and Xiao H. (2025), PhRvD, 111 : 023535

Lu Y., Mo H. J., Katz N., and Weinberg M. D. (2006), MNRAS, 368 : 1931–1940

Lynden-Bell D. and Eggleton P. P. (1980), MNRAS, 191 : 483–498

Lynden-Bell D. and Pringle J. E. (1974), MNRAS, 168 : 603–637

Lynden-Bell D. and Wood R. (1968), MNRAS, 138 : 495

Ma C.-P. and Bertschinger E. (1995), ApJ, 455 : 7

Macciò A. V., Paduroiu S., Anderhalden D., Schneider A., and Moore B. (2012), MNRAS, 424 : 1105–1112

Mace C., Yang S., Carton Zeng Z., et al. (2025), arXiv: 2504.13004

Magorrian J. and Tremaine S. (1999), Monthly Notices of the Royal Astronomical Society, 309 : 447–460

Markevitch M., Gonzalez A. H., Clowe D., et al. (2004), ApJ, 606 : 819–824

Markevitch M., Gonzalez A. H., David L., et al. (2002), The Astrophysical Journal, 567 : L27–L31

Matthee J., Naidu R. P., Brammer G., et al. (2024), The Astrophysical Journal, 963 : 129

McDonald J. (2002), Physical Review Letters, 88 : 091304

Mehran Kardar (2007), Statistical Physics of Particles

Merritt D. (2004a), PhRvL, 92 : 201304

Merritt D. (2004b), arXiv: astro-ph/0301257

Merritt D. (2013), Classical and Quantum Gravity, 30 : 244005

Milgrom M. (1983), The Astrophysical Journal, 270 : 365–370

Mo H., Bosch F. van den, and White S. (2010), *Galaxy Formation and Evolution*

Mohapatra R. N., Nussinov S., and Teplitz V. L. (2002), Physical Review D, 66 : 063002

Monaghan J. J. and Lattanzio J. C. (1985), Astronomy and Astrophysics, 149 : 135–143

Moore B. (1994), Nature, 370 : 629–631

Moore B., Ghigna S., Governato F., et al. (1999), The Astrophysical Journal, 524 : L19–L22

Mukherjee D., Holgado A. M., Ogiya G., and Trac H. (2024), MNRAS, 533 : 2335

Nadler E. O., An R., Yang D., et al. (2025), The Astrophysical Journal, 986 : 129

Narayan R. and Yi I. (1994), The Astrophysical Journal, 428 : L13

Navarro J. F., Frenk C. S., and White S. D. M. (1996), ApJ, 462 : 563

Newman A. B., Ellis R. S., and Treu T. (2015), The Astrophysical Journal, 814 : 26

Newman A. B., Treu T., Ellis R. S., and Sand D. J. (2013a), The Astrophysical Journal, 765 : 25

Newman A. B., Treu T., Ellis R. S., et al. (2013b), ApJ, 765 : 24

Nishikawa H., Boddy K. K., and Kaplinghat M. (2020), PhRvD, 101 : 063009

O'Neil S., Vogelsberger M., Heeba S., et al. (2022), MNRAS, 524 : 288

Oke J. B., Cohen J. G., Carr M., et al. (1995), Publications of the Astronomical Society of the Pacific, 107 : 375

Oman K. A., Navarro J. F., Fattahi A., et al. (2015), MNRAS, 452 : 3650–3665

Oort J. H. (1932), Bulletin of the Astronomical Institutes of the Netherlands, 6 : 249

Ostriker J. P., Choi E., Chow A., and Guha K. (2019), The Astrophysical Journal, 885 : 97

Outmezguine N. J., Boddy K. K., Gad-Nasr S., Kaplinghat M., and Sagunski L. (2023), MNRAS, 523 : 4786–4800

Pace A. B., Erkal D., and Li T. S. (2022), The Astrophysical Journal, 940 : 136

Penzias A. A. and Wilson R. W. (1965), ApJ, 142 : 419–421

Pert G. J. (2021), Foundations of Plasma Physics for Physicists and Mathematicians

Piattella O. (2018), *Lecture Notes in Cosmology*

Pieri M. M., Bonoli S., Chaves-Montero J., et al. (2016), arXiv: 1611.09388

Pitaevskii L. P. and Lifshitz E. M. (1981), Physical Kinetics

Planck Collaboration, Aghanim N., Akrami Y., et al. (2020a), A&A, 641 : A6

Planck Collaboration, Akrami Y., Ashdown M., et al. (2020b), A&A, 641 : A1

Poisson E. and Will C. M. (2014), Gravity

Pollack J., Spergel D. N., and Steinhardt P. J. (2015), ApJ, 804 : 131

Poulin V., Lesgourgues J., and Serpico P. D. (2017), Journal of Cosmology and Astroparticle Physics, 2017 : 043

Press W. H., Teukolsky S. A., Vetterling W. T., and Flannery B. P. (2002), Numerical Recipes in C++

Pringle J. E. (1981), ARA&A, 19 : 137–162

Purcell C. W. and Zentner A. R. (2012), Journal of Cosmology and Astroparticle Physics, 2012 : 007

Ragagnin A., Meneghetti M., Calura F., et al. (2024), A&A, 687 : A270

Ragagnin A., Tchipev N., Bader M., Dolag K., and Hammer N. J. (2016), arXiv: 1810.09898

Randall S. W., Markevitch M., Clowe D., Gonzalez A. H., and Bradač M. (2008), ApJ, 679 : 1173

Ranjbar R., Olivares-Sánchez H. R., and Abbassi S. (2025), ApJ, 992 : 147

Ray A. K. and Bhattacharjee J. K. (2007), arXiv: astro-ph/0703301

Read J. I. and Erkal D. (2019), Monthly Notices of the Royal Astronomical Society, 487 : 5799–5812

Reardon D. J., Zic A., Shannon R. M., et al. (2023), The Astrophysical Journal, 951 : L6

Reeves H., Audouze J., Fowler W. A., and Schramm D. N. (1973), ApJ, 179 : 909–930

Ren T., Kwa A., Kaplinghat M., and Yu H.-B. (2019), Phys. Rev. X, 9 : 031020

Revaz Y. and Jablonka P. (2012), Astronomy and Astrophysics, 538 : A82

Riess A. G., Scolnic D., Anand G. S., et al. (2024), ApJ, 977 : 120

Roberts M. S. and Whitehurst R. N. (1975), ApJ, 201 : 327–346

Robertson A., Massey R., and Eke V. (2017a), MNRAS, 467 : 4719–4730

Robertson A., Massey R., and Eke V. (2017b), MNRAS, 465 : 569–587

Robertson A., Massey R., Eke V., Schaye J., and Theuns T. (2021), Monthly Notices of the Royal Astronomical Society, 501 : 4610–4634

Robertson H. P. (1935), ApJ, 82 : 284

Roca-Fàbrega S., Kim J.-H., Hausammann L., et al. (2021), The Astrophysical Journal, 917 : 64

Rocha M., Peter A. H. G., Bullock J. S., et al. (2013), Monthly Notices of the Royal Astronomical Society, 430 : 81–104

Rodríguez-Cardoso R., Roca-Fàbrega S., Jung M., et al. (2025), Astronomy and Astrophysics, 698 : A303

Romualdez L. J., Benton S. J., Clark P., et al. (2016), arXiv: 1608.02502

Rosswog S. and Diener P. (2021), CQGra, 38 : 115002

Rosswog S. and Diener P. (2024), arXiv: 2404.15952

Rubin V. C., Ford Jr. W. K., and Thonnard N. (1980), ApJ, 238 : 471–487

Rubin V. C. and Ford Jr. W. K. (1970), ApJ, 159 : 379

Sabarish V. M., Brüggen M., Hoberg K.-S., and Fischer M. S. (2025), Astronomy and Astrophysics, 703 : A142

Sabarish V. M., Brüggen M., Schmidt-Hoberg K., Fischer M. S., and Kahlhoefer F. (2024), MNRAS, 529 : 2032–2046

Sadeghian L., Ferrer F., and Will C. M. (2013), Phys. Rev. D, 88 : 063522

Sagunski L., Gad-Nasr S., Colquhoun B., Robertson A., and Tulin S. (2021), J. Cosmol. Astropart. Phys. 2021 : 024–024

Sankar Ray T., Sarkar S., and Kumar Shaw A. (2022), JCAP, 2022 : 011

Santos-Santos I. M. E., Navarro J. F., Robertson A., et al. (2020), Monthly Notices of the Royal Astronomical Society, 495 : 58–77

Schaye J., Crain R. A., Bower R. G., et al. (2015), Monthly Notices of the Royal Astronomical Society, 446 : 521–554

Schive H.-Y., Chiueh T., and Broadhurst T. (2014a), NatPh, 10 : 496–499

Schive H.-Y., Liao M.-H., Woo T.-P., et al. (2014b), PhRvL, 113 : 261302

Schneider A., Smith R. E., and Reed D. (2013), MNRAS, 433 : 1573–1587

Schöneberg N., Abellán G. F., Sánchez A. P., et al. (2022), Physics Reports, 984 : 1–55

Schutz K. and Slatyer T. R. (2015), Journal of Cosmology and Astroparticle Physics, 2015 : 021–021

Shakura N. I. and Sunyaev R. A. (1973), A&A, 24 : 337–355

Shapiro S. L. (2018), PhRvD, 98 : 023021

Shapiro S. L. (2023), PhRvD, 108 : 083037

Shapiro S. L. and Paschalidis V. (2014), Phys. Rev. D, 89 : 023506

Sharma P., Quataert E., and Stone J. M. (2008), MNRAS, 389 : 1815–1827

Shen T., Shen X., Xiao H., Vogelsberger M., and Jiang F. (2025), arXiv: 2504.00075

Shirasaki M., Lau E. T., and Nagai D. (2018), Monthly Notices of the Royal Astronomical Society, 477 : 2804–2814

Shu F. H. (1992), The Physics of Astrophysics. Volume II

Sigurdson K. and Kamionkowski M. (2004), Physical Review Letters, 92 : 171302

Skidmore W., TMT International Science Development Teams, and Science Advisory Committee T. M. T. (2015), Research in Astronomy and Astrophysics, 15 : 1945

Skordis C. (2009), CQGra, 26 : 143001

Skordis C. and Złośnik T. (2021), PhRvL, 127 : 161302

Slatyer T. R. (2010), Journal of Cosmology and Astroparticle Physics, 2010 : 028

Slone O., Jiang F., Lisanti M., and Kaplinghat M. (2023), PhRvD, 107 : 043014

Smoot G. F., Bennett C. L., Kogut A., et al. (1992), ApJL, 396 : L1

Spergel D., Gehrels N., Baltay C., et al. (2015), arXiv: 1503.03757

Spergel D. N. and Steinhardt P. J. (2000), Phys. Rev. Lett. 84 : 3760–3763

Springel V. (2005), MNRAS, 364 : 1105–1134

Springel V. (2010), MNRAS, 401 : 791–851

Springel V. (2016), MNRAS, 43 : 251

Steckelmacher W. (1986), Reports on Progress in Physics, 49 : 1083–1107

Stone J. M., Tomida K., White C. J., and Felker K. G. (2020), The Astrophysical Journal Supplement Series, 249 : 4

Tan C. Y., Dekker A., and Drlica-Wagner A. (2025), PhRvD, 111 : 063079

Tanaka T. and Menou K. (2006), ApJ, 649 : 345–360

The Dark Energy Survey Collaboration (2005), arXiv: astro-ph/0510346

The MSE Science Team, Babusiaux C., Bergemann M., et al. (2019), arXiv: 1904.04907

Theis C. (1998), Astronomy and Astrophysics, 330 : 1180–1189

Tiruvaskar S. and Gordon C. (2025), PhRvD, 113 : 043501

Torrealba G., Belokurov V., Koposov S. E., et al. (2018), Monthly Notices of the Royal Astronomical Society, 475 : 5085–5097

Tucker W., Blanco P., Rappoport S., et al. (1998), The Astrophysical Journal, 496 : L5–L8

Tulin S. and Yu H.-B. (2018), Physics Reports, 730 : 1–57

Tulin S., Yu H.-B., and Zurek K. M. (2013a), PhRvD, 87 : 115007

Tulin S., Yu H.-B., and Zurek K. M. (2013b), Physical Review Letters, 110 : 111301

Van Dokkum P., Brammer G., Wang B., Leja J., and Conroy C. (2024), Nature Astronomy, 8 : 119–125

Van Beijeren H. and Ernst M. H. (1973), Physica, 68 : 437–456

Van den Aarssen L. G., Bringmann T., and Pfrommer C. (2012), Physical Review Letters, 109 : 231301

Vernet J., Dekker H., D'Odorico S., et al. (2011), Astronomy and Astrophysics, 536 : A105

Viel M., Lesgourgues J., Haehnelt M. G., Matarrese S., and Riotto A. (2005), PhRvD, 71 : 063534

Vincenti W. G. and Kruger C. H. (1965), Introduction to Physical Gas Dynamics

Vogelsberger M., Zavala J., Cyr-Racine F.-Y., et al. (2016), MNRAS, 460 : 1399–1416

Vogelsberger M., Zavala J., and Loeb A. (2012), MNRAS, 423 : 3740–3752

Walker A. G. (1935), QJMat, 1 : 81–93

Wilkinson R. J., Bœhm C., and Lesgourgues J. (2014), Journal of Cosmology and Astroparticle Physics, 2014 : 011

Wittman D., Golovich N., and Dawson W. A. (2018), The Astrophysical Journal, 869 : 104

Wright A. H., Stölzner B., Asgari M., et al. (2025), A&A, 703 : A158

Yang D. and Yu H.-B. (2022), J. Cosmol. Astropart. Phys. 2022 : 077

Yang S., Du X., Zeng Z. C., et al. (2023a), Astrophys. J. 946 : 47

Yang S., Jiang F., Benson A., et al. (2023b), MNRAS, 533 : 4007

Yoshida N., Springel V., White S. D. M., and Tormen G. (2000), MNRAS, 535 : L103–L106

Yuan F. and Narayan R. (2014), ARA&A, 52 : 529–588

Yunis R., Argüelles C. R., and Nacir D. L. (2020), J. Cosmol. Astropart. Phys. 2020 : 041–041

Yvon, Jacques and Rocard, Yves (1935), *La Théorie Statistique Des Fluides et l'équation d'état.*

Zappacosta L., Buote D. A., Gastaldello F., et al. (2006), The Astrophysical Journal, 650 : 777–790

Zentner A., Dandavate S., Slone O., and Lisanti M. (2022), Journal of Cosmology and Astroparticle Physics, 2022 : 031

Zhang X., Yu H.-B., Yang D., and An H. (2024), The Astrophysical Journal, 968 : L13

Zhao H. and Silk J. (2005), PhRvL, 95 : 011301

Zolotov A., Brooks A. M., Willman B., et al. (2012), The Astrophysical Journal, 761 : 71

Zwicky F. (1933), AcHPh, 6 : 110–127

Zwicky F. (1937), ApJ, 86 : 217